AUG 1 6 1988

1051-H-11

Y3.N88:25/5119

NUREG/CR-5119
EGG-2537

Metallographic Examination of the Severe Fuel Damage Scoping Test (SFD-ST) Fuel Rod Bundle Cross Sections

Prepared by P. Hofmann

Idaho National Engineering Laboratory
EG&G Idaho, Inc.

Prepared for
U.S. Nuclear Regulatory
Commission

COMPLETED

C[illegible]D

med/Am

ORIGINAL

NOTICE

This report was prepared as an account of work sponsored by an agency of the United States Government. Neither the United States Government nor any agency thereof, or any of their employees, makes any warranty, expressed or implied, or assumes any legal liability of responsibility for any third party's use, or the results of such use, of any information, apparatus, product or process disclosed in this report, or represents that its use by such third party would not infringe privately owned rights.

NOTICE

Availability of Reference Materials Cited in NRC Publications

Most documents cited in NRC publications will be available from one of the following sources:

1. The NRC Public Document Room, 1717 H Street, N.W.
   Washington, DC 20555
2. The Superintendent of Documents, U.S. Government Printing Office, Post Office Box 37082, Washington, DC 20013-7082
3. The National Technical Information Service, Springfield, VA 22161.

Although the listing that follows represents the majority of documents cited in NRC publications, it is not intended to be exhaustive.

Referenced documents available for inspection and copying for a fee from the NRC Public Document Room include NRC correspondence and internal NRC memoranda; NRC Office of Inspection and Enforcement bulletins, circulars, information notices, inspection and investigation notices; Licensee Event Reports; vendor reports and correspondence; Commission papers; and applicant and licensee documents and correspondence.

The following documents in the NUREG series are available for purchase from the GPO Sales Program: formal NRC staff and contractor reports, NRC-sponsored conference proceedings, and NRC booklets and brochures. Also available are Regulatory Guides, NRC regulations in the *Code of Federal Regulations*, and *Nuclear Regulatory Commission Issuances*.

Documents available from the National Technical Information Service include NUREG series reports and technical reports prepared by other federal agencies and reports prepared by the Atomic Energy Commission, forerunner agency to the Nuclear Regulatory Commission.

Documents available from public and special technical libraries include all open literature items, such as books, journal and periodical articles, and transactions. *Federal Register* notices, federal and state legislation, and congressional reports can usually be obtained from these libraries.

Documents such as theses, dissertations, foreign reports and translations, and non-NRC conference proceedings are available for purchase from the organization sponsoring the publication cited.

Single copies of NRC draft reports are available free, to the extent of supply, upon written request to the Division of Information Support Services, Distribution Section, U.S. Nuclear Regulatory Commission, Washington, DC 20555.

Copies of industry codes and standards used in a substantive manner in the NRC regulatory process are maintained at the NRC Library, 7920 Norfolk Avenue, Bethesda, Maryland, and are available there for reference use by the public. Codes and standards are usually copyrighted and may be purchased from the originating organization or, if they are American National Standards, from the American National Standards Institute, 1430 Broadway, New York, NY 10018.

NUREG/CR-5119
EGG-2537
R3

Metallographic Examination of the Severe Fuel Damage Scoping Test (SFD-ST) Fuel Rod Bundle Cross Sections

---

Manuscript Completed: June 1988
Date Published: July 1988

Prepared by
P. Hofmann*

Idaho National Engineering Laboratory
Managed by the U.S. Department of Energy

EG&G Idaho, Inc.
P.O. Box 1625
Idaho Falls, ID 83415

*Kernforschungszentrum Karlsruhe
Institute fur Material und Festkoerperforschung
Postfach 3640, D-7500 Karlsruhe
Federal Republic of Germany

Prepared for
Division of Reactor Accident Analysis
Office of Nuclear Regulatory Research
U.S. Nuclear Regulatory Commission
Washington, D.C. 20555
NRC FIN A6305
Under DOE Contract No. DE-AC07-76ID01570

ABSTRACT

A series of severe fuel damage (SFD) tests was performed in the Power Burst Facility (PBF) at the Idaho National Engineering Laboratory (INEL) to obtain data necessary to understand: (a) fission product release, deposition, and transport; (b) hydrogen release; and (c) fuel behavior and coolability during severe fuel damage accidents. This report presents the results from the metallographic posttest examination of the fuel rod bundle cross sections of the first experiment in the SFD series, the Scoping Test (SFD-ST). The metallographic appearance of the zircaloy cladding, solidified melt, UO_2 fuel, Inconel spacer grids, and other instrumentation and structural components is discussed. The observed structures are compared to those documented in well defined, out-of-pile, separate-effects reference experiments. The chemical interactions that take place at high temperatures between the fuel bundle components are described; and estimates of peak test temperatures are made, based only on metallography since scanning electron microscopy results were not available.

FIN No. A6305—TFEP Severe Fuel Damage Studies

FOREWORD

This report represents the initial effort to determine the material interactions and fission product release during the Severe Fuel Damage Scoping Test (SFD-ST) conducted in the Power Burst Facility (PBF). This work was done before chemical analyses and elemental distribution measurements were made, using a scanning electron microscope with X-ray spectroscopy. The reader is encouraged to read the report entitled ***PBF Severe Fuel Damage Scoping Test—Test Results Report***, NUREG/CR-4683, EGG-2413, August 1986, for a complete discussion of experiment results.

BEST COPY AVAILABLE

iv

SUMMARY

The Severe Fuel Damage Scoping Test (SFD-ST) was conducted in the Power Burst Facility (PBF) at the Idaho National Engineering Laboratory (INEL) on October 29, 1982, as part of the U.S. Nuclear Regulatory Commission's (NRCs) internationally sponsored severe accident research Program. The objectives of the program are to investigate light water reactor fuel rod and core response and the release and transport of fission products and hydrogen during severe fuel damage accidents.

The SFD-ST, first in a series of four bundle experiments, consisted of a 32-rod bundle of pressurized-water-reactor-type fuel rods, 0.91-m long and enclosed in an insulated shroud. The bundle was subjected to a slow heatup (to about 1373 K in the lower part of the fuel bundle and to about 1773 K in the upper part of the bundle) and then rapid heatup to the maximum bundle temperatures, followed by coolant reflood and quenching. After testing, the fuel rod bundle was examined using various nondestructive and destructive techniques. The bundle was epoxy-encapsulated, sectioned, and metallographically examined.

The microstructural examination of the SFD-ST fuel rod bundle cross sections identified a great variety of metallic and ceramic materials and solid and liquid interaction products. The microstructures were compared to well-defined, out-of-pile, separate-effects tests in order to determine material composition. Melt regions high in uranium content were identified. Maximum temperature estimates were made based on microstructure and material composition. Peak temperatures of at least 2873 K were reached, with a few indications of the onset of fuel melting (≃3123 K). Large temperature gradients (1073 K and more) were observed in many cross sections.

✓

ACKNOWLEDGMENTS

This report was completed with the help and assistance of many people. J. E. Stoyack developed the metallographic sample preparation techniques, and P. M. Stephens and M. Lindstrom performed the sampling. S. O. Peck performed the hot cell metallographic examinations of the fuel rod bundle cross sections. Detailed technical discussions about the appearance of the metallographic structures were held with Dr. M. L. Picklesimer and Dr. R. R. Hobbins. B. A. Cook and J. E. Stoyack are thanked for their technical review of the report.

CONTENTS

ABSTRACT ii iii

FOREWORD iii iv

SUMMARY iv v

ACKNOWLEDGMENTS v vi

INTRODUCTION 1

FUEL ROD BUNDLE SECTIONING 3

RESULTS OF THE METALLOGRAPHIC EXAMINATIONS 18

- Metallographic Appearance of the Zircaloy Cladding 18
- Metallographic Appearance of the Solidified Melts 29
    - General Considerations 29
    - Interpretation of the Cross Sections 38
- Mechanical and Chemical Behavior of the Spacer Grids 71
- Mechanical and Chemical Behavior of the Inner Zircaloy Liner 75
    - General Remarks 75
    - Chemical State of the Zircaloy Liner 75
- Mechanical and Chemical Behavior of the ZrO_2 Insulator 80
- Mechanical and Chemical Behavior of the Zircaloy Saddle 80
- Chemical Behavior of the Thermocouples 86
- Fuel Structure Appearance 86

DISCUSSION 93

REFERENCES 95

FIGURES

1. Radiograph of the SFD-ST fuel bundle 4
2. Comparison of structures visible in overall neutron radiograph and gross gamma scan of the SFD-ST fuel bundle 7
3. Metallographic cross section of the SFD-ST bundle at 0.055 m above the bottom of the fuel stack 8

4. Metallographic cross section of the SFD-ST bundle at 0.145 m above the bottom of the fuel stack 9

5. Metallographic cross section of the SFD-ST bundle at 0.170 m above the bottom of the fuel stack 10

6. Metallographic cross section of the SFD-ST bundle at 0.245 m above the bottom of the fuel stack 12

7. Metallographic cross section of the SFD-ST bundle at 0.270 m above the bottom of the fuel stack 13

8. Metallographic cross section of the SFD-ST bundle at 0.395 m above the bottom of the fuel stack 14

9. Metallographic cross section of the SFD-ST bundle at 0.495 m above the bottom of the fuel stack 15

10. Metallographic cross section of the SFD-ST bundle at 0.825 m above the bottom of the fuel stack 16

11. Metallographic cross section of the SFD-ST bundle at 0.915 m above the bottom of the fuel stack 17

12. Simplified schematic of the SFD-ST fuel bundle cross section 19

13. Weak external steam/cladding interactions (Rod 1B, 0°, at the 0.17-m cross-section elevation) 19

14. Zirconium-oxygen equilibrium phase diagram 21

15. Strong external and internal cladding interactions (Rod 1B, 180°, at the 0.17-m cross-section elevation) 22

16. External cladding oxidation and solidified metallic (U,Zr,O) melt between the UO_2 fuel and cladding (Rod 1B, 270°, at the 0.17-m cross-section elevation) 23

17. Localized cladding melting on the cladding external surface due to contact with a melt droplet (Rod 2A, 45°, at the 0.17-m cross-section elevation) 24

18. Local melt/cladding contact that causes zircaloy grain structure changes (Rod 4D, 80°, at the 0.055-m cross-section elevation). Note the zirconium hydrides in the cladding 25

19. Local melt/cladding contact that causes large circumferential temperature differences within the cladding and different zirconium hydride precipitation behavior (Rod 2B, 270°, at the 0.055-m cross-section elevation) 26

20. Local metallic melt/cladding contact on the cladding outside and inside surface (Rod 4A, 300°, at the 0.145-m cross-section elevation). Chemical interactions between the melt and cladding occur only on the cladding outside surface 27

21. Local melt/cladding contact on both sides of the cladding that causes azimuthal temperature differences in the cladding and different zirconium hydride precipitation behavior (Rod 4A, 300°, at the 0.145-m cross-section elevation) 28

VIII

22. Location of the maximum solidified melt layer on the internal cladding surface (Rod 4A, 300°, at the 0.145-m cross-section elevation). Note the zirconium hydride formation in the cladding 30

23. Solidified melt between fuel and cladding (Rod 4A, 300°, at the 0.145-m cross-section elevation) 30

24. Solidified melt between fuel and cladding (Rod 6B, at the 0.145-m cross-section elevation) 31

25. Strong external steam/zircaloy and internal UO_2/zircaloy cladding interactions (Rod 3A, 0°, at the 0.17-m cross-section elevation). Note the (U,Zr) alloy incursions into the α-Zr(O) phase 32

26. External steam/zircaloy and internal UO_2/zircaloy cladding interactions (Rod 3A, 270°, at the 0.17-m cross-section elevation). The (U,Zr) alloy is sandwiched by two α-Zr(O) layers 33

27. Completely oxidized cladding in contact with a ceramic melt which was initially metallic. Apparently a part of the internal cladding was molten before it was oxidized (Rod 2C, 90°, at the 0.915-m cross-section elevation) 34

28. Cladding/fuel interface. The crack in the UO_2 is partially filled with a ceramic melt which was probably metallic when it penetrated into the crack (Rod 2C, 90°, at the 0.915-m cross-section elevation) 34

29. Equilibrium phase diagram of the (U,Zr,O) ternary system at 1273 and 2273 K, from References 2 and 10 36

30. Quasi-binary α-Zr(O)/UO_2 phase diagram in mol% UO_2 and at.% UO_2, from Reference 13 37

31. Solidified ceramic and metallic melts near Rod 4D, 45°, at the 0.145-m cross-section elevation 39

32. Penetration of a metallic (U,Zr,O) melt in between the cladding and fuel gap (Rod 4B, 180°, at the 0.145-m cross-section elevation) 40

33. Solidified metallic melt near Rod 2E, 45°, at the 0.145-m cross-section elevation 41

34. Solidified melt between Rods 2E (45°) and 3D (225°) at the 0.145-m cross-section elevation 42

35. Solidified metallic melt between oxidized cladding and UO_2 fuel (Rod 4F, 270°, at the 0.145-m cross-section elevation). The solidified metallic melt was oxidized by steam later in time along open cracks 43

36. Solidified metallic (U,Zr,O) melts near Rod 2D, 45°, at the 0.055-m cross-section elevation, showing different degrees of external oxidation 45

37. Solidified metallic melt near Rod 2D, 30°, at the 0.245-m cross-section elevation, showing pronounced dendritic segregation and coring of the precipitates 46

38. Solidified metallic melt near Rod 3D, 135°, at the 0.245-m cross-section elevation 47

39. Solidified metallic melt in contact with ceramic material near Rod 6E, 90°, at the 0.27-m cross-section elevation 48

40. Metallic inclusions in the ceramic material (object number 10, 315°, at the 0.495-m cross-section elevation 49

41. Solidified heterogeneous, metallic (U,Zr,O) melt that contained solid (U,Zr)O_2 particles at temperature (debris near Rod 6E, 90°, at the 0.245-m cross-section elevation) 51

42. Heterogeneous metallic (U,Zr,O) melt attacking formerly oxidized zircaloy cladding (large, semi-metallic mass near 0° orientation at the 0.17-m cross-section elevation) 52

43. Solidified heterogeneous metallic melt that contained solid ZrO_2 and/or (U,Zr)O_2 particles at temperature (debris near Rod 6E, 45°, at the 0.27-m cross-section elevation) 53

44. Homogeneous metallic (U,Zr,O) melt penetrating along a crack into a UO_2 pellet with simultaneous chemical attack (dissolution) of the UO_2 (pellet near Rod 6E, 90°, at the 0.245-m cross-section elevation) 54

45. Cracks in the UO_2 pellet filled with a ceramic material. This ceramic was probably a formerly metallic (U,Zr,O) melt which penetrated into the cracks (see Figure 42) before it was oxidized to (U,Zr)O_2 (Rod 5B, 180°, at the 0.245-m cross-section elevation) 55

46. Solidified material in contact with UO_2 fuel pellet (Rod 4F, 90°, at the 0.245-m cross-section elevation). Note the small metallic inclusions in the two-phase ceramic matrix material which was probably a formerly metallic melt 57

47. Ceramic material, which was probably a formerly metallic melt, in contact with UO_2 fuel pellet at its circumference and within large cracks (Rod 3E, 80°, at the 0.245-m cross-section elevation) 58

48. Solidified and oxidized melt in contact with a UO_2 pellet, showing strong pore formation within the fuel, preferentially along grain boundaries. In some of the small pores, another phase is present (Rod 4B, 135°, at the 0.245-m cross-section elevation) 59

49. Detail of the uranium-oxygen phase diagram, from Reference 2 60

50. Attack of the UO_2 outer surface by a formerly metallic (U,Zr,O) melt, as well as penetration of the melt into UO_2 cracks before it was oxidized by steam (Rod 6E, 180°, at the 0.27-m cross-section elevation) 61

51. Uranium-zirconium phase diagram, from Reference 2 62

52. Melt penetration into UO_2 pellet cracks (object number 4, 280°, at the 0.495-m cross-section elevation) 64

53. Melt penetration into UO_2 pellet interfaces (dishing volume) (object number 5 at the 0.495-m cross-section elevation) 65

X

54. Onset of UO_2 fuel melting in pellet cracks (Rod 4E, at the 0.915-m cross-section elevation) 66

55. Transition region from porous, previously molten UO_2 pellet to as-fabricated fuel structure with densified zone in between (Rod 2D, 0°, at the 0.915-m cross-section elevation) 67

56. Solidified ceramic material with small metallic inclusions (between Rods 4D, 5D, and 4E, 5E, at the 0.145-m cross-section elevation) 68

57. Ballooned cladding touching each other with subsequent oxidation. Melt attack occurred on the cladding OD and ID surfaces as well as the fuel surface (object number 1, 0°, at the 0.495-m cross-section elevation) 69

58. Ceramic phase formation located between the zircaloy liner and Rod 6E at the 0.145-m cross-section elevation. This is a typical microstructure of a solidified multicomponent system, probably a eutectic chemical interaction between the Al_2O_3 temperature profile detector tube and UO_2 or $(U,Zr)O_2$ 70

59. Microstructure in the same region as that of Figure 58 71

60. Spacer grid junctions between Rods 4F and 5E (upper photograph) and Rods 5F and 6E (lower photograph) at the 0.055-m cross-section elevation 72

61. Metallographic appearance of the previously molten Inconel 718 spacer grids in contact with solidified ceramic material near Rod 6E, 135°, at the 0.055-m cross-section elevation 73

62. Metallographic appearance of the chemical interaction between the melt and partially molten Inconel 718 spacer grid between Rods 4C and 4D at the 0.055-m cross-section elevation 74

63. Deformed and undeformed zircaloy liner in different chemical oxidation states at the 0.145-m cross-section elevation 76

64. Chemical state of the zircaloy liner remnant at the 0.245-m cross-section elevation 77

65. Appearance of the zircaloy liner, 180°, at the 0.915-m cross-section elevation. The metallic part of the liner reached temperatures above 2223 K, the melting point of oxygen-stabilized α-Zr(O) 78

66. Appearance of the zircaloy liner, 135°, at the 0.915-m cross-section elevation. The metallic part of the liner reached temperatures above 2223 K, the melting point of oxygen-stabilized α-Zr(O) 79

67. Possible zircaloy liner remnant which is almost completely transformed into ZrO_2 (near the saddle, 90°, at the 0.245-m cross-section elevation) 81

68. High-density ZrO_2 cylinder (near the saddle, 90° at the 0.245-m cross-section elevation) 82

69. Attack of a ZrO_2 insulator cylinder by a (U,Zr,O) melt with partial disintegration (object number 8 at the 0.495-m cross-section elevation) 83

70. Chemical attack of a ZrO_2 insulator cylinder by a (U,Zr,O) melt with partial disintegration (near object number 4, 315°, at the 0.495-m cross-section elevation) 84

71. Zircaloy saddle, 180°, at the 0.915-m cross-section elevation 85

72. Zircaloy saddle, 0°, at the 0.17-m cross-section elevation 85

73. Cladding internal TC in Rod 3A, 315°, at the 0.17-m cross-section elevation (TC wires, W/Rh; insulation, BeO; sheath, Zr/ZrO_2 duplex tube) 87

74. Fuel centerline TC in Rod 3C at the 0.055-m cross-section elevation (TC wire, W/Rh; insulation, BeO; sheath, Mo/Re alloy) 88

75. Debris near cladding remnant on object number 11, 60°, at the 0.495-m cross-section elevation (may be Be/BeO eutectic) 89

76. Fuel across the pellet cross section shows different conditions (object number 2 at the 0.495-m cross-section elevation). Etching reveals a very fine structure within a few UO_2 regions and pore formation at the grain boundaries 90

77. Fuel structure at the pellet center of Rod 4D at the 0.27-m cross-section elevation 91

78. Fuel structure at the pellet/melt interface of Rod 6E, 90°, at the 0.17-m cross-section elevation 92

METALLOGRAPHIC EXAMINATION OF THE SEVERE FUEL DAMAGE SCOPING TEST (SFD-ST) FUEL ROD BUNDLE CROSS SECTIONS

INTRODUCTION

In a severe fuel damage (SFD) accident, the fuel and cladding may reach temperatures up to the melting point. With increasing fuel and cladding temperatures, fuel rod damage will occur in the light water reactor (LWR) core in a variety of forms. Since zircaloy is thermodynamically unstable with respect to steam and uranium dioxide (UO_2) fuel, chemical interactions will take place which become significant at temperatures above 1273 K. To predict fuel rod behavior in SFD accidents, a quantitative description of the steam/zircaloy, fuel/zircaloy, and zircaloy/Inconel[a] chemical interactions as a function of temperature and time is needed. For this reason, in-pile and out-of-pile[1-12] experiments have been performed to analyze and characterize fuel rod damage.

The United States Nuclear Regulatory Commission (NRC) has initiated an internationally sponsored[b] severe fuel damage research program in the Power Burst Facility (PBF) to investigate LWR fission product release, fission product deposition, fission product transport, hydrogen release, and fuel behavior and coolability during severe fuel damage accidents. The Severe Fuel Damage Scoping Test (SFD-ST), the first test in the four-test series, was conducted on October 29, 1982. A 32-rod bundle of pressurized-water-reactor (PWR)-type fuel rods, 0.91 m long and enclosed in an insulated shroud, was subjected first to a slow heatup (to about 1373 K in the lower part of the fuel bundle and to about 1773 K in the upper portion of the bundle) and then a rapid heatup to the maximum test temperatures, followed by coolant reflood and quenching.

The SFD-ST fuel rod bundle was examined posttest using a variety of nondestructive and destructive techniques. Considerable disruption of the fuel bundle occurred during the transient. This report presents the results of the metallographic examination of the SFD-ST bundle cross sections. In order to understand the phenomena that occurred during Test SFD-ST, it is important to describe the severe fuel damage scenario in general.

In an SFD accident that leads to fuel rod melting, the following processes and chemical reactions can take place as the temperature rises:

- Plastic deformation and bursting or collapsing of the cladding, depending on the differential pressure.
- Oxidation and embrittlement of the cladding, which may result in rod fragmentation.
- Oxidation of the fuel.
- Melting of the metallic zircaloy or the metallic oxygen-stabilized alpha zircaloy [α-Zr(O)] phase.
- Interactions between solid and/or molten zircaloy and solid fuel, with partial dissolution of UO_2.
- Formation of an α-Zr(O)/zirconium dioxide (ZrO_2) eutectic.
- Eutectic and monotectic reactions between α-Zr(O) and UO_2.
- Disintegration and dissolution of solid UO_2 by molten zircaloy, forming a homogeneous or heterogeneous metallic (U,Zr,O) melt.
- Melting of ZrO_2 and UO_2, forming a ceramic (U,Zr,O) melt.

In addition to the above-described chemical interactions, localized reactions between the spacer grids (Inconel 718) and zircaloy cladding, as well as the absorber materials (Ag-In-Cd alloy) and cladding, will take place at temperatures below 1273 K. All of these interactions are of concern in an SFD accident, since relocation and/or solidification of the resulting fragments or melt may result in coolant channel blockages.

---

[a] Mention of specific products and/or manufacturers in this document implies neither endorsement or preference nor disapproval by the U.S. Government, any of its agencies, or EG&G Idaho, Inc., of the use of a specific product for any purpose.

[b] Partners of the program include Belgium, Canada, Federal Republic of Germany, Finland, Italy, Japan, Netherlands, Republic of Korea, Spain, Sweden, United Kingdom, American Institute of Taiwan, and the United States Nuclear Regulatory Commission.

Elevated fuel rod temperatures cause a variety of changes in the fuel and cladding microstructure, resulting in typical metallographic structures for the reaction products. These phenomena include grain growth, phase transformations, porosity distribution, type and extent of oxidation, formation of precipitates, cladding melting, UO_2 and/or ZrO_2 dissolution, and the solidification of melts. Since most of these phenomena leave characteristic patterns in the resulting microstructures of the various phases, these microstructures can be compared with those obtained in well defined out-of-pile annealing or interaction experiments.[1-9,12] This is the only tool which could be used to make any statement with respect to the chemical interactions that occurred in Test SFD-ST, since qualitative or quantitative chemical analyses were not available. In many cases, one could therefore only postulate what may have happened to the fuel rods during the test and what chemical composition the resulting reaction products may have.

It is particularly important to emphasize that many complex phenomena occurred simultaneously or in series during the SFD test transient, due to large variations in individual rod temperatures and local steam flow rate, and also because of cladding and fuel relocation. The resultant solid and liquid phases encompass a wide range of initial and final chemical compositions. Therefore, what can be identified through posttest metallographic examinations at room temperature is only the chemical and physical state of the reaction products that were present when quenching, or cooldown, of the fuel rod bundle occurred. In a few cases, the time-dependent material behavior during the accident scenario may be postulated.

It is also important to keep in mind the fact that the microstructure (number of phases) of the components of reaction products at room temperature may be different than that which exists under the physical and chemical conditions at test temperature. A microstructure that looks multiphase at room temperature may be singlephase at high temperatures. This can have an influence on some physical properties, such as the meltdown behavior of liquid phases determined by the wetting properties between the melt and the solid substrate.[7,10] Furthermore, as a result of the fast cooldown rate, the phases may not be under equilibrium conditions. For this reason, the application of available phase equilibrium diagram information is limited.

FUEL ROD BUNDLE SECTIONING

The SFD-ST fuel rod bundle was first examined by neutron radiography, a nondestructive examination technique used to help determine posttest fuel rod bundle geometry and at which axial elevations bundle sectioning should be performed. Radiographs were taken in seven axial positions, two of which were radiographed at multiple angles for tomography.

The overall neutron radiographs are shown, split into three axial sections, in Figures 1(a), (b), and (c). The bottom of the bundle contained instrumentation leads and the tie plate, and the bottom end caps and insulation pellets can be seen in each rod. Below the bottom grid spacer (centered 0.05 m above the bottom of the fuel stack), the fuel rods remained intact; no molten material or debris can be seen. Molten material has moved down into the rod stub region, which extends from 0.72 to 0.198 m. Above the rod stubs is a large, nearly spherical mass of rod segments, about 0.07 m in diameter, cemented together with previously liquid material. Above the mass is a debris bed of fairly uniform consistency, probably composed primarily of large cladding chunks and fuel pieces greater than one-fourth the size of a fuel pellet. The middle grid spacer is not visible in the neutron radiographs. In addition, sections of fuel rods are visible at the upper end of the debris bed. These rod segments are probably highly oxidized, and many of the segments are lying at odd angles. There is a gap in the fuel stacks just below the top grid spacer, and the upper ends of the fuel rods are about 0.11 m above their original location. All of the structural components unique to the SFD test train are apparent in the neutron radiographs.

A comparison between the location of the various structures in the neutron radiographs and the gross gamma scan is shown in Figure 2. The comparison illustrates that very little relocation of the fuel bundle occurred during handling between the gross gamma scan and the neutron radiography. The high gamma activity measured at elevations corresponding to the location of the previously molten material confirms dissolution of UO_2 by molten cladding. The gamma scan does not show a discontinuity below the mass, as seen in the neutron radiograph, but rather shows it about 0.10 m lower, below most of the previously molten structure. A portion of the solidified structure evidently broke off during handling and fell onto the rod stubs above the bottom grid.

The SFD-ST fuel rod bundle was then encapsulated in epoxy and sectioned, permitting a detailed examination of the chemical interaction of the materials and retained fission products in the bundle, as well as a comparison of bundle geometry via neutron radiograph and metallographic cross sections. This procedure, performed remotely in a hot cell facility, is described below.

After evaluating three different epoxy systems, one composed of dye-impregnated Dow Epoxy Resin 332 and Jeffamine T-403,[a] mixed at a ratio of 100 to 45, respectively, was chosen as the SFD-ST bundle encapsulant. This epoxy exhibited good debris penetration and polishing characteristics and also showed little heating during the curing stage. The volume of epoxy needed was calculated to be ∼7 L prior to encapsulation, based upon the assumption that the insulation region would not fill with epoxy. However, during the potting operation, 9.5 L of epoxy were required to fill the bundle, implying complete epoxy penetration of the insulation region and all voids. Sectioning of the bundle confirmed this result.

The sectioning saw was manufactured by Felker and included a 35.5-cm-diameter by 0.317-cm-thick, diamond-embedded steel blade. The saw had a traversing table with an average manual feed rate of 0.071 cm/min and a blade speed of ∼1600 rpm. Twenty-one 0.0254-m-thick metallographic sections were cut and vacuum-impregnated with epoxy into metallographic mounts. Analysis of these sections shows excellent penetration of the epoxy into the debris and insulation.

Nine cross sections, representative of all of the major regions in the bundle, have been polished. The cross sections are located at 0.055, 0.145, 0.170, 0.245, 0.270, 0.395, 0.495, 0.825, and 0.915 m above the bottom of the fuel stack. All samples were viewed from the bottom surface with counterclockwise orientations; however, to be consistent with the neutron tomography results, the photographs of the metallographic cross sections are reversed in this report. Therefore, all samples appear as if they were viewed from the top, and all orientations are clockwise.

---

[a] Dow Epoxy Resin 332 manufactured by Dow Chemical Co., Midland, MI; Jeffamine T-403 manufactured by Jefferson Chemical Co., a subsidiary of Texaco, BelAire, TX.

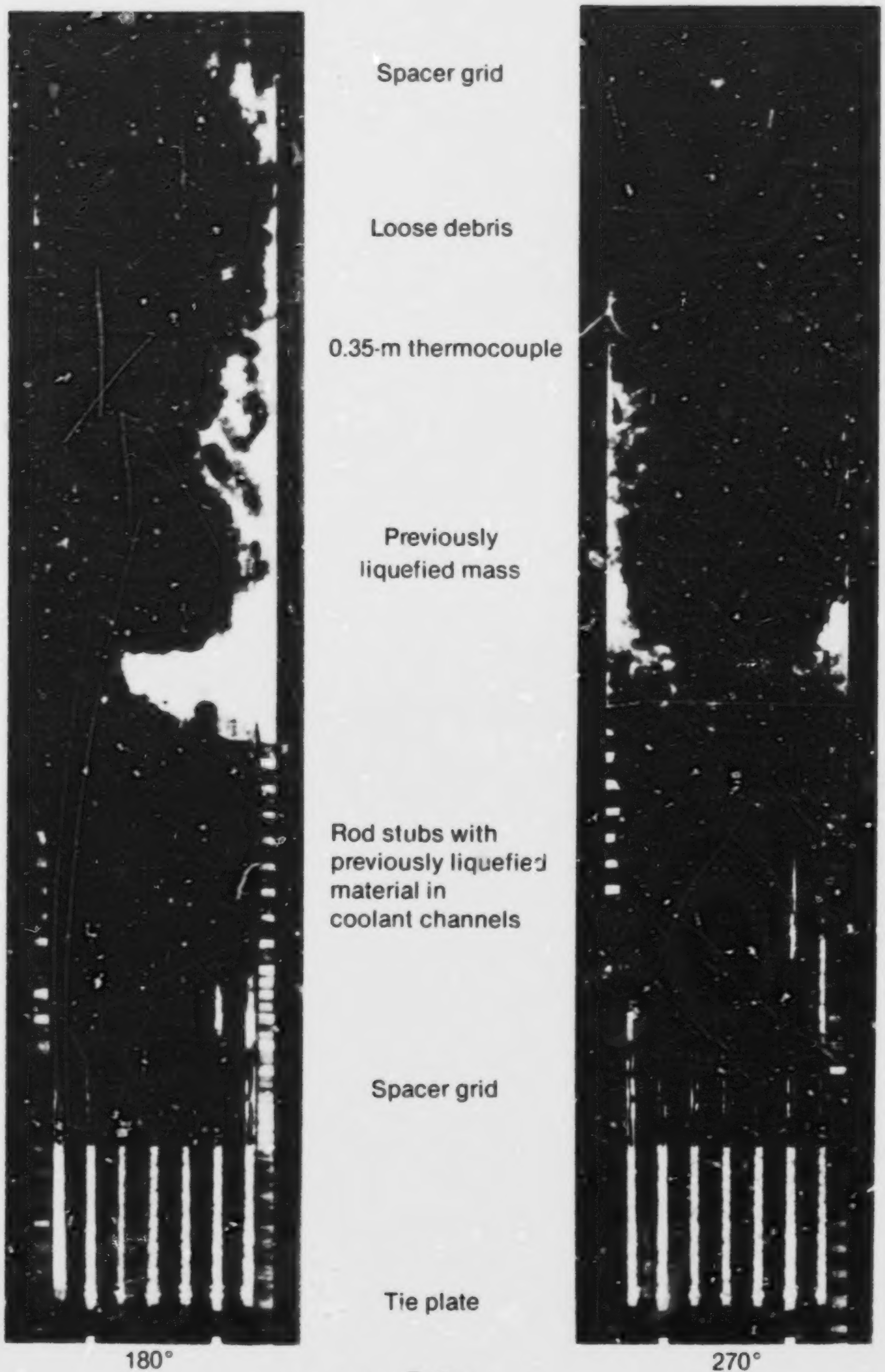
Spacer grid
Loose debris
0.35-m thermocouple
Previously liquefied mass
Rod stubs with previously liquefied material in coolant channels
Spacer grid
Tie plate
180°
270°

a. Bottom

Figure 1. Radiograph of the SFD-ST fuel bundle.

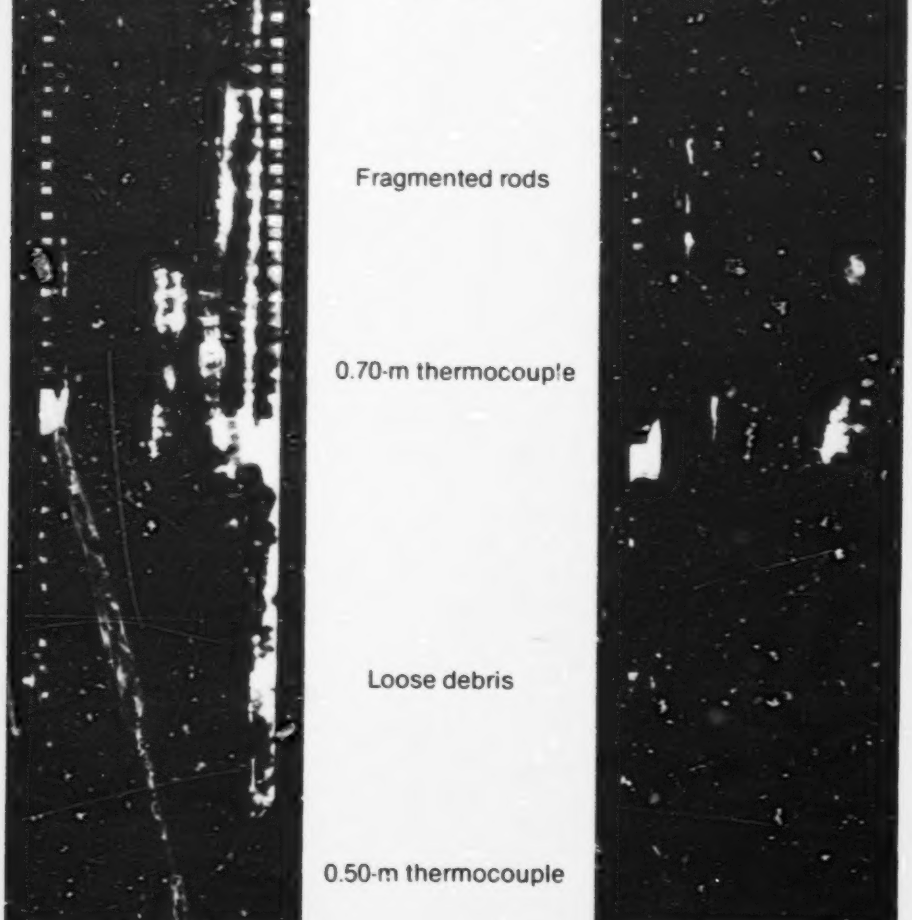
Spacer grid
Fragmented rods
0.70-m thermocouple
Loose debris
0.50-m thermocouple

180°

270°

b. Middle

Figure 1. (Continued)

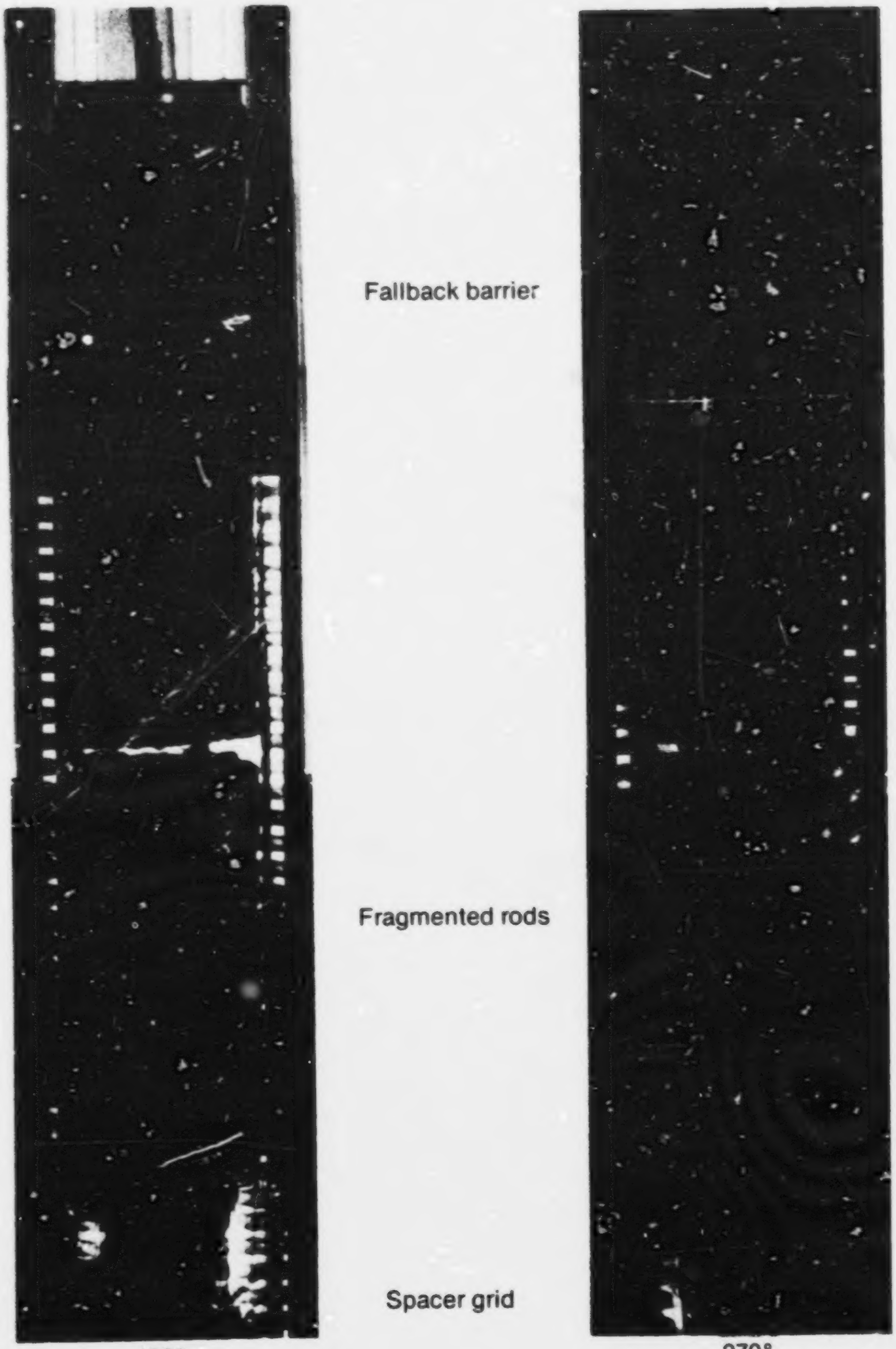
Fallback barrier
Fragmented rods
Spacer grid

180°   270°

c. Top

Figure 1. (Continued)

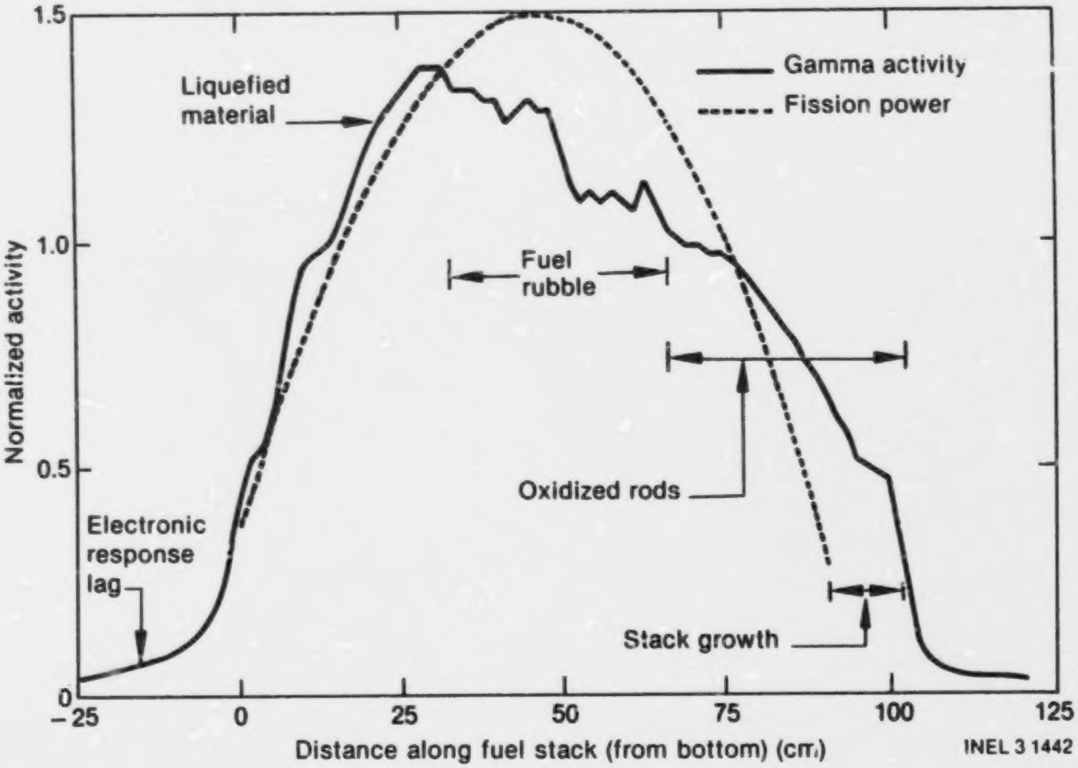

Figure 2. Comparison of structures visible in overall neutron radiograph and gross gamma scan of the SFD-ST fuel bundle.

The cross section at 0.055 m (Figure 3) shows the fuel rods to be intact at this elevation. The grid spacer, the fuel and cladding thermocouples (TCs), the zircaloy inner liner, and much of the insulation material are also apparent. Some of the low-density ZrO_2 material in the insulation region may have been washed out by the epoxy during encapsulation. Small filings from the holes milled through the shroud for epoxy injection were transported to this elevation and appear in the insulation region at about the 240° location. Previously molten material has relocated to the areas between the fuel rods and the grid spacer. The detailed metallography revealed that the metallic and ceramic particles were molten when they reached this elevation, then solidified in place causing local hot spots. The chemical and thermal attack by these melts was stronger on the spacer grid than on the cladding.

The cross section at 0.145 m, about halfway up through the rod stubs, is shown in Figure 4. The fuel rod array is still nearly intact; however, a significant amount of molten metallic and ceramic material has relocated to this elevation. The inner liner and insulation are intact in most regions, except for a few places where the molten material has flowed into the insulation region. The fuel centerline TCs are intact, but some of the TCs on the inside surface of the cladding have been significantly damaged. Two distinct molten regions are apparent, both of which probably contain zirconium, uranium, and oxygen in different amounts. However, the lighter, denser, metallic-looking region probably has a lower oxygen content than the darker, more porous, ceramic-looking region. There is a buildup of darker material on the outer surface of the lighter material, suggesting that further steam oxidation of the metallic material occurred.

The cross section at 0.170 m, also in the rod stub region, is shown in Figure 5. Approximately 15 of the rods are in their original positions in the fuel rod array. The cladding around all but two of the 15 rods was either totally oxidized or melted. The previously molten material is of a uniform dark color and highly porous. Much of the loose debris

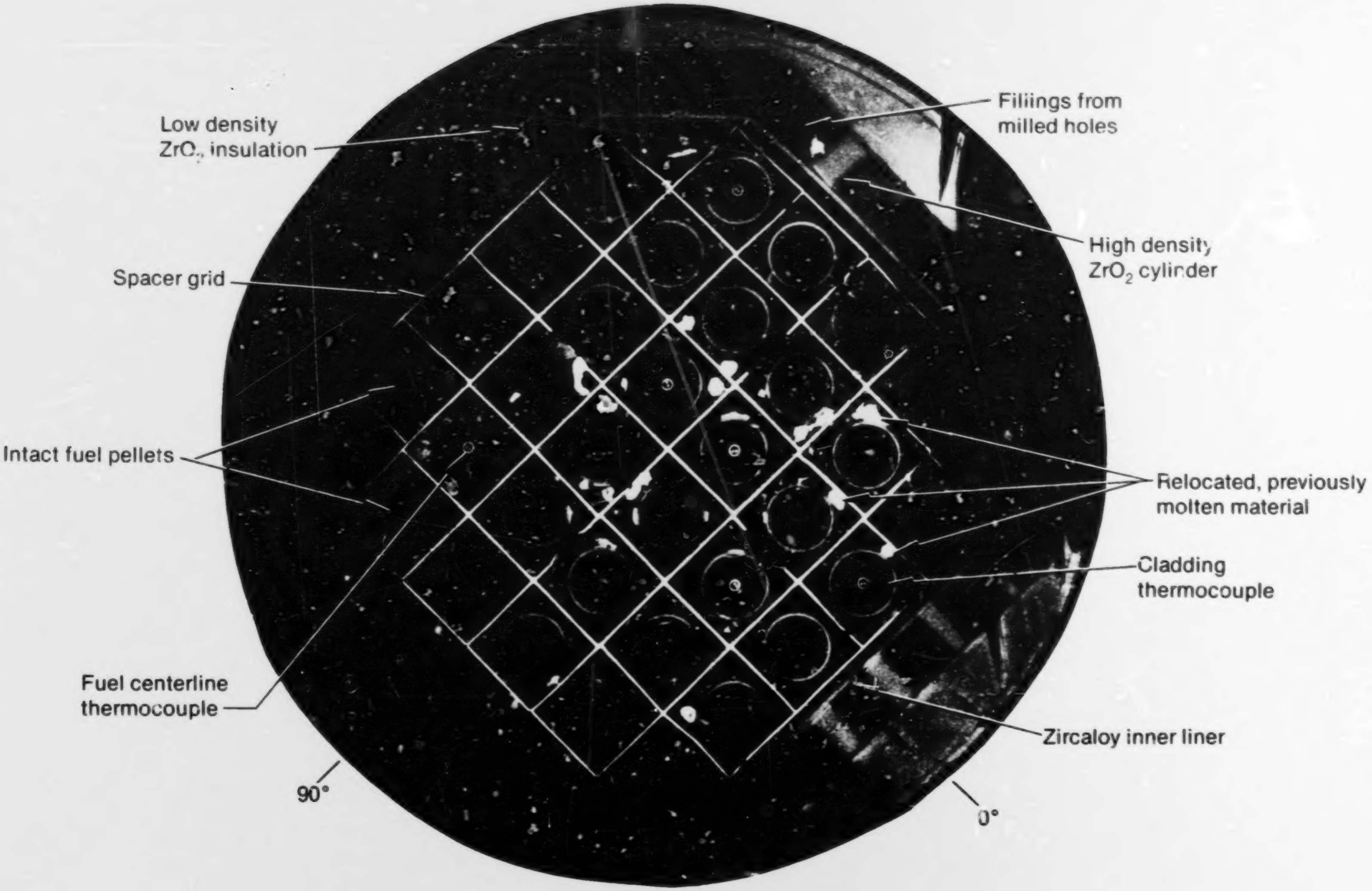
Low density
ZrO₂ insulation
Filings from
milled holes
High density
ZrO₂ cylinder
Spacer grid
Intact fuel pellets
Relocated, previously
molten material
Cladding
thermocouple
Fuel centerline
thermocouple
Zircaloy inner liner
90°
0°

Figure 3. Metallographic cross section of the SFD-ST bundle at 0.055 m above the bottom of the fuel stack.

BEST COPY AVAILABLE

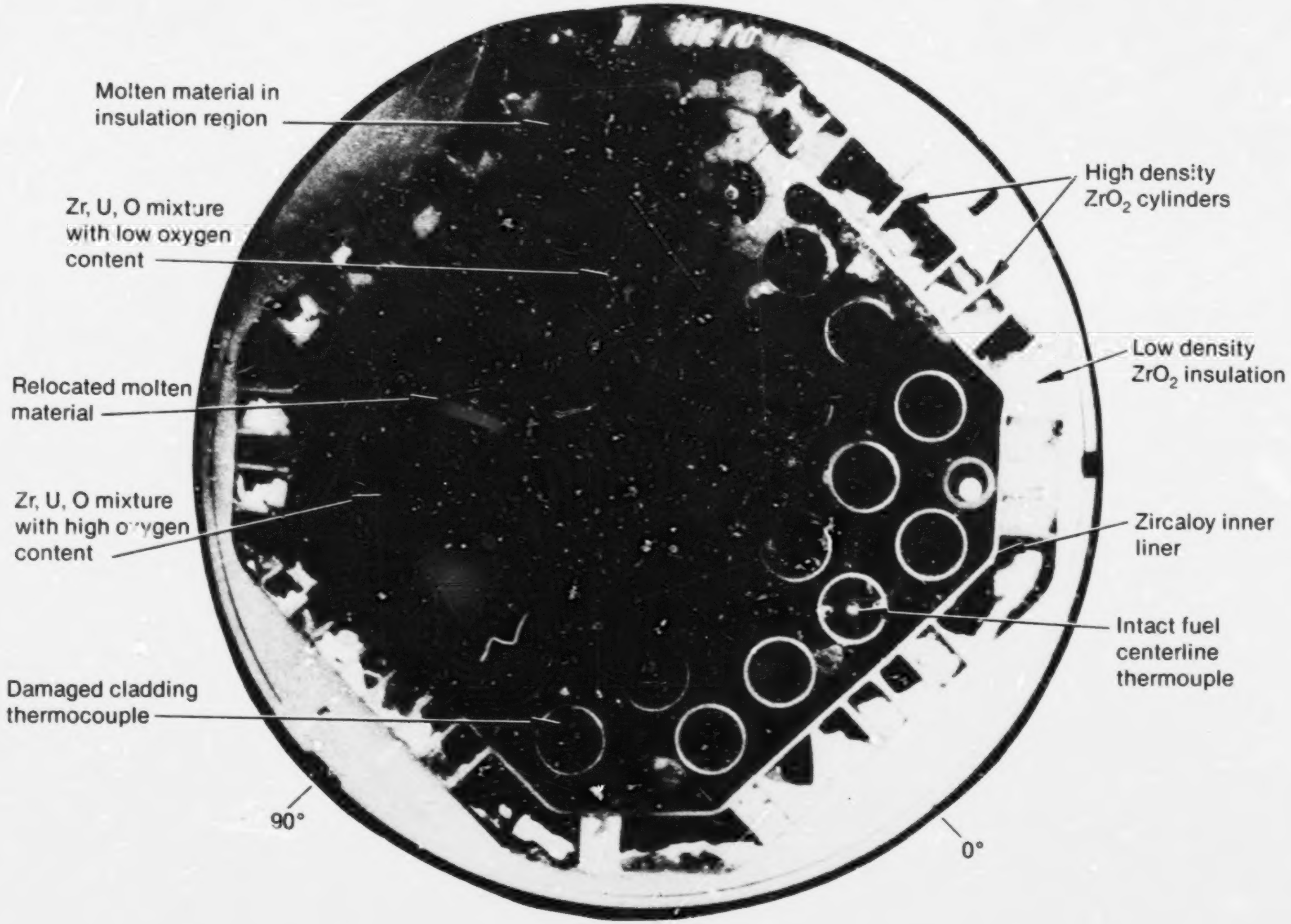
Molten material in insulation region
Zr, U, O mixture with low oxygen content
Relocated molten material
Zr, U, O mixture with high oxygen content
Damaged cladding thermocouple
High density ZrO_2 cylinders
Low density ZrO_2 insulation
Zircaloy inner liner
Intact fuel centerline thermouple
90°
0°

Figure 4. Metallographic cross section of the SFD-ST bundle at 0.145 m above the bottom of the fuel stack.

BEST COPY AVAILABLE

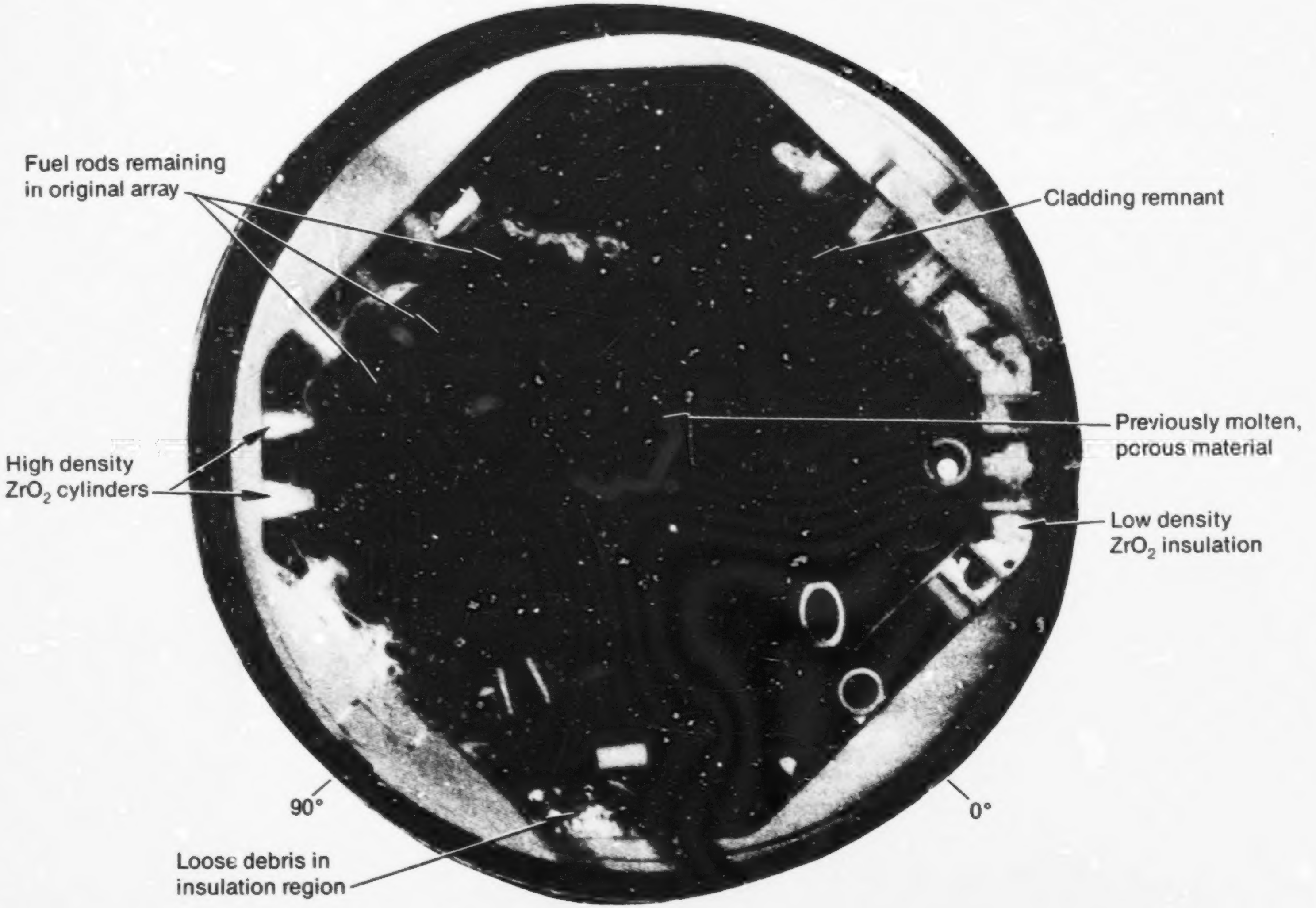
Fuel rods remaining in original array
Cladding remnant
Previously molten, porous material
High density ZrO_2 cylinders
Low density ZrO_2 insulation
90°
0°
Loose debris in insulation region

Figure 5. Metallographic cross section of the SFD-ST bundle at 0.170 m above the bottom of the fuel stack.

has fallen into the insulation region between 0° and 90°. About 50% of the zircaloy liner and ZrO_2 insulation has disappeared.

Two cross sections through the large, nearly spherical mass are shown in Figures 6 and 7 (0.245 and 0.270 m). Twenty-three of the rods (less cladding) are still in their original positions in the fuel rod array and have been attacked (dissolved) to different extents. The previously molten material surrounding the rods is uniformly dark and highly porous. The cracks in the fuel pellets contain previously molten material, suggesting that the melt was of relatively low viscosity when it relocated to this region. The diameter of the mass at these elevations is about 0.07 m. None of the insulation region is intact, and much of the loose debris surrounding the mass is from the insulation. The lighter metallic material within the ceramic material at the 0.245-m elevation probably consisted of remnants of the fuel and cladding TCs, in particular the TC insulation material. One small section of the inner liner is also evident at this elevation.

Close inspection of the fuel pellets within the mass at the 0.270-m elevation (Figure 7) reveals that Rod 1F has shifted diagonally. This shift is not apparent at the preceding elevation. This elevation also contained less TC material. The previously molten material appears to be a little less porous, but the fuel pellets have been more strongly attacked. The zircaloy liner and ZrO_2 insulation materials have completely disappeared.

The fuel rod bundle cross sections from the debris region (at 0.395 and 0.495 m) are shown in Figures 8 and 9. The debris contained large fuel particles (generally greater than one-quarter the size of a fuel pellet), some heavily oxidized cladding sections, and considerable insulation material. It is difficult to distinguish the densely packed fuel rod debris from the insulation and previously molten fuel rod materials. The packing of the debris into the lower half of the cross section is due to the orientation of the fuel rod bundle during shipping and epoxy encapsulation. The grid spacer that was originally located at the 0.395-m elevation is no longer present, although there is evidence of some previously molten material which might contain Inconel.

Very little debris is apparent at the 0.825-m elevation, shown in Figure 10. The insulation is mostly intact; however, the inner liner was deformed and highly oxidized. The ZrO_2 insulation material was still present. Most of the cladding and fuel have relocated away from this elevation. The grid spacer that was originally located at this elevation is entirely gone, probably due to relocation of material during the test.

Figure 11 shows the cross section taken at 0.915 m, in which most of the fuel rod array is present. More apparent melting and oxidation of the zircaloy cladding occurred at this elevation than at the lower elevations. A few UO_2 pellets show a foam-like appearance, which may be caused by some onset of fuel melting. Some liquefaction of the UO_2 fuel occurred as a result of cladding melting. About 50% of the deformed and oxidized zircaloy liner was still present; however, more than 60% of the ZrO_2 insulator material was gone.

BLANK PAGE

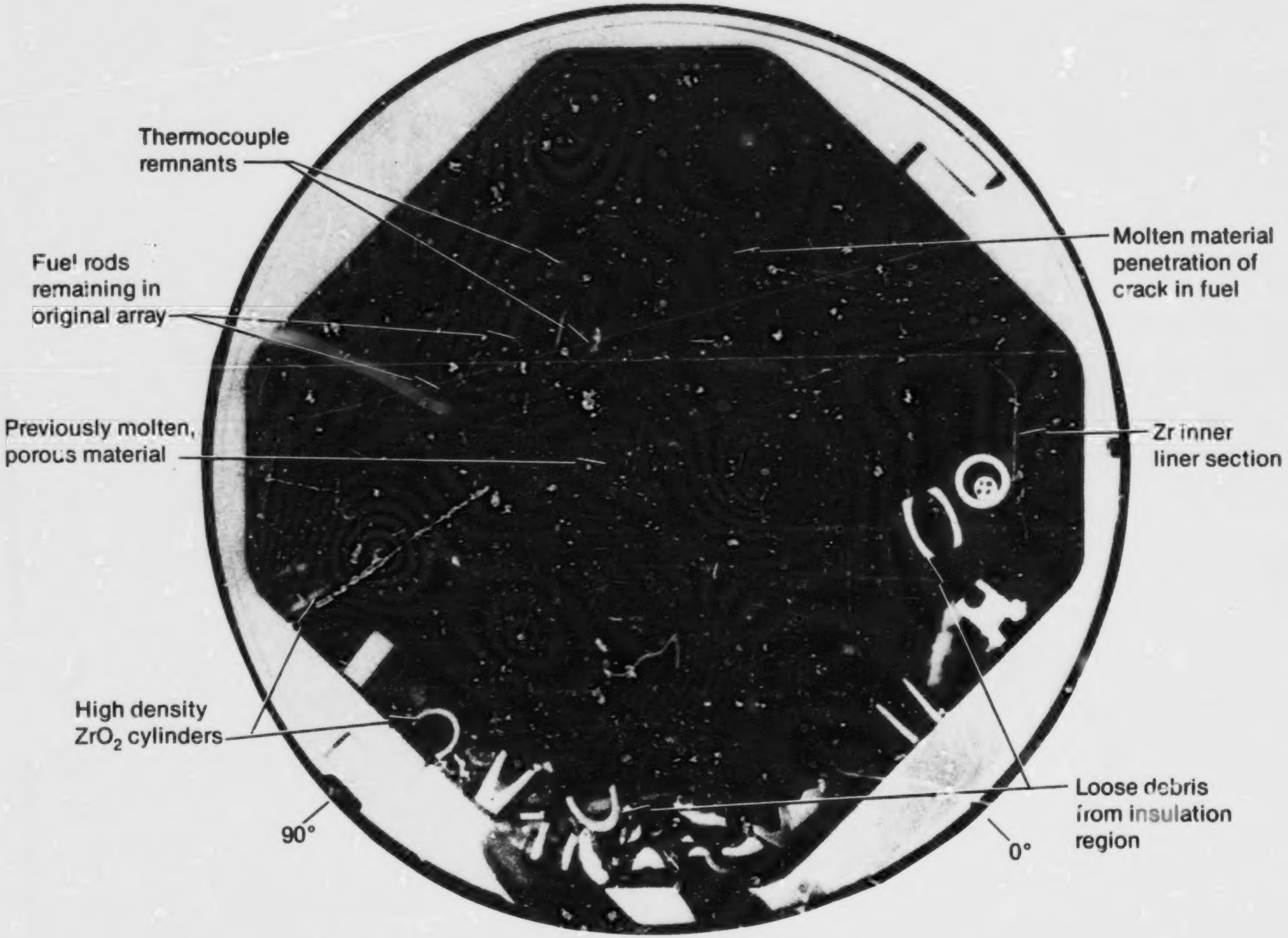
Thermocouple remnants
Fuel rods remaining in original array
Previously molten, porous material
High density ZrO_2 cylinders
90°
Molten material penetration of crack in fuel
Zr inner liner section
Loose debris from insulation region
0°

Figure 6. Metallographic cross section of the SFD-ST bundle at 0.245 m above the bottom of the fuel stack.

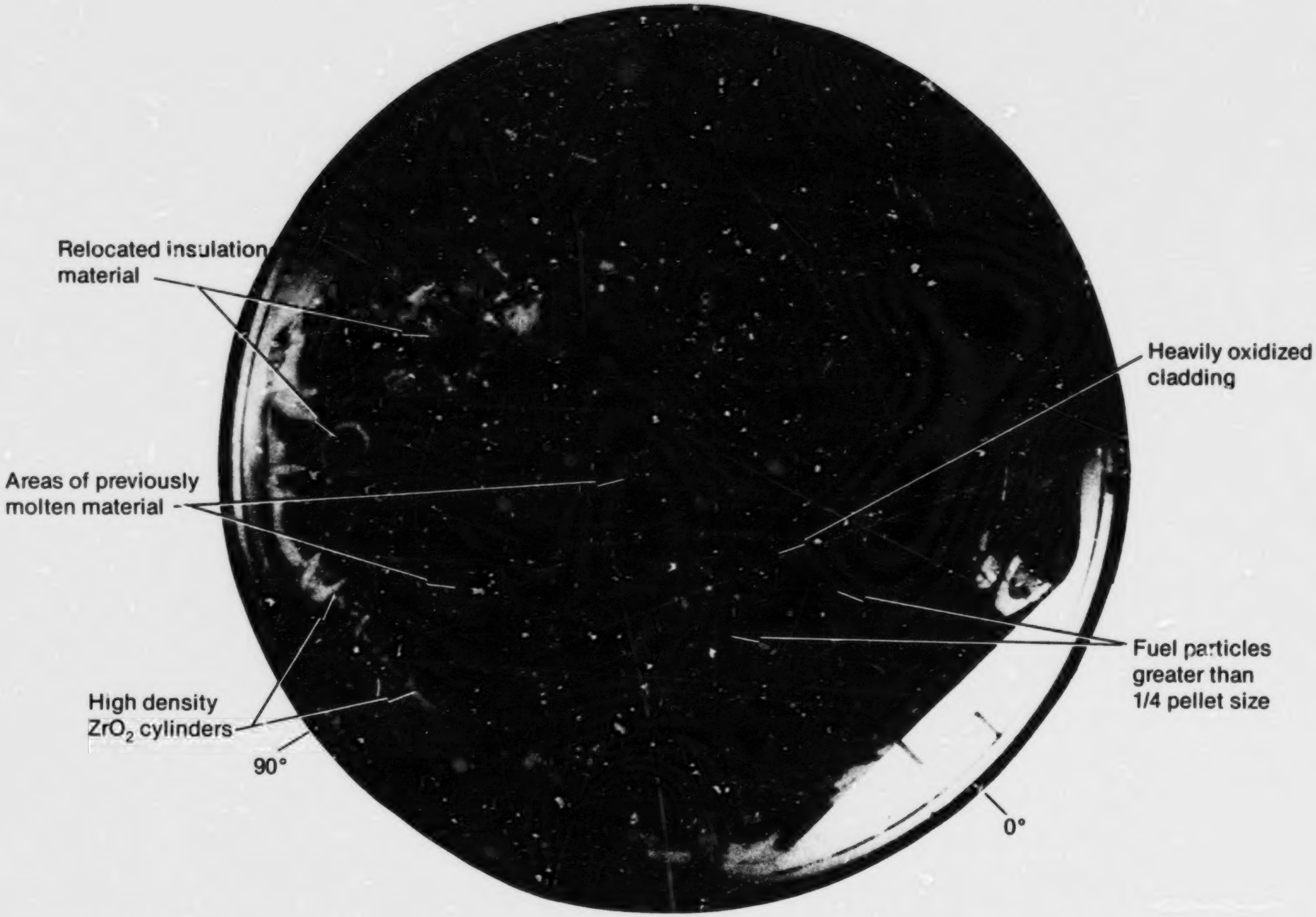
Relocated insulation material
Heavily oxidized cladding
Areas of previously molten material
Fuel particles greater than 1/4 pellet size
High density ZrO_2 cylinders
90°
0°

Figure 7. Metallographic cross section of the SFD-ST bundle at 0.270 m above the bottom of the fuel stack.

BEST COPY AVAILABLE

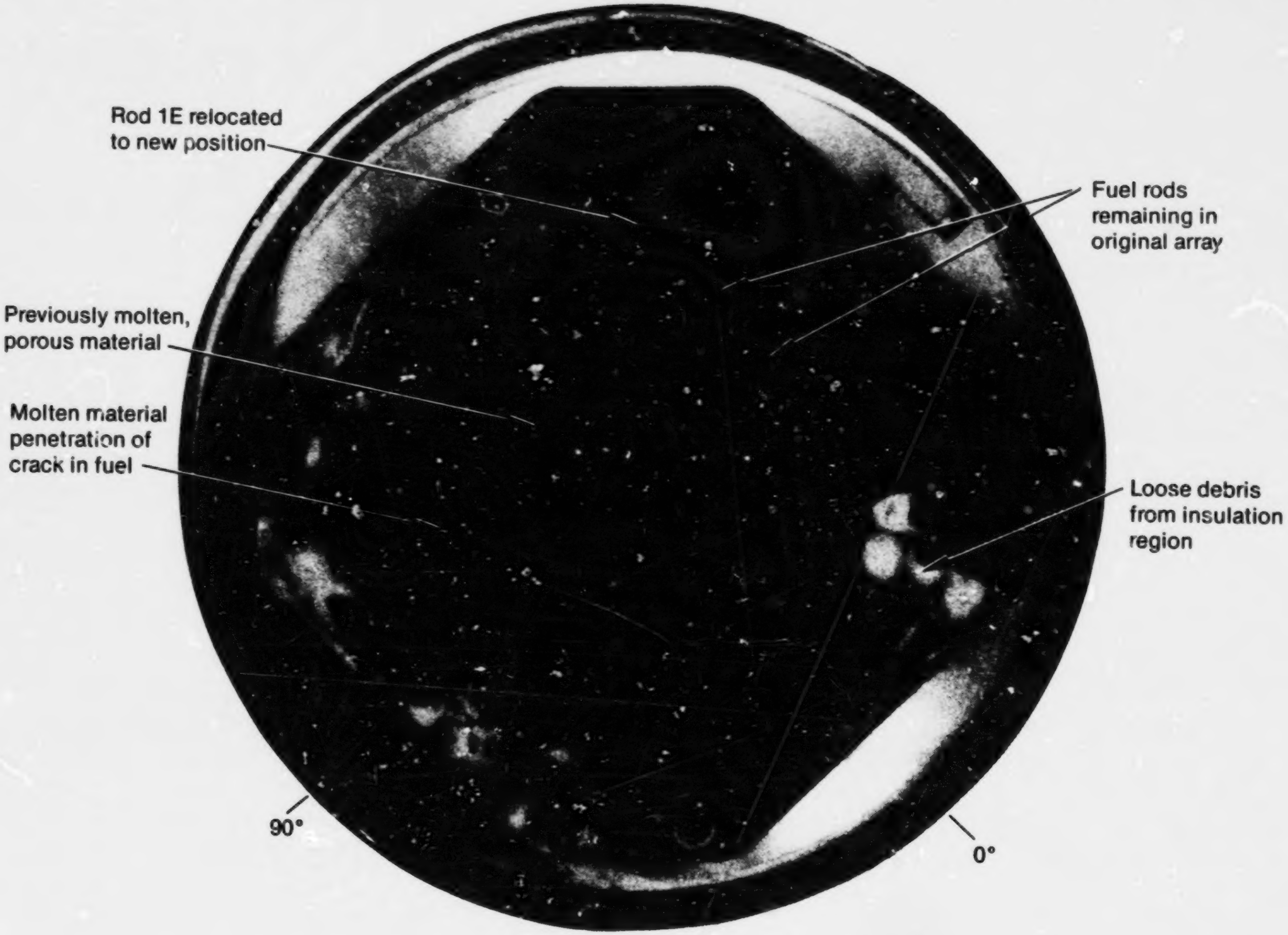
Rod 1E relocated to new position
Fuel rods remaining in original array
Previously molten, porous material
Molten material penetration of crack in fuel
Loose debris from insulation region
90°
0°

Figure 8. Metallographic cross section of the SFD-ST bundle at 0.395 m above the bottom of the fuel stack.

BEST COPY AVAILABLE

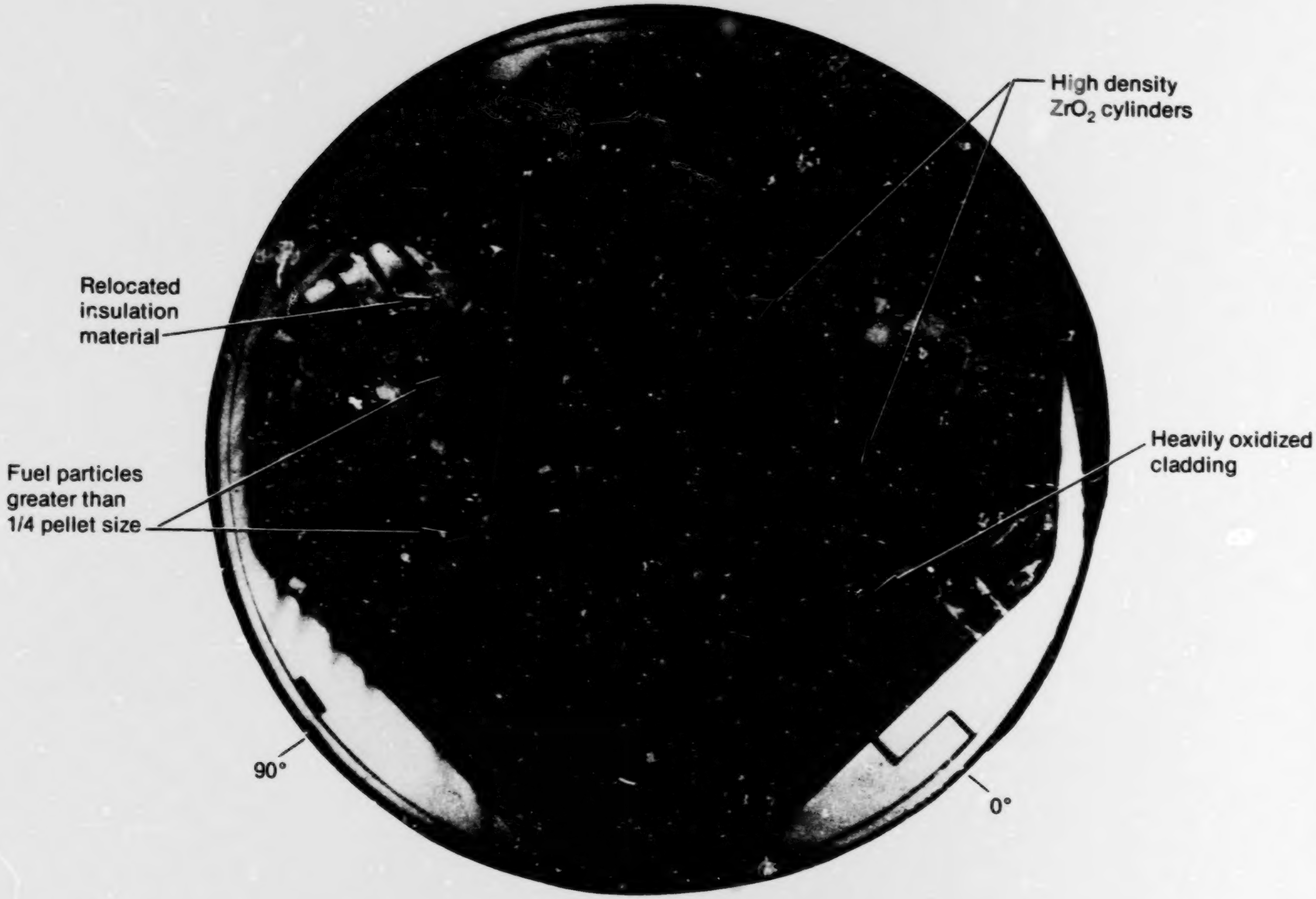
High density
ZrO_2 cylinders
Relocated
insulation
material
Heavily oxidized
cladding
Fuel particles
greater than
1/4 pellet size
90°
0°

Figure 9. Metallographic cross section of the SFD-ST bundle at 0.495 m above the bottom of the fuel stack.

BEST COPY AVAILABLE

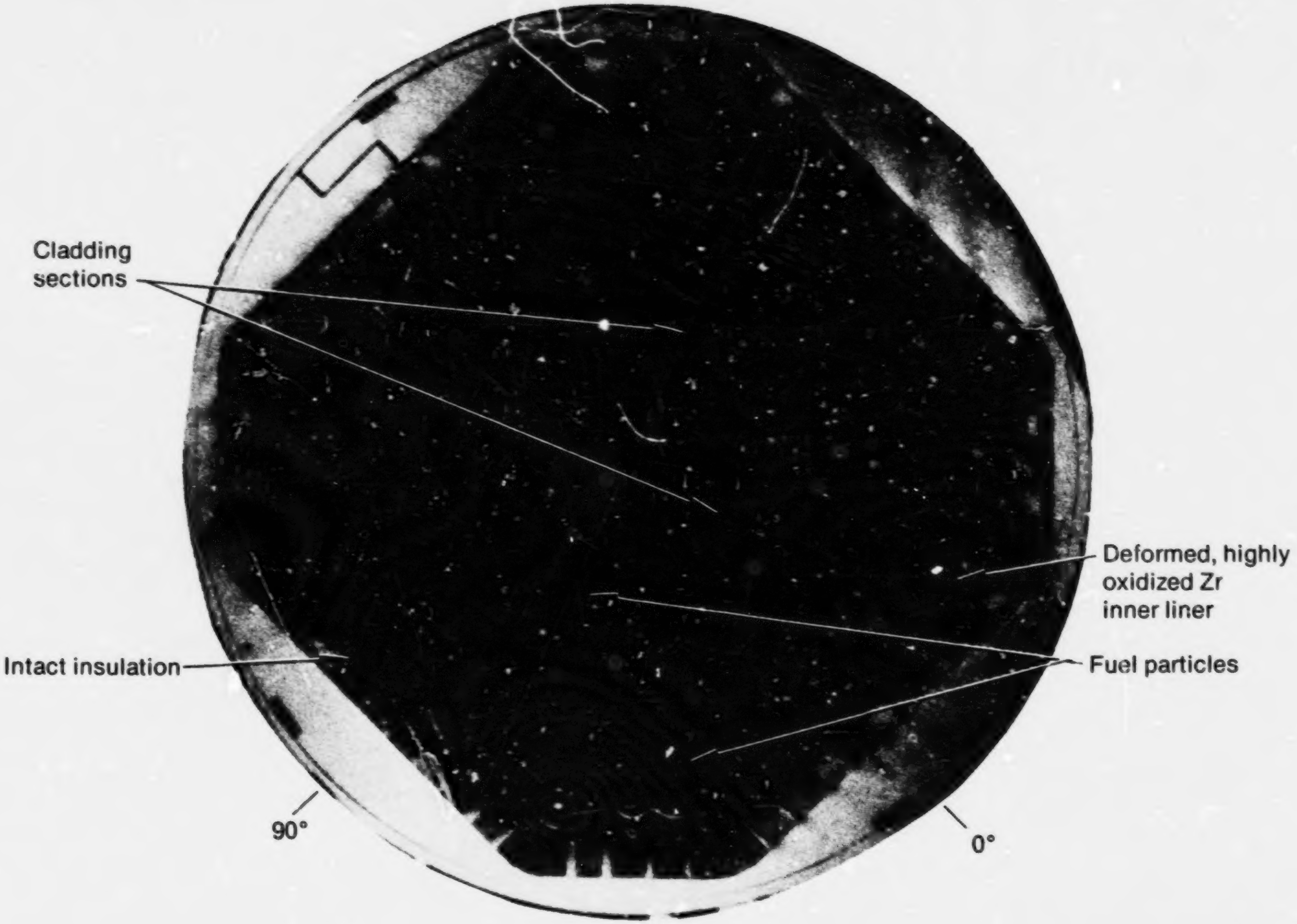
Cladding sections
Deformed, highly oxidized Zr inner liner
Intact insulation
Fuel particles
90°
0°

Figure 10. Metallographic cross section of the SFD-ST bundle at 0.825 m above the bottom of the fuel stack.

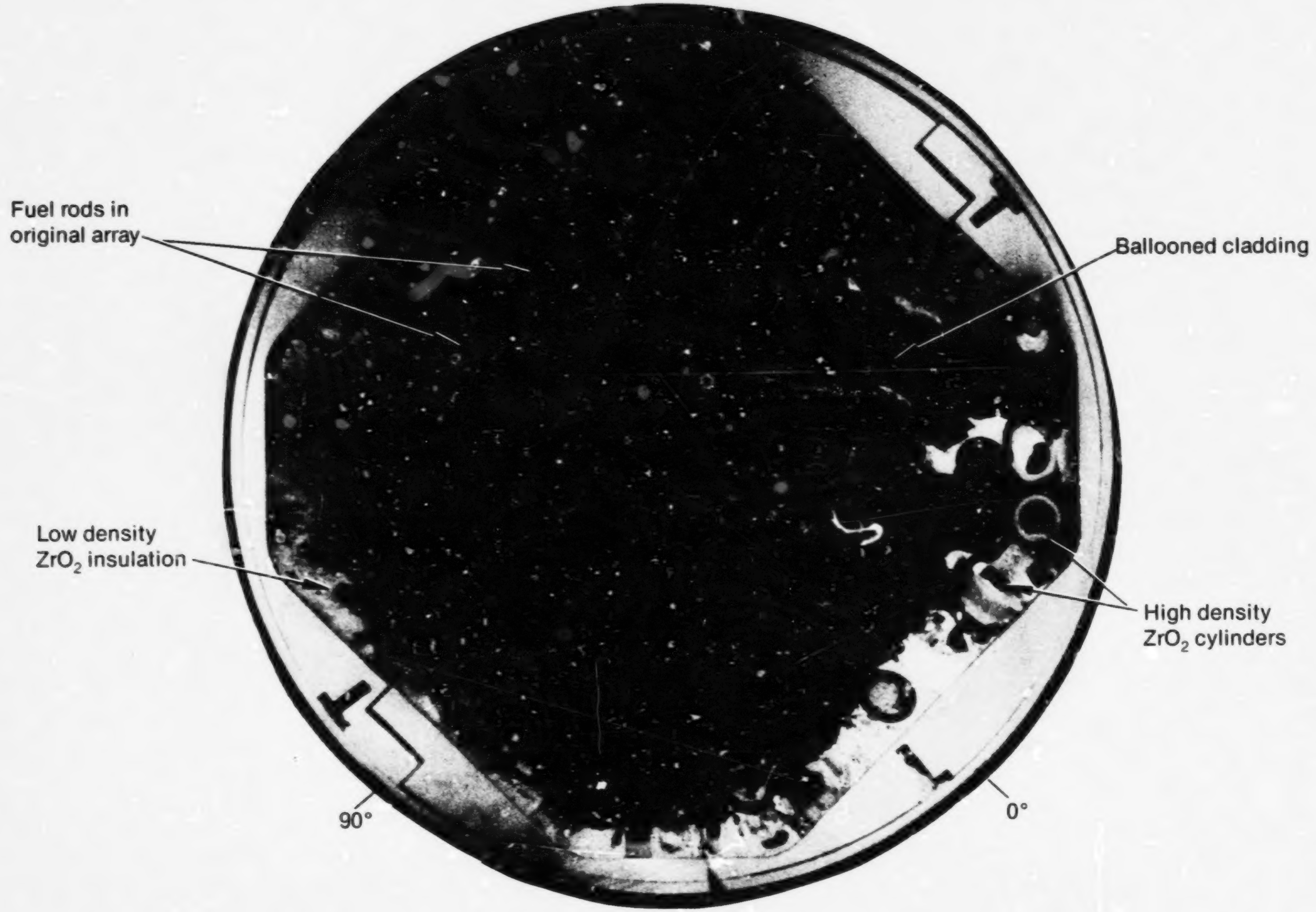
Fuel rods in original array
Ballooned cladding
Low density ZrO_2 insulation
High density ZrO_2 cylinders
90°
0°

Figure 11. Metallographic cross section of the SFD-ST bundle at 0.915 m above the bottom of the fuel stack.

BEST COPY AVAILABLE

RESULTS OF THE METALLOGRAPHIC EXAMINATIONS

The primary objective of the metallographic microstructural examinations of the SFD-ST fuel rod bundle cross sections was to describe in detail the physical and chemical state of the main components (fuel, cladding, spacer grids, zircaloy liner, insulation material, and saddle) and the reaction products which formed during the temperature transient. However, the present description could only be considered a preliminary qualitative assessment, since no chemical analyses were performed at that time.

Most of the nine cross sections were studied in the as-polished and etched condition under bright-field illumination at magnifications between 50 and 500X. In a few cases, additional information was obtained by using polarized light.

The following etching methods were applied to the specimens after they were inspected in the as-polished condition:

1. Attack polishing on the polishing wheel for about 5 min with a 1 wt% ammonium bifluoride [$(NH_4)_2F_2$] etching solution. Sometimes additional polishing without any etching was necessary to get a better microstructure before a second or third attack polishing was performed.
2. Ten-minute polishing by a vibratory polisher with a 0.3-μm diamond abrasive, followed by another 10-min polishing with 0.05-μm abrasive. During the last 5 min, attack polishing with a 7 vol% nitric acid (HNO_3) and 1 wt% $(NH_4)_2F_2$ etching solution was performed. [In some cases, a 7 vol% lactic acid and 7 wt% $(NH_4)_2F_2$ solution was used.]
3. Cotton swab etching with an 85 vol% hydrogen peroxide (H_2O_2), 15 vol% sulphuric acid (H_2SO_4) solution after vibratory polishing with 0.3 μm α-alumina.
4. Cotton swab etching with a 55 vol% lactic acid, 19 vol% water (H_2O), 19 vol% HNO_3, and 7 vol% hydrofluoric acid (HF) solution after polishing with a 0.5-μm diamond abrasive.

In the following, the phenomena that occurred during Test SFD-ST will be described with respect to increasing temperatures, which caused increasing degrees of chemical interaction between (a) cladding and steam; (b) solid cladding and solid UO_2; (c) molten cladding and solid UO_2 fuel; and (d) liquid or solidified metallic melts and steam. The chemical behavior of the spacer grids, inner zircaloy liner, ZrO_2 insulator materials, zircaloy saddle, and TCs will also be discussed. In the subsequent description of the microstructural appearance of the fuel rod bundle cross sections, the inspected location will be mainly characterized by the position of the fuel rods. Therefore, a simplified schematic of the SFD-ST fuel bundle cross section is given in Figure 12.

Metallographic Appearance of the Zircaloy Cladding

In the various fuel rod bundle cross sections, large temperature differences existed from rod to rod and also around the cladding circumference of the individual fuel rods. This can be recognized by the extent of zircaloy cladding oxidation and/or the zircaloy microstructure, and also by the formation of molten metallic or ceramic phases in some regions of the cross sections. Also, the steam flow rate during the course of the test was apparently not very uniform over the whole bundle cross section. The temperature differences and varying steam flow rate within the fuel bundle may be due to cladding and fuel relocation during the transient.

In general, large temperature differences around the circumference of the cladding were noticed for many of the fuel rods. One example is fuel Rod 1B at the 0.17-m cross-section elevation (Figure 5); a part of the cladding (≃25%) of this rod is missing. Figure 13 shows the typical microstructural appearance of small external cladding oxidation at the 0° orientation, resulting in the formation of a α-Zr(O) and a ZrO_2 layer. The thickness of the double layer is about 20 to 30 μm. On the cladding internal surface, apparently no UO_2/zircaloy interaction occurred. The microstructure of the remaining unreacted cladding tube is prior β-zircaloy. [On heatup, α-zircaloy transforms into β-zircaloy which decomposes into α'-zircaloy on cooldown.] That means the temperature of the cladding was above the $(\alpha + \beta)/\beta$ transformation temperature of about 1243 K for oxygen-free zircaloy. The $(\alpha + \beta)/\beta$ transformation temperature of the zircaloy increases with increasing oxygen content, and the transformation may be prevented in the oxygen concentration range between 20 and 30 at. %

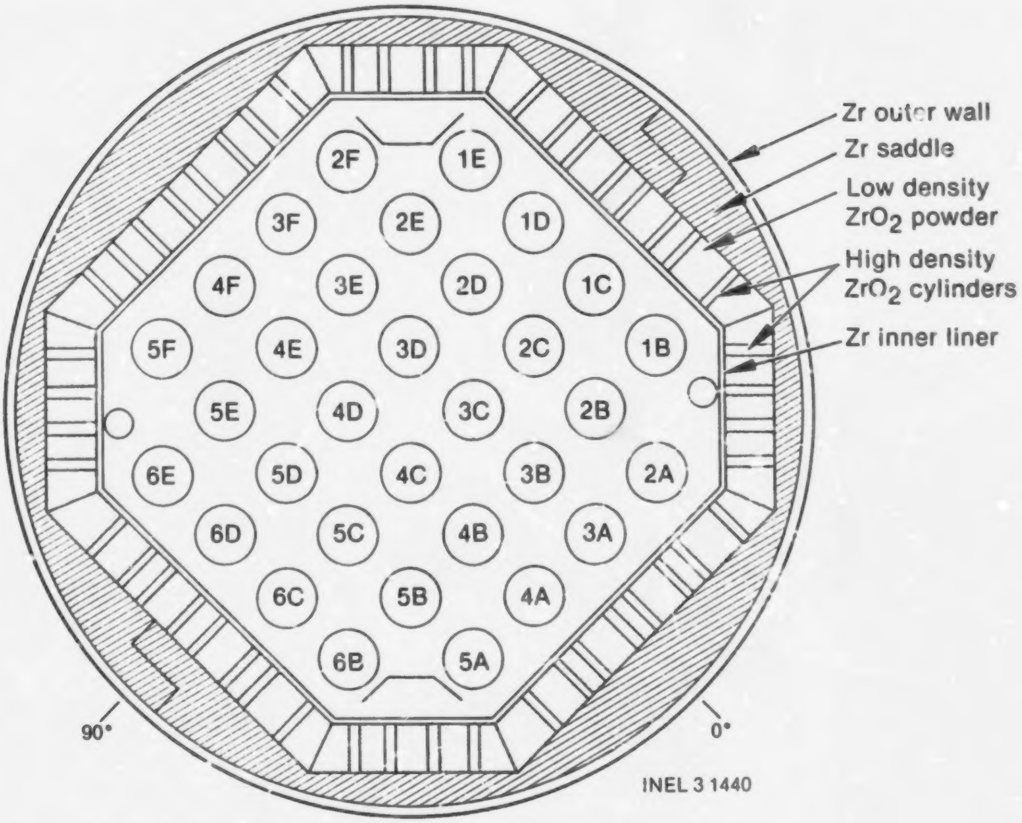
Zr outer wall
Zr saddle
Low density ZrO$_2$ powder
High density ZrO$_2$ cylinders
Zr inner liner
2F
1E
3F
2E
1D
4F
3E
2D
1C
5F
4E
3D
2C
1B
5E
4D
3C
2B
6E
5D
4C
3B
2A
6D
5C
4B
3A
6C
5B
4A
6B
5A
90°
0°
INEL 3 1440

Figure 12. Simplified schematic of the SFD-ST fuel bundle cross section.

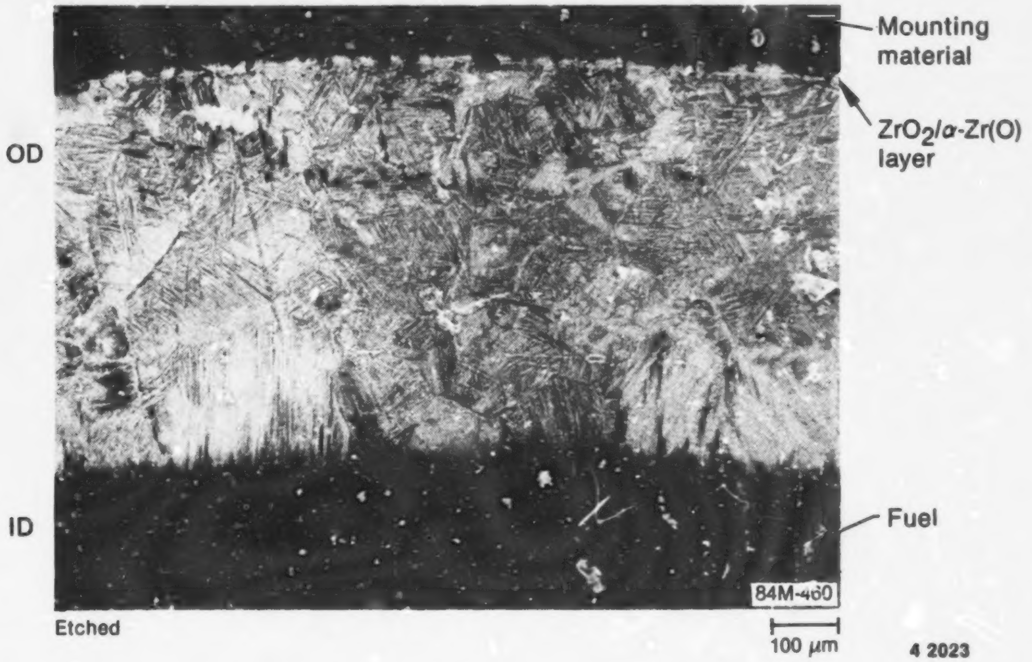
Mounting material
ZrO$_2$/α-Zr(O) layer
OD
ID
Fuel
84M-460
Etched
100 μm
4 2023

Figure 13. Weak external steam/cladding interactions (Rod 1B, 0°, at the 0.17-m cross-section elevation).

(Figure 14). The prior β-zircaloy forms very large grains, which are also partially visible in Figure 13.

The same fuel rod (1B) at the 180° orientation experienced higher temperatures, resulting in extensive external and internal cladding interaction (Figure 15). Prior β-zircaloy is no longer present, since the cladding was completely transformed to α-Zr(O) due to oxygen uptake from the steam on the outer diameter (OD) and from the fuel on the inner diameter (ID). The external ZrO_2 layer thickness varies between 120 and 140 μm.

The internal UO_2/zircaloy interaction resulted in the formation of the following reaction layer sequence which is similar to that of out-of-pile experiments:[1-3,6-8,12]

$$[UO_2 + Zr] \rightarrow [\alpha\text{-Zr(O)}_a + (U,Zr)] \rightarrow (U,Zr)\text{ alloy} \rightarrow \alpha\text{-Zr(O)}_b \rightarrow \beta\text{-Zr} \rightarrow \alpha\text{-Zr(O)} \rightarrow ZrO_2 .$$

The α-Zr(O)$_b$ and α-Zr(O)$_c$ layers grow both from the inside and outside into the cladding and are, at a smaller extent of oxidation, separated by prior β-zircaloy. In cases where they touch each other at the cladding center, the α-Zr(O)$_b$ and α-Zr(O)$_c$ phases can no longer be distinguished metallographically, since they have practically the same chemical composition and, therefore, the same microstructural appearance. The zircaloy alloying element tin is collected as metallic inclusions at the midpoint of the cladding (Figure 15).

The α-Zr(O)$_a$ and α-Zr(O)$_b$ layers form by diffusion of oxygen from the UO_2 into the zircaloy. The fuel is chemically dissolved by zircaloy to form metallic α-Zr(O) and elemental uranium. The metallic uranium does not remain at the UO_2/α-Zr(O)$_a$ interface, since it tends to interact with zirconium low in oxygen and therefore penetrates and/or diffuses into the cladding to form a metallic (U,Zr) alloy rich in uranium. The (U,Zr) alloy lies between two α-Zr(O) layers and is liquid above about 1423 K, depending on the zirconium content. The α-Zr(O)$_a$ layer adjacent to the fuel contains small amounts of the (U,Zr) alloy, primarily along grain boundaries but also as small globules within the α-Zr(O)$_a$ grains. The α-Zr(O)$_b$ layer adjacent to the β-zircaloy region contains no (U,Zr) alloy. During cooldown of the specimen, the hypostoichiometric UO_{2-x} decomposes into stoichiometric $UO_{2.00}$ and additional metallic uranium. The two-phase [α-Zr(O)$_a$ + (U, Zr)] layer is made up of relatively small, radially elongated α-Zr(O) grains compared to the α-Zr(O)$_b$ layer [and α-Zr(O) in general], which is made up of large grains (Figure 15).[2,3,6,12]

The boundary between the [α-Zr(O)$_a$ + (U,Zr)] and (U,Zr) layers is distinct, but the interface between the (U,Zr) and α-Zr(O)$_b$ layers can be very irregular. The formation of large (U,Zr) globules within the α-Zr(O)$_b$ layer occurs only at reaction temperatures $\geq$ 1773 K; at lower temperatures, small spherical particles form.[2,3] This means that this part of the cladding of fuel Rod 1B has reached temperatures of at least 1773 K, since large (U,Zr) globules (incursions) formed (Figure 15).

An intermediate cladding attack can be seen on the same fuel rod (1B) at a 270° orientation. The external [α-Zr(O)$_c$ + ZrO_2] double layer is about 65 μm thick. On the internal cladding surface, there is a solidified metallic melt that consists of molten cladding containing some dissolved fuel (Figure 16). This melt does not contain any appreciable amount of cladding from the 0.17-m elevation, since the full 600-μm thickness of cladding wall was present. A well defined interface exists between this "molten" region and the prior β-zircaloy phase region. This solidified metallic (U,Zr,O) melt is oxidized at its surface, indicating the presence of steam. In general, a ZrO_2 layer cannot form due to chemical interactions between the cladding and UO_2 fuel.[2,3] Figure 16 shows the formation of a (U,Zr,O) solid solution on the free surface of the solidified melt but not at the interface with UO_2 fuel. The prior β-zircaloy forms very large, well defined grains with a few α-Zr(O) incursions on the cladding OD. Similar localized cladding melting occurred at many other places within the fuel rod bundle with temperatures above 2033 K (the melting point of as-received zircaloy; for example, on Rod 2A at the same cross-section elevation (Figure 17). The slightly oxidized cladding (double layer 65 to 70 μm thick) was touched on the OD by a small melt droplet (about 100 μm diameter at this elevation). As a result of the higher temperatures at this location, a part of the α-Zr(O) was dissolved in the molten zircaloy. The solidified melt/prior β-zircaloy interface is well defined. The molten cladding area is only 400 μm wide and about 150 μm deep.

This type of melt droplet contact with solid cladding occurred at many places at the lowest (0.055-m) cross-section elevation of the bundle (Figure 3). Besides limited chemical interactions between the melt and the cladding, zircaloy grain growth and α-/β-zircaloy phase transformations took place, indicating that different maximum cladding temperatures were reached at these locations. Further examples are shown with increasing temperature in Figures 18 through 21.

Figure 18 shows a local melt/cladding contact that does not result in cladding melting but in grain

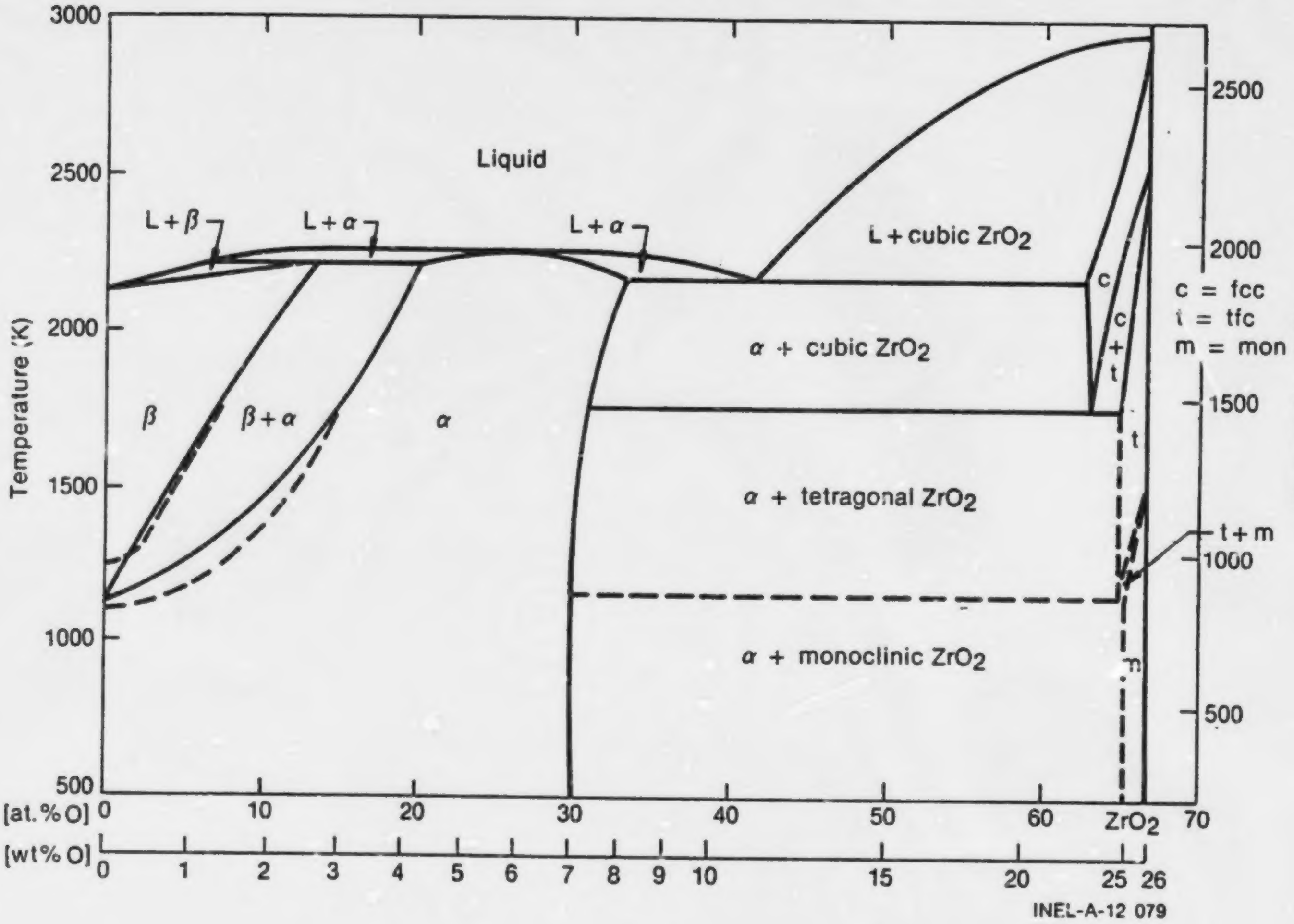

Figure 14. Zirconium-oxygen equilibrium phase diagram.

BEST COPY AVAILABLE

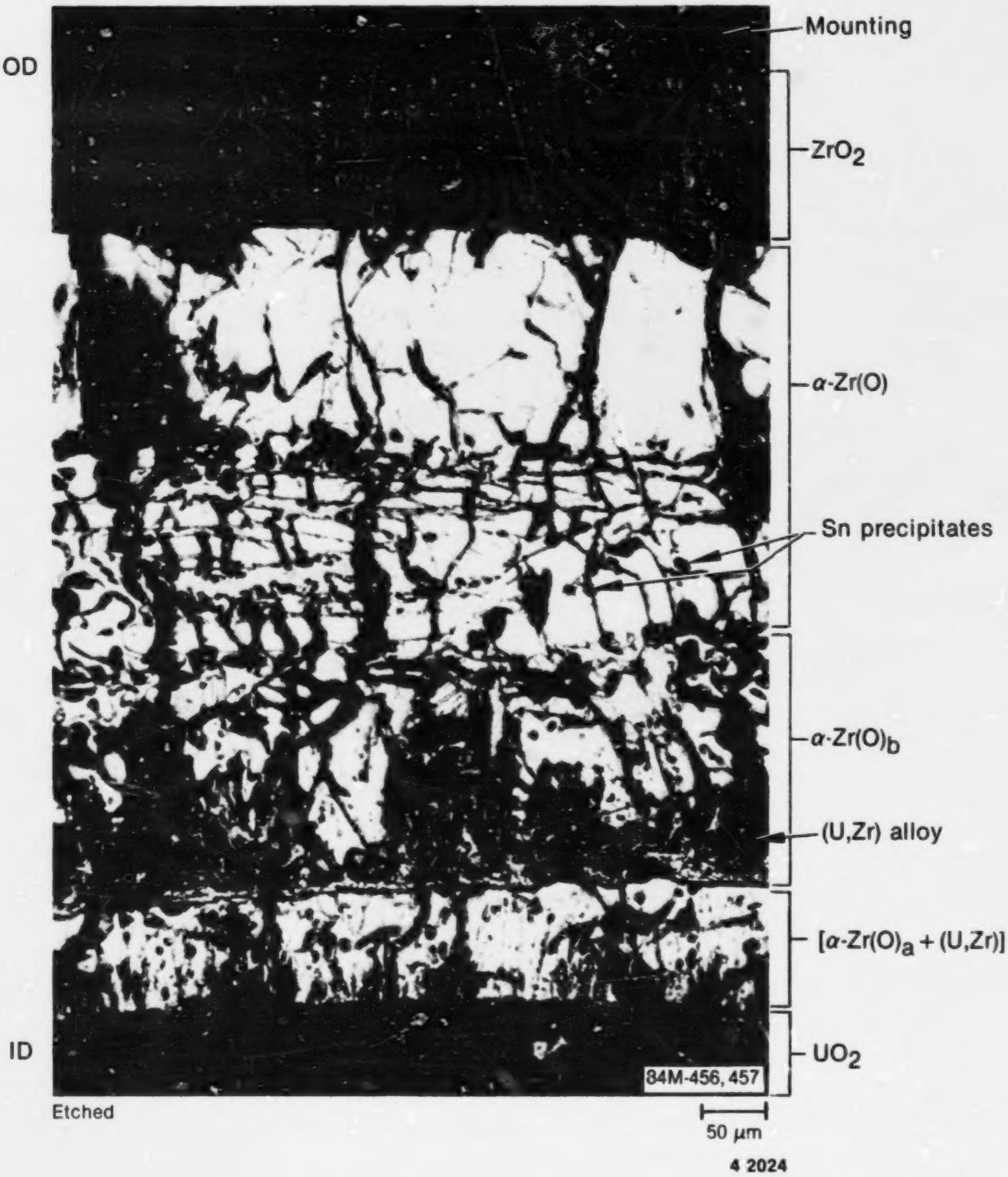
Mounting
OD
ZrO2
α-Zr(O)
Sn precipitates
α-Zr(O)b
(U,Zr) alloy
[α-Zr(O)a + (U,Zr)]
ID
UO2
84M-456, 457
Etched
50 μm
4 2024

Figure 15. Strong external and internal cladding interactions (Rod 1B, 180°, at the 0.17-m cross-section elevation).

BEST COPY AVAILABLE

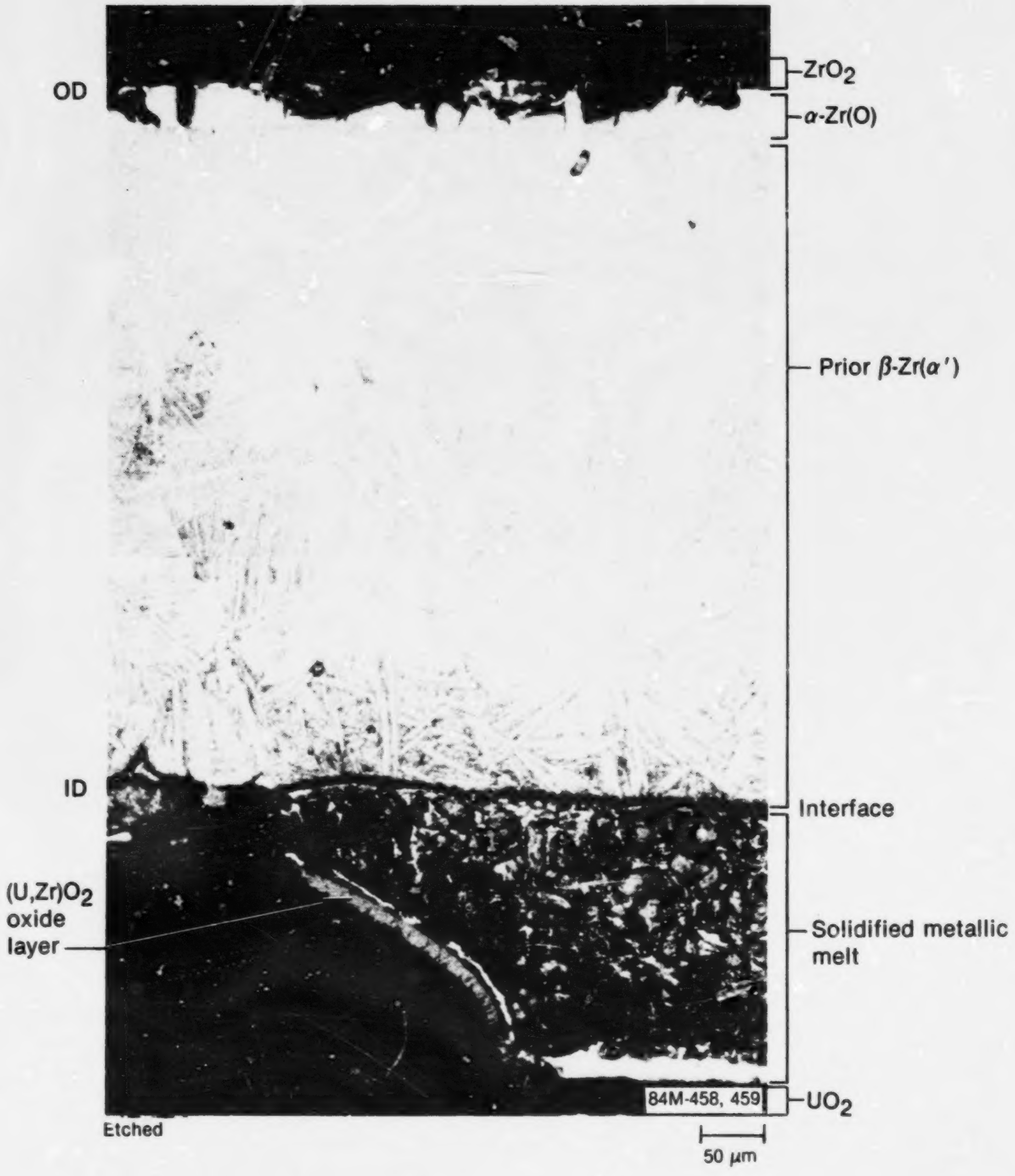
OD
ID
ZrO_2
α-Zr(O)
Prior β-Zr(α′)
Interface
Solidified metallic melt
$(U,Zr)O_2$ oxide layer
UO_2
84M-458, 459
Etched
50 μm
4 2025

Figure 16. External cladding oxidation and solidified metallic (U,Zr,O) melt between the UO_2 fuel and cladding (Rod 1B, 270°, at the 0.17-m cross-section elevation).

BEST COPY AVAILABLE

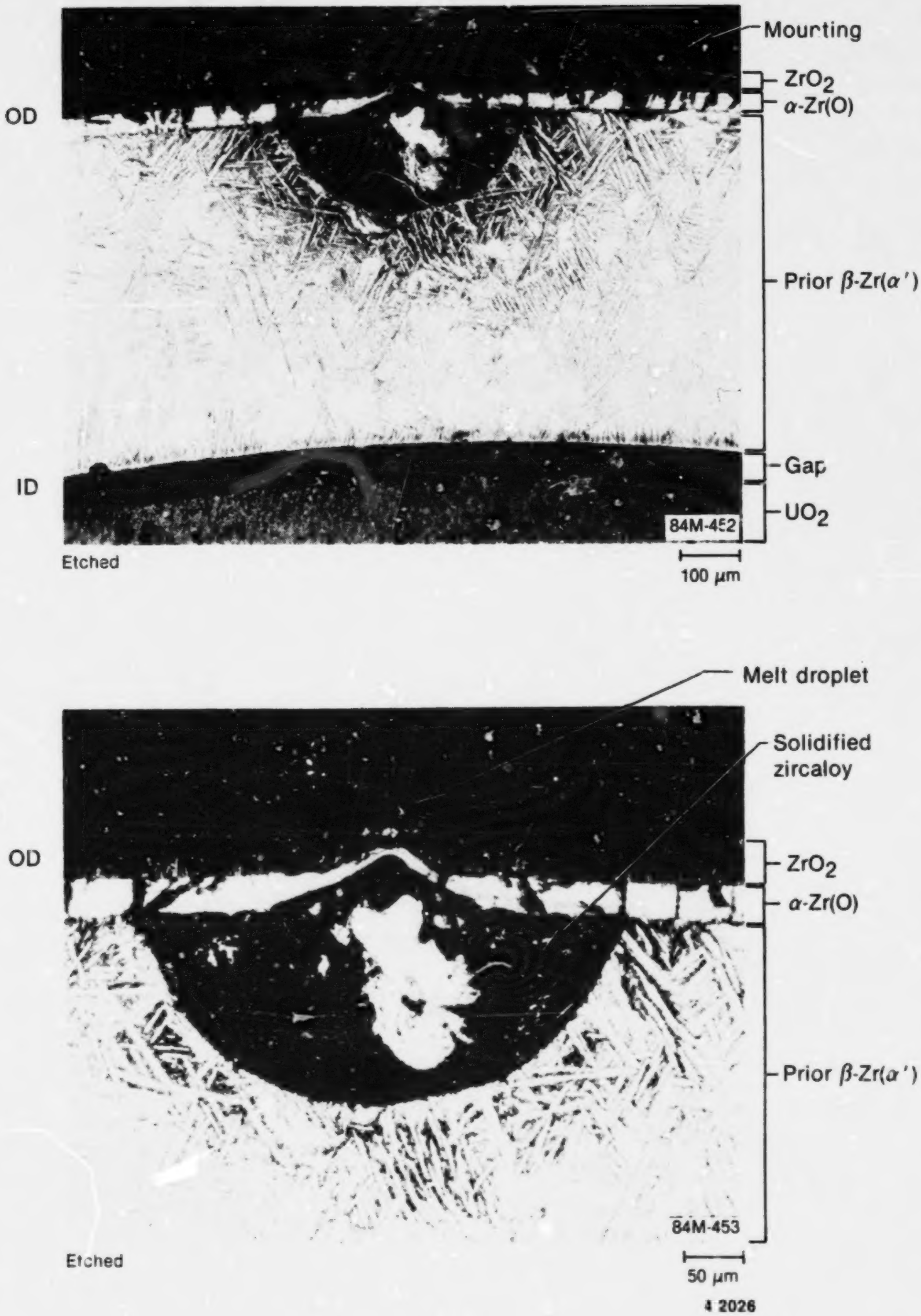
Mourting
ZrO2
α-Zr(O)
OD
Prior β-Zr(α')
Gap
ID
UO2
84M-452
Etched
100 μm
Melt droplet
Solidified zircaloy
OD
ZrO2
α-Zr(O)
Prior β-Zr(α')
84M-453
Etched
50 μm
4 2026

Figure 17. Localized cladding melting on the cladding external surface due to contact with a melt droplet (Rod 2A, 45°, at the 0.17-m cross-section elevation).

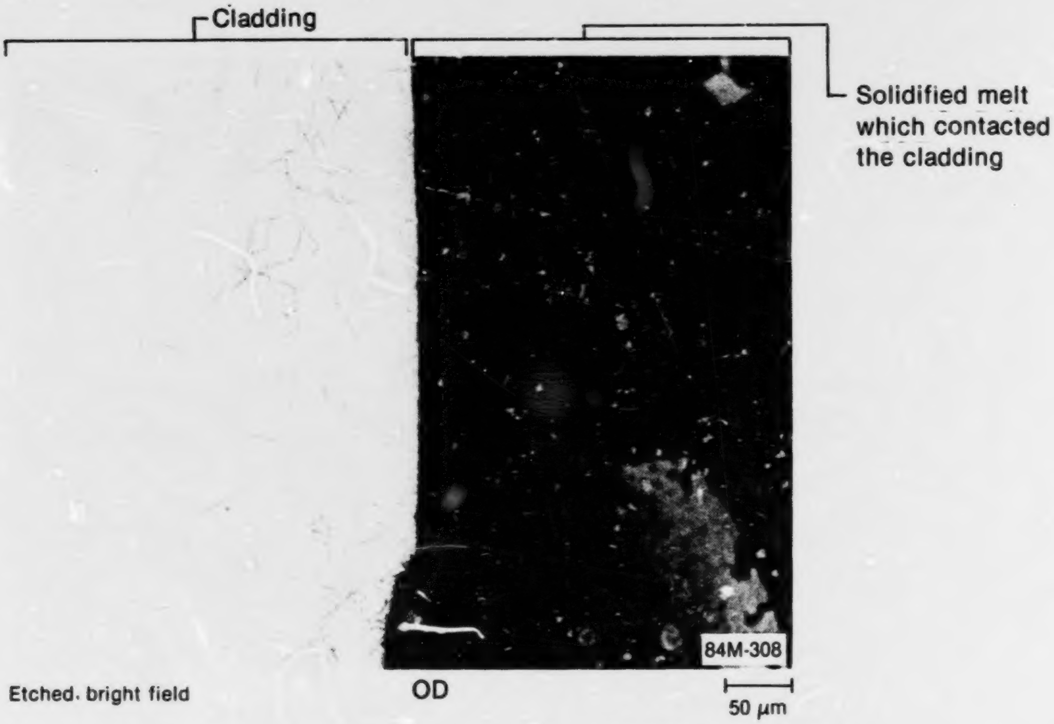
Cladding
Solidified melt which contacted the cladding
84M-308
OD
50 μm

Etched. bright field

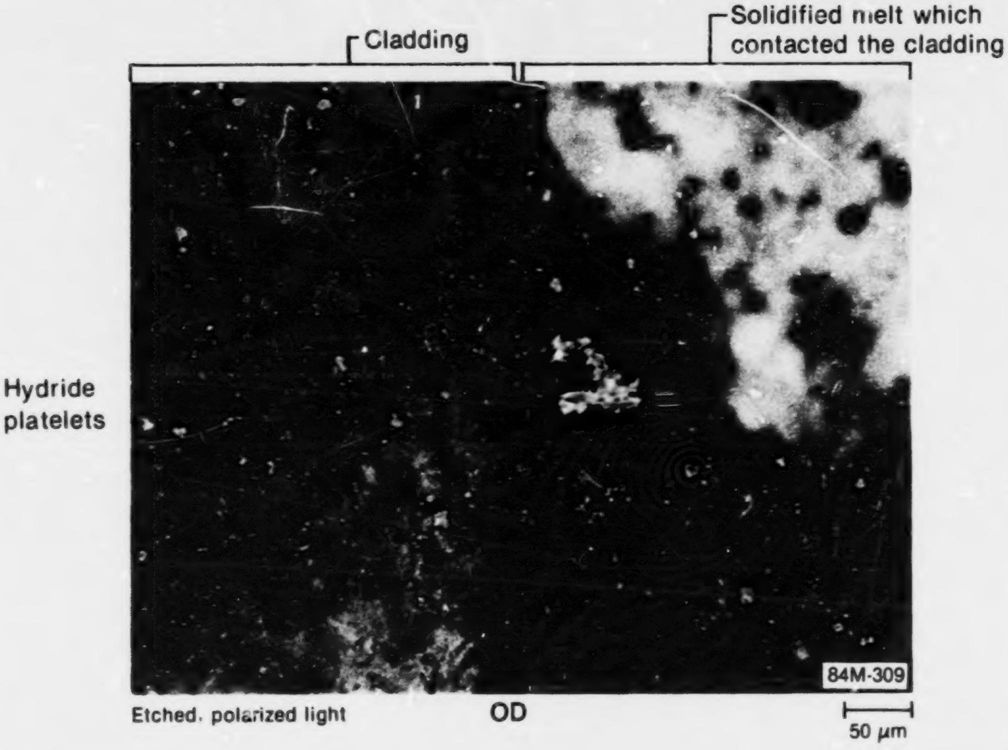
Cladding
Solidified melt which contacted the cladding
Hydride platelets
84M-309
OD
50 μm

Etched, polarized light

4 2027

Figure 18. Local melt/cladding contact that causes zircaloy grain structure changes (Rod 4D, 80°, at the 0.055-m cross-section elevation). Note the zirconium hydrides in the cladding.

BEST COPY AVAILABLE

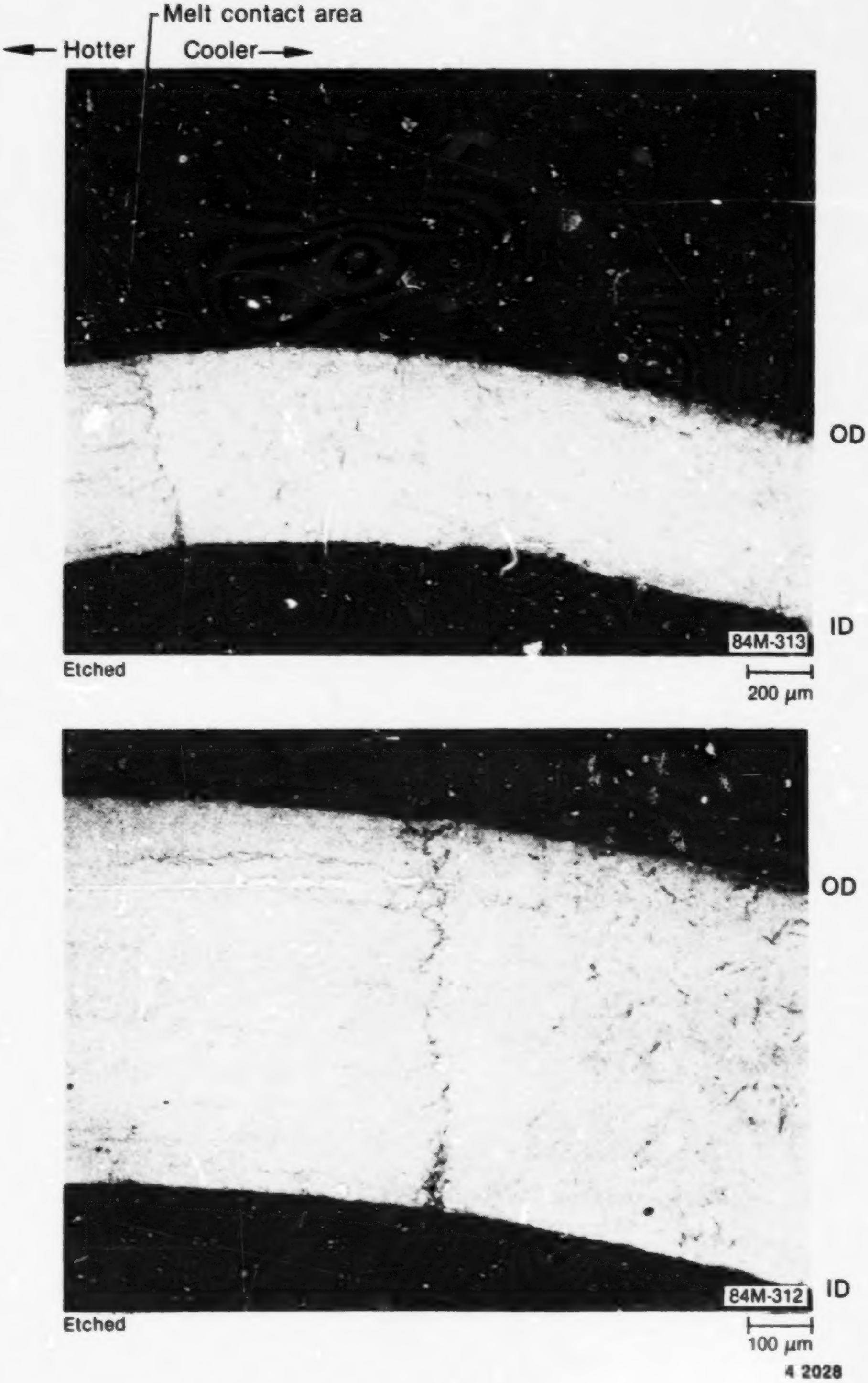
Melt contact area
Hotter
Cooler
OD
ID
84M-313
Etched
200 µm
OD
ID
84M-312
Etched
100 µm
4 2028

Figure 19. Local melt/cladding contact that causes large circumferential temperature differences within the cladding and different zirconium hydride precipitation behavior (Rod 2B, 270°, at the 0.055-m cross-section elevation).

BEST COPY AVAILABLE

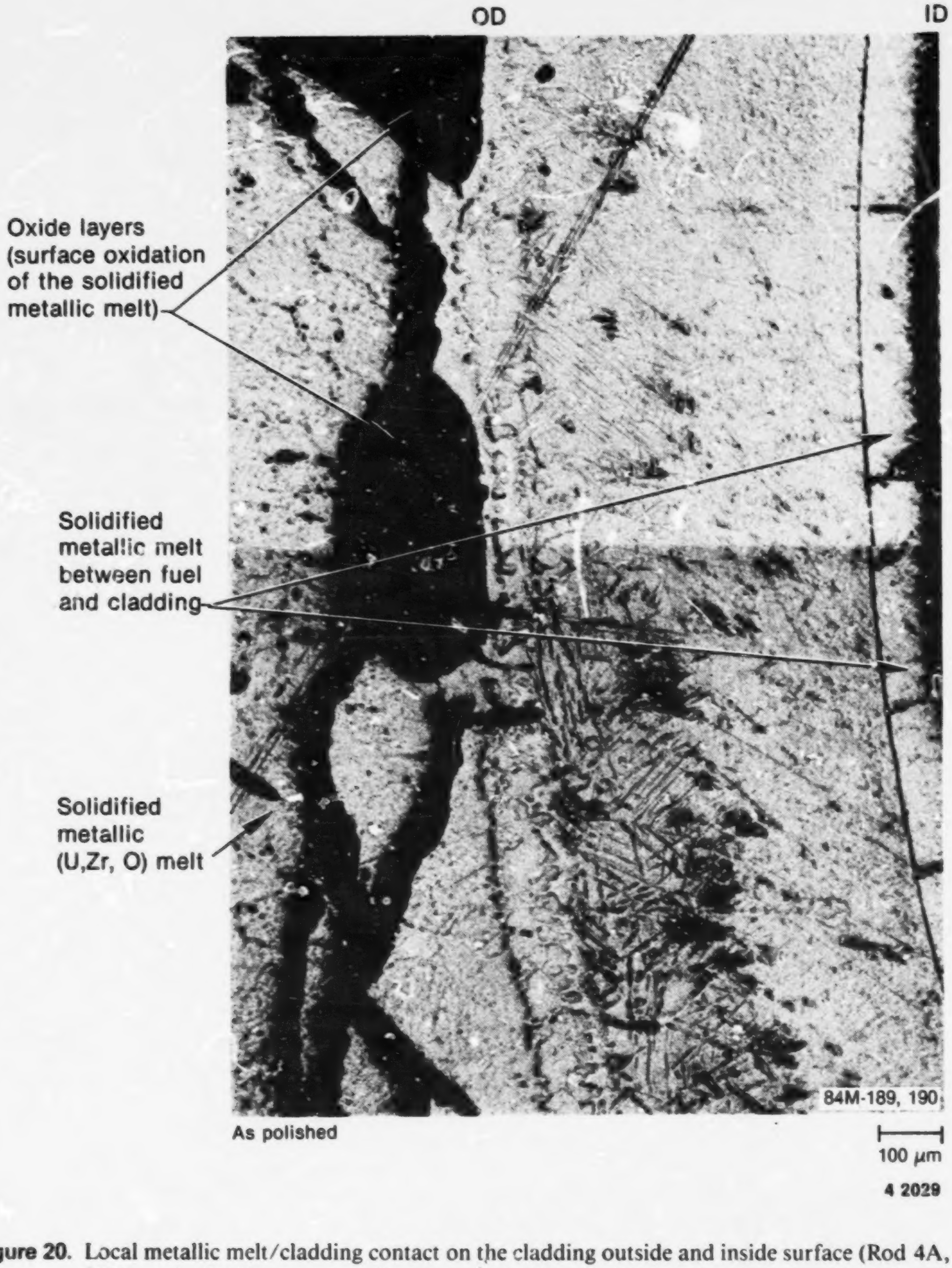
OD
ID
Oxide layers (surface oxidation of the solidified metallic melt)
Solidified metallic melt between fuel and cladding
Solidified metallic (U,Zr, O) melt
84M-189, 190
As polished
100 μm
4 2029

Figure 20. Local metallic melt/cladding contact on the cladding outside and inside surface (Rod 4A, 300°, at the 0.145-m cross-section elevation). Chemical interactions between the melt and cladding occur only on the cladding outside surface.

BEST COPY AVAILABLE

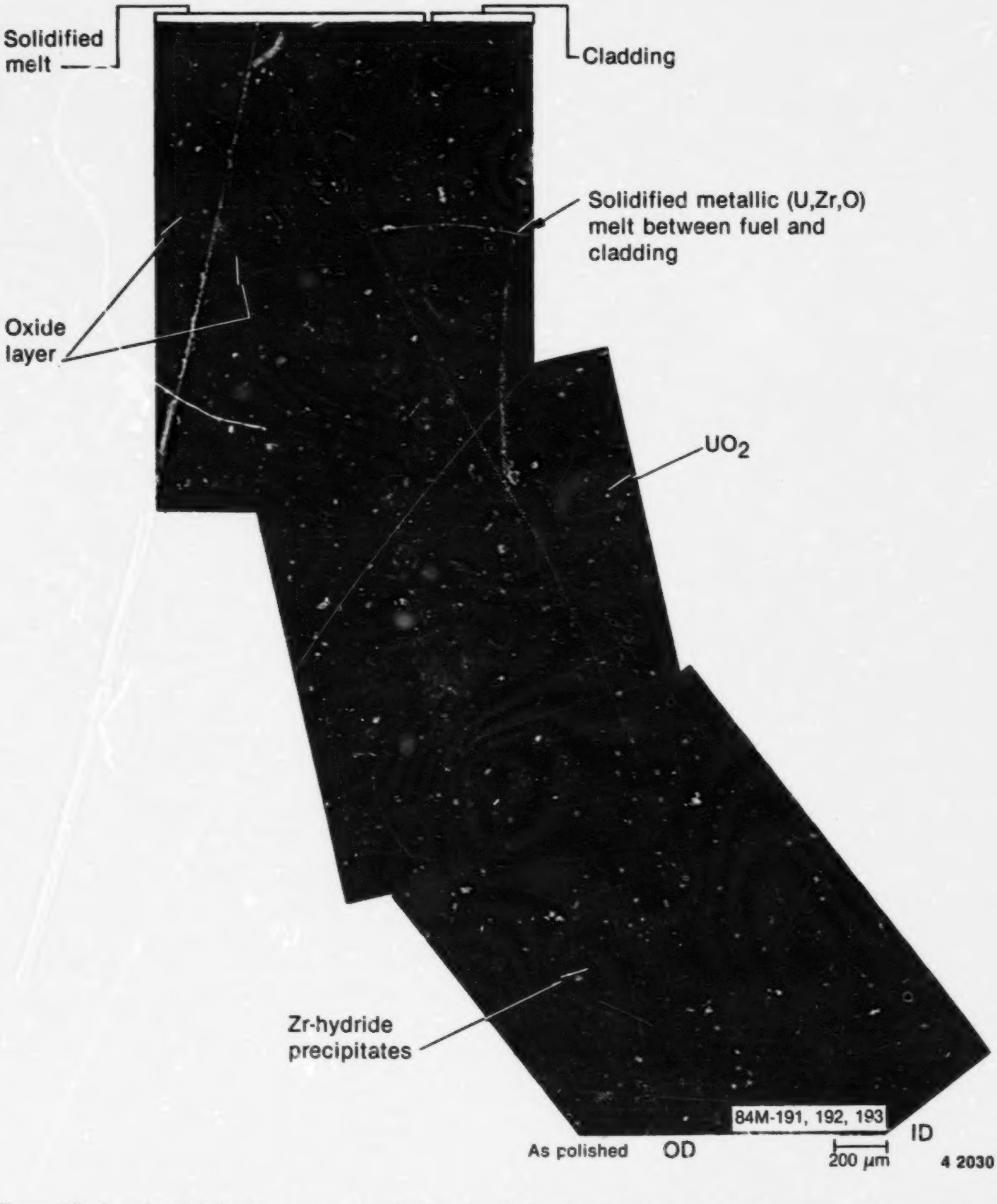
Solidified melt
Cladding
Solidified metallic (U,Zr,O) melt between fuel and cladding
Oxide layer
UO2
Zr-hydride precipitates
84M-191, 192, 193
ID
As polished
OD
200 μm
4 2030

Figure 21. Local melt/cladding contact on both sides of the cladding that causes azimuthal temperature differences in the cladding and different zirconium hydride precipitation behavior (Rod 4A, 300°, at the 0.145-m cross-section elevation).

BEST COPY AVAILABLE

growth and some α-/β-zircaloy phase transformation. Many zirconium hydride precipitates are visible in the cladding material. Figure 19 shows the microstructure of the cladding along the circumference. One can see that, due to the melt/cladding contact, temperature differences built up, resulting in different zirconium hydride precipitation behavior. There is a clear boundary between tangentially oriented and irregularly distributed zirconium hydride precipitates. Figure 20 shows a melt/cladding contact region in the cross section at the 0.145-m elevation. Melt interactions took place on both sides of the cladding, but the cladding apparently did not reach its melting point. Between the solidified melt and the OD cladding surface, a "cooling" channel formed which was oxidized by steam later in the transient, as was the surface of the metallic melt. The solidified melt layer on the cladding interior surface decreased to zero thickness at some locations on the cladding circumference (Figure 21). The cooler the cladding, the more zirconium hydride precipitates are visible.

The maximum thickness of the solidified melt layer on the cladding interior surface is shown in Figure 22. There is a crack in the melt layer, and zirconium hydrides in the prior β-zircaloy phase are visible. The external cladding oxidation is very small. Repolishing and reexamination of the cross section revealed that the solidified melt consists of two or three different phases and has a eutectic metallographic appearance (Figure 23). This melt must have been formed at higher elevations and flowed down in the fuel/cladding gap. Very little of the cladding at this elevation melted, since the full 600-μm cladding wall thickness is present as unmelted cladding. Similar melt formations have also been observed in other fuel rods. Figure 24 shows a solidified melt between the fuel and cladding which has a different metallographic appearance than that of Figure 23. The chemical composition of these melts has not been determined.

Another good example of strong circumferential temperature gradients as revealed by cladding interactions is Rod 3A (270°) at the 0.17-m cross-section elevation. The greatest part of the cladding and fuel of Rod 3A had disappeared (Figure 5). At the hottest side (Figure 25), the (U,Zr) alloy, which formed due to chemical interactions between the cladding and fuel, formed large globules in the α-Zr(O). The central part of the cladding is completely transformed into α-Zr(O). At the cooler side of the cladding (<1773 K), prior β-zircaloy [with α-Zr(O) incursions] is still visible (Figure 26). The (U,Zr) alloy forms a homogeneous layer between the [α-Zr(O)$_a$ + (U,Zr)] and α-Zr(O)$_b$ with regular interfaces. It is important to point out that the (U,Zr) alloy is metallic, and its microstructure looks similar to that of α-Zr(O).[2,3] For this reason, it is very difficult to recognize the (U,Zr) alloy in the as-polished condition. In the etched condition, the (U,Zr) alloy oxidizes on its surface to (U,Zr)O_2 and can be distinguished from the other phases.

In the upper fuel rod bundle regions, especially at the 0.915-m cross-section elevation (Figure 11), cladding deformation (ballooning) took place before the zircaloy was completely oxidized. Figure 27 shows the microstructure of fully oxidized zircaloy tubing. A ceramic solidified melt is in contact with the oxidized cladding at the external surface. Also, apparently a part of the internal cladding was molten and dissolved some fuel before it was oxidized. Two observations support this hypothesis: (a) the porosity of the interaction layer between the oxidized cladding and fuel and (b) the appearance of a phase in a crack of the UO_2 fuel which looks very similar (Figure 28). As subsequent analysis will show, the external and internal melts were metallic before they were oxidized in the course of the transient. The oxidized cladding (ZrO_2) forms very long columnar grains. Also, the solidified melt and the oxidized cladding appear to be single-phase at higher magnifications.

Metallographic Appearance of the Solidified Melts

General Considerations. With increasing temperatures, some of the phases or reaction products will melt and relocate within the fuel rod bundle. Due to this relocation, parts of the bundle will be blocked to different degrees, as can be seen in the various cross sections (Figures 4 through 7). As long as the cladding is not fully oxidized, the metallic parts will melt first at about 2033 K, the melting point of as-received (oxygen-deficient) zircaloy-4. The melting point of zircaloy increases with increasing oxygen content up to about 2243 K, the melting point of oxygen-saturated α-Zr(O). Much higher temperatures are necessary to obtain ceramic melts. The melting point of ZrO_2 is 2963 K, and that of stoichiometric UO_2 is 3123 K. The lower melting points of Inconel 718, the Inconel oxidation products, and alumina (2323 K) are not considered, since they are present in the bundle only in small amounts. Also, the low-temperature eutectics which may form between Inconel and zircaloy are probably not of great importance. However, the formation of reaction products which have lower melting points than

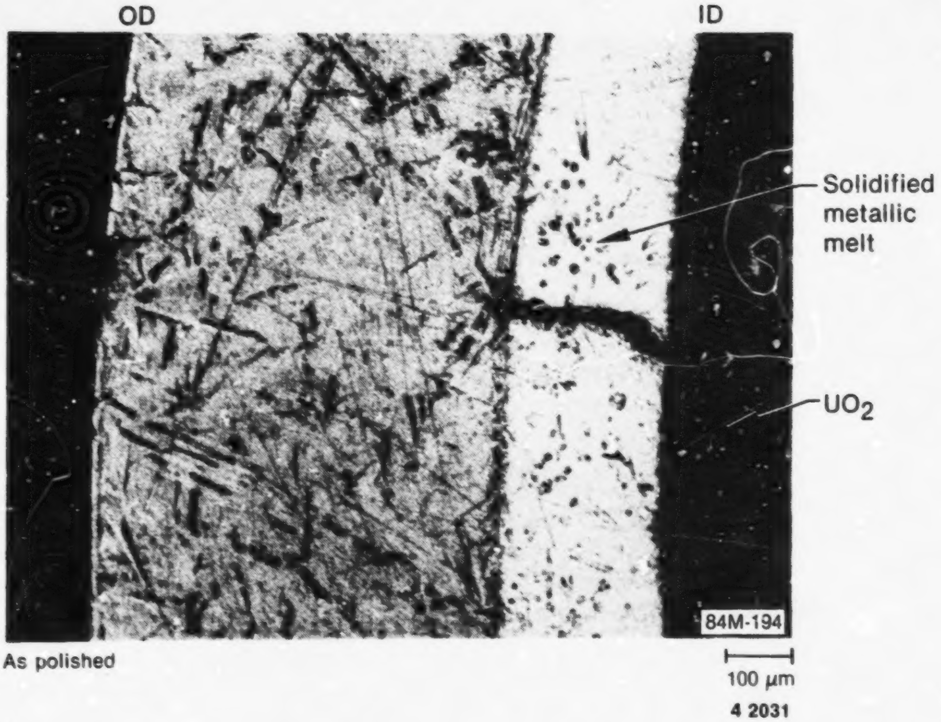
OD
ID
Solidified metallic melt
UO$_2$
84M-194
As polished
100 μm
4 2031

Figure 22. Location of the maximum solidified melt layer on the internal cladding surface (Rod 4A, 300°, at the 0.145-m cross-section elevation). Note the zirconium hydride formation in the cladding.

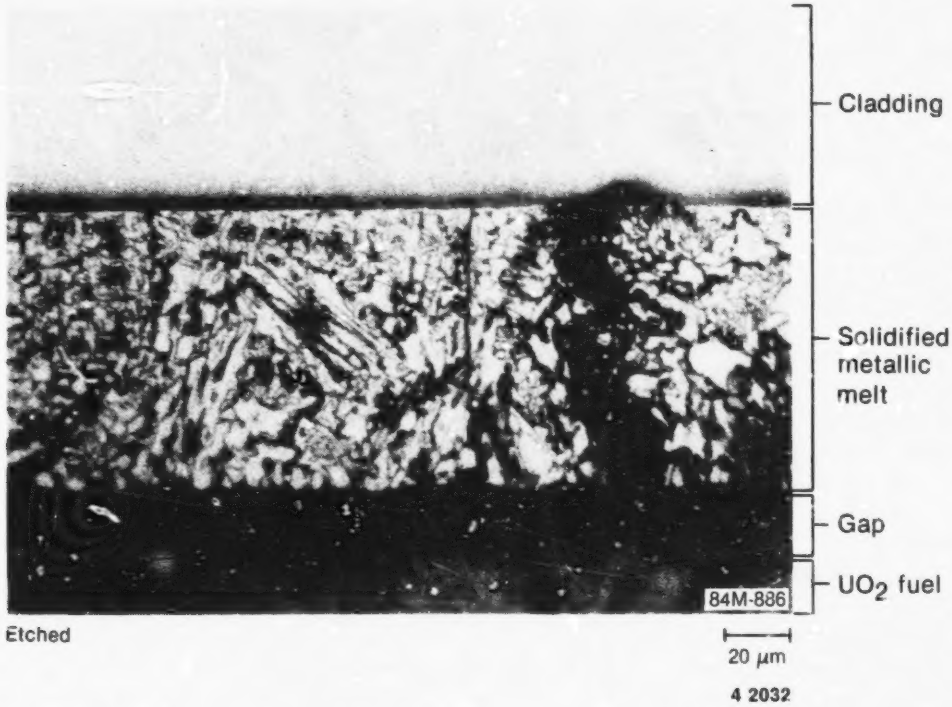
Cladding
Solidified metallic melt
Gap
UO$_2$ fuel
84M-886
Etched
20 μm
4 2032

Figure 23. Solidified melt between fuel and cladding (Rod 4A, 300°, at the 0.145-m cross-section elevation).

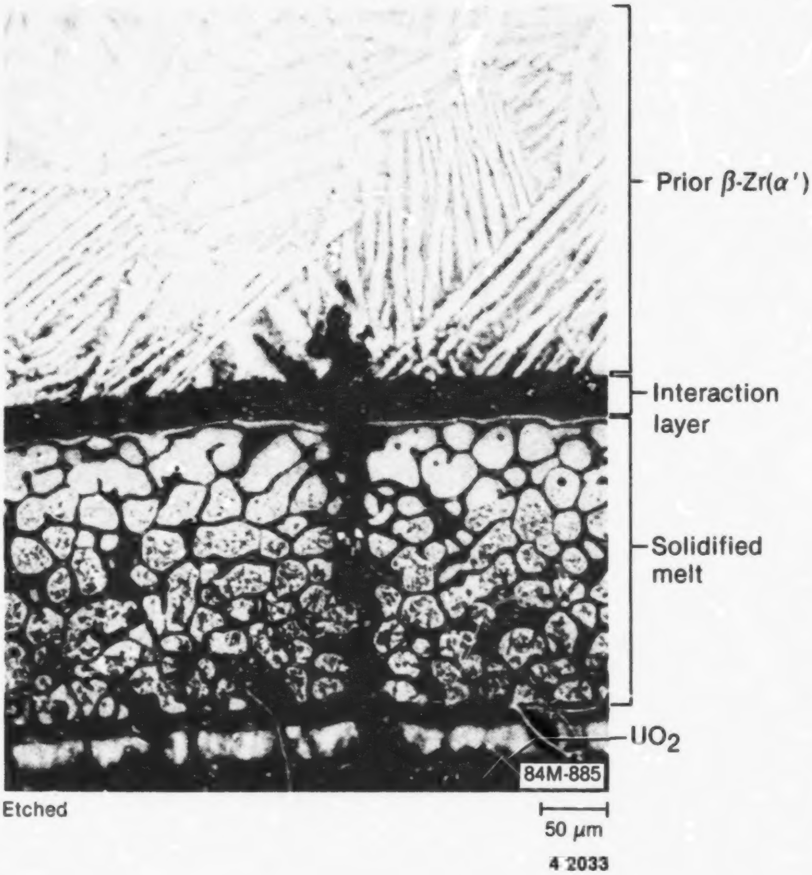
Prior β-Zr(α')
Interaction layer
Solidified melt
UO2
84M-885
Etched
50 μm
4 2033

Figure 24. Solidified melt between fuel and cladding (Rod 6B, at the 0.145-m cross-section elevation).

BEST COPY AVAILABLE

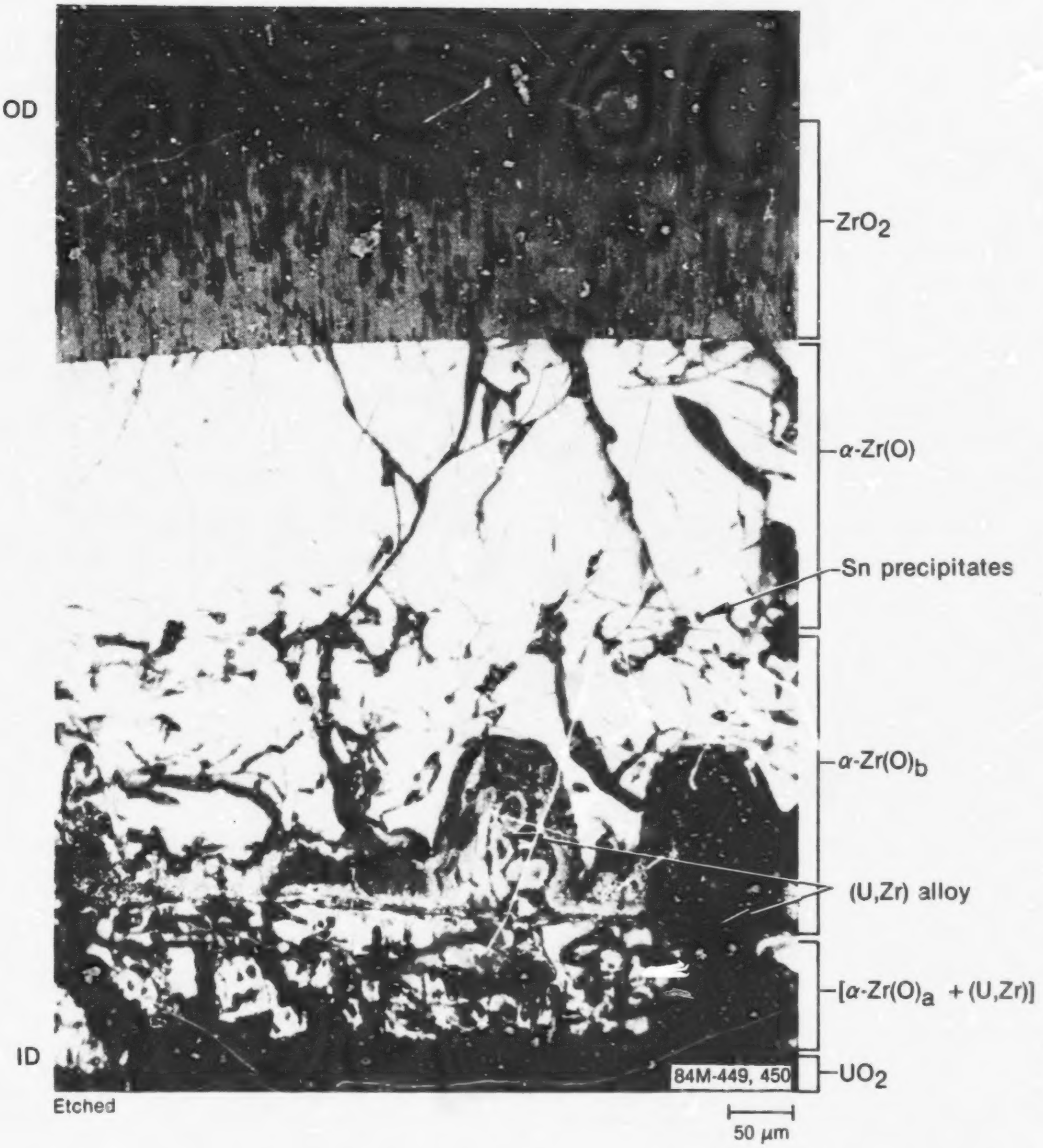
OD
ZrO$_2$
α-Zr(O)
Sn precipitates
α-Zr(O)$_b$
(U,Zr) alloy
[α-Zr(O)$_a$ + (U,Zr)]
ID
UO$_2$
84M-449, 450
Etched
50 μm

4 2034

Figure 25. Strong external steam/zircaloy and internal UO_2/zircaloy cladding interactions (Rod 3A, 0°, at the 0.17-m cross-section elevation). Note the (U,Zr) alloy incursions into the α-Zr(O) phase.

BEST COPY AVAILABLE

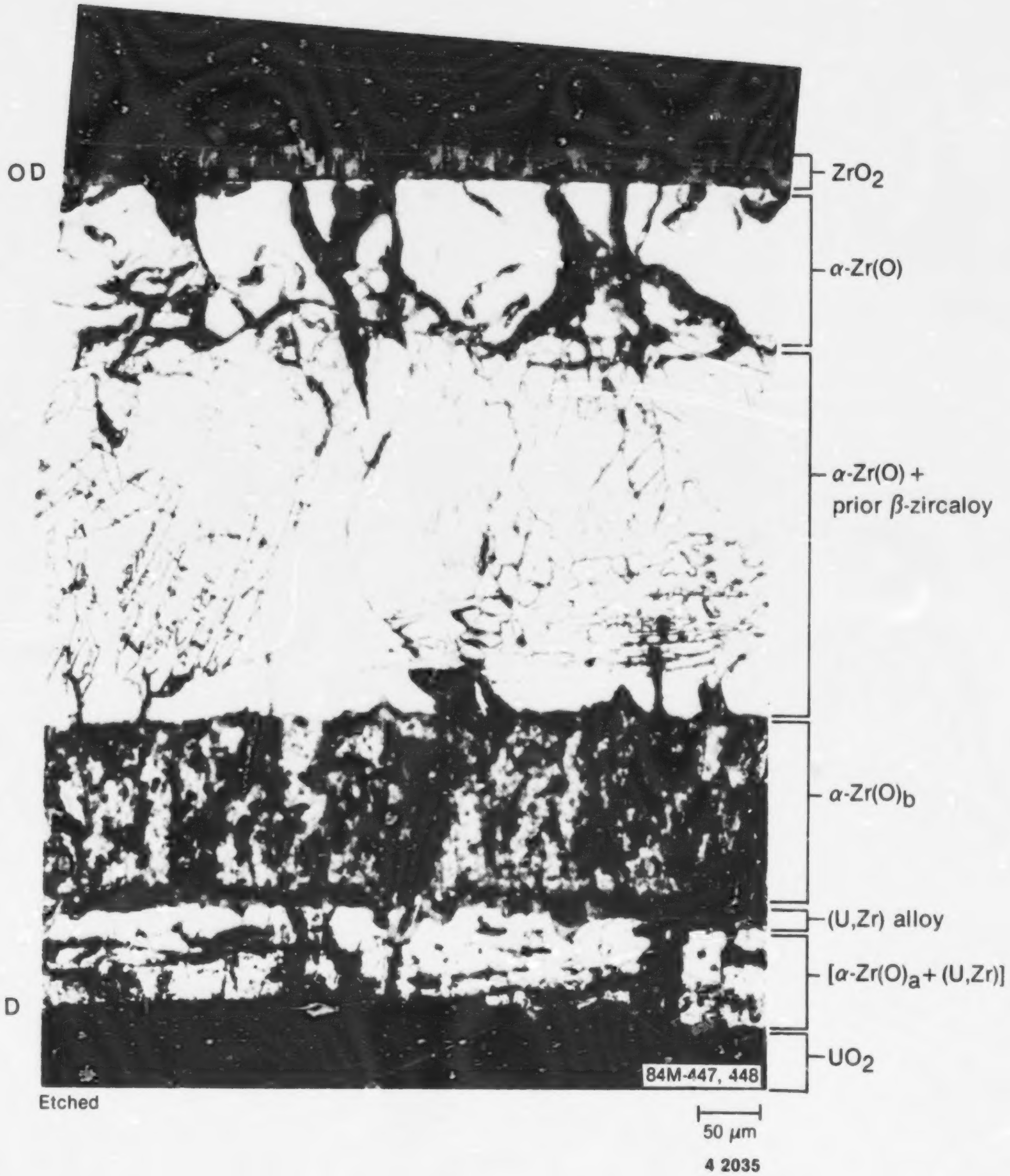
OD
ZrO_2
α-Zr(O)
α-Zr(O) +
prior β-zircaloy
α-Zr(O)$_b$
(U,Zr) alloy
[α-Zr(O)$_a$ + (U,Zr)]
ID
UO_2
84M-447, 448
Etched
50 μm
4 2035

Figure 26 External steam/zircaloy and internal UO_2/zircaloy cladding interactions (Rod 3A, 270°, at the 0.17-m cross-section elevation). The (U,Zr) alloy is sandwiched by two α-Zr(O) layers.

BEST COPY AVAILABLE

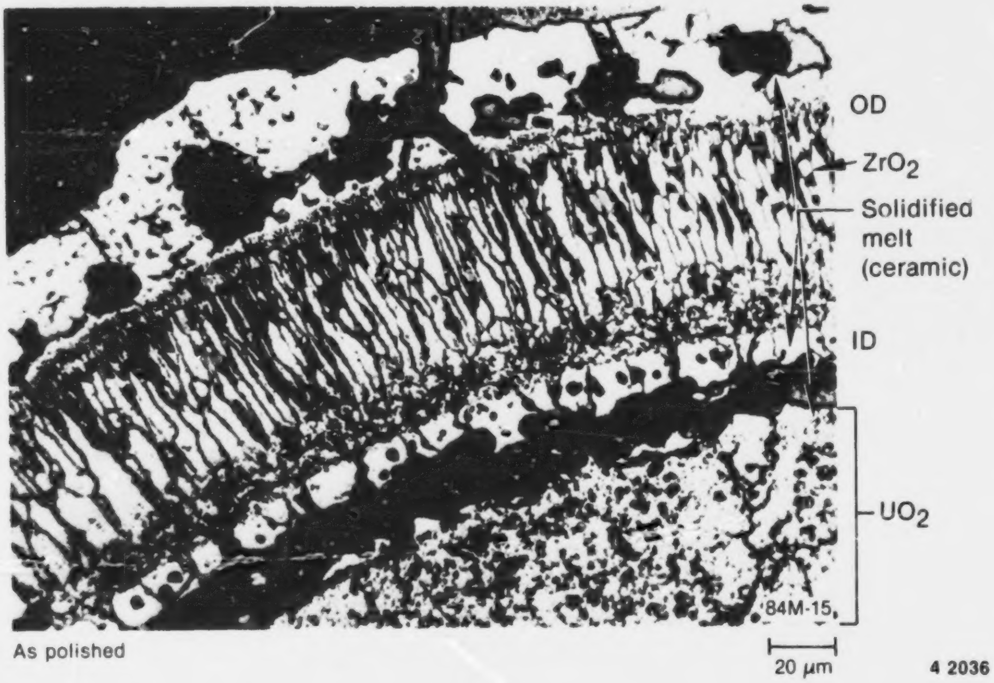
OD
ZrO_2
Solidified melt (ceramic)
ID
UO_2
84M-15
As polished
20 μm
4 2036

Figure 27. Completely oxidized cladding in contact with a ceramic melt which was initially metallic. Apparently a part of the internal cladding was molten before it was oxidized (Rod 2C, 90°, at the 0.915-m cross-section elevation).

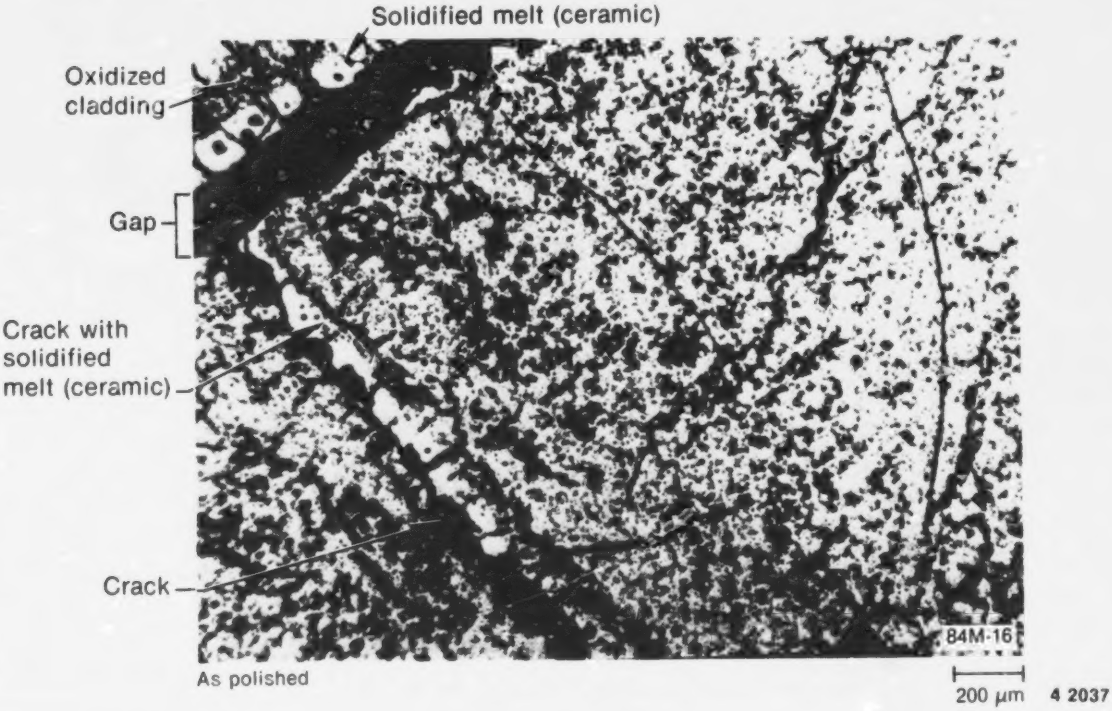
Solidified melt (ceramic)
Oxidized cladding
Gap
Crack with solidified melt (ceramic)
Crack
84M-16
As polished
200 μm
4 2037

Figure 28. Cladding/fuel interface. The crack in the UO_2 is partially filled with a ceramic melt which was probably metallic when it penetrated into the crack (Rod 2C, 90°, at the 0.915-m cross-section elevation).

the components should be taken into consideration. UO_2 and ZrO_2 form a solid solution at higher temperature, with a melting point of about 2873 K at a 50/50 mol% composition. Between UO_2 and oxygen-saturated α-Zr(O), a eutectic interaction takes place at about 2173 K (20 mol% UO_2) and a monotectic interaction at about 2673 K (85 mol% UO_2).[2] It is important to emphasize that UO_2 fuel can be liquefied by molten zircaloy at temperatures below 2273 K.[1] For this reason, a rather large temperature range exists (2033 to 3123 K) in which various molten materials may form.

Nearly all the fuel rod bundle cross sections reveal that metallic melts formed in the course of the temperature transient which flowed down the fuel pellet stack, outside and/or inside the partially oxidized cladding, and also penetrated cracks in the UO_2 pellets. These metallic melts interacted chemically with the steam, fuel, and/or ZrO_2, resulting in not only a continuous change of their chemical composition but also a change of their melting points. As a result of these interactions, or due to temperature decreases, the melts solidified. In many cases, the solidified melts were initially metallic but were oxidized later in time by steam. For this reason, it is sometimes very difficult to determine if the melts were ceramic during the whole test or if the formerly metallic melts were oxidized later in the transient.

The metallic melts probably consisted of a (U,Zr,O) mixture, which can be either homogeneous or heterogeneous at temperature, depending on the oxygen content, i.e., the amount of dissolved UO_2 and/or ZrO_2. The homogeneous metallic (U,Zr,O) melt decomposes during cooling into two metallic phases, an α-Zr(O) phase containing some uranium and a (U,Zr) alloy containing little or no oxygen.[1,7,9] Above a certain oxygen content in the melt (about 3.6 wt% oxygen), solid $(U,Zr)O_{2-x}$ particles with a low zirconium content precipitate at temperature to form a liquid/solid phase mixture. The solid substoichiometric $(U,Zr)O_{2-x}$ particles decompose on cooling into stoichiometric $(U,Zr)O_2$ and a (U,Zr) alloy (Figure 14).[1,7] In some cases, a portion of the $(U,Zr)O_2$ phase may exhibit a dendritic (tree-like) structure, indicating that it formed during cooling. The actual amount of ceramic phase at test temperatures was therefore smaller.

With respect to the dissolution of solid UO_2 by molten zircaloy, up to 35 wt% UO_2 can be dissolved before a ceramic phase is evident at room temperature.[1] The amount of ZrO_2 which can be dissolved before a ceramic phase can be recognized at room temperature is between 25 and 30 wt%. In the case of ZrO_2 dissolved in molten zircaloy, no decomposition of the homogeneous metallic (Zr,O) melt occurs during cooldown. At room temperature, only oxygen-stabilized α-Zr(O) is present.

The number of phases of solidified metallic melts and their chemical composition, with and without ceramic precipitates, tells what could have happened at temperature, since the observed phases should be in agreement with the (U,Zr,O) ternary phase diagram. The ternary equilibrium phase diagrams of the (U,Zr,O) system at 1273 and 2273 K are shown in Figure 29.[2,8] At 2273 K, one can recognize the large region of the homogeneous melt (U,Zr,O) on the lower right and the large region of the heterogeneous melt [(U,Zr,O) plus the solid $(U,Zr)O_{2-x}$ particles] on the upper left. The equilibrium phases expected during cooldown and at room temperature are shown in the phase diagram at 1273 K. (No further decompositions take place at lower temperatures.) Melting experiments with (UO_2 + Zr) or (UO_2 + Zr + ZrO_2) mixtures always result, independent of the cooldown rate, in the equilibrium phases shown in Figure 29.[1]

The initial tie-line for the UO_2 fuel/zircaloy cladding interaction lies between UO_2 at point A and zirconium at point B. As the reaction proceeds, the cladding picks up oxygen from the fuel; and point B moves continuously from oxygen-poor zirconium toward oxygen-saturated α-Zr(O), point C. Oxygen-stabilized α-Zr(O) contains a maximum of about 30 at. % oxygen, as shown in Figure 14. Point A moved relatively little (toward UO_{2-x}), since the amount of UO_2 fuel in the experiments was always much larger than the amount of zircaloy cladding. As a result of UO_2/zircaloy interactions alone, point C cannot be reached; the reaction products should be on the tie-line A-B. If oxygen-saturated α-Zr(O) is in contact with UO_2, no pronounced chemical interactions will take place under solid-state conditions. When this equilibrium position has been reached, the quasi-binary α-Zr(O)-UO_2 phase diagram is applicable (Figure 30).[13] One has to point out that this quasi-binary phase diagram can only be applied for oxygen-saturated α-Zr(O), not for zircaloy with a much smaller oxygen content.[2] If one exceeds point C, ZrO_2 forms at higher oxygen concentrations.

In the large triangle on the lower right of the (U-Zr-O) phase diagram for 1273 K, the final phases are α-Zr(O) and a (U,Zr) alloy (Figure 29). In the large triangle in the center of the diagram, the final phases are α-Zr(O), a (U,Zr) alloy, and UO_2. No additional decomposition takes place on cooldown

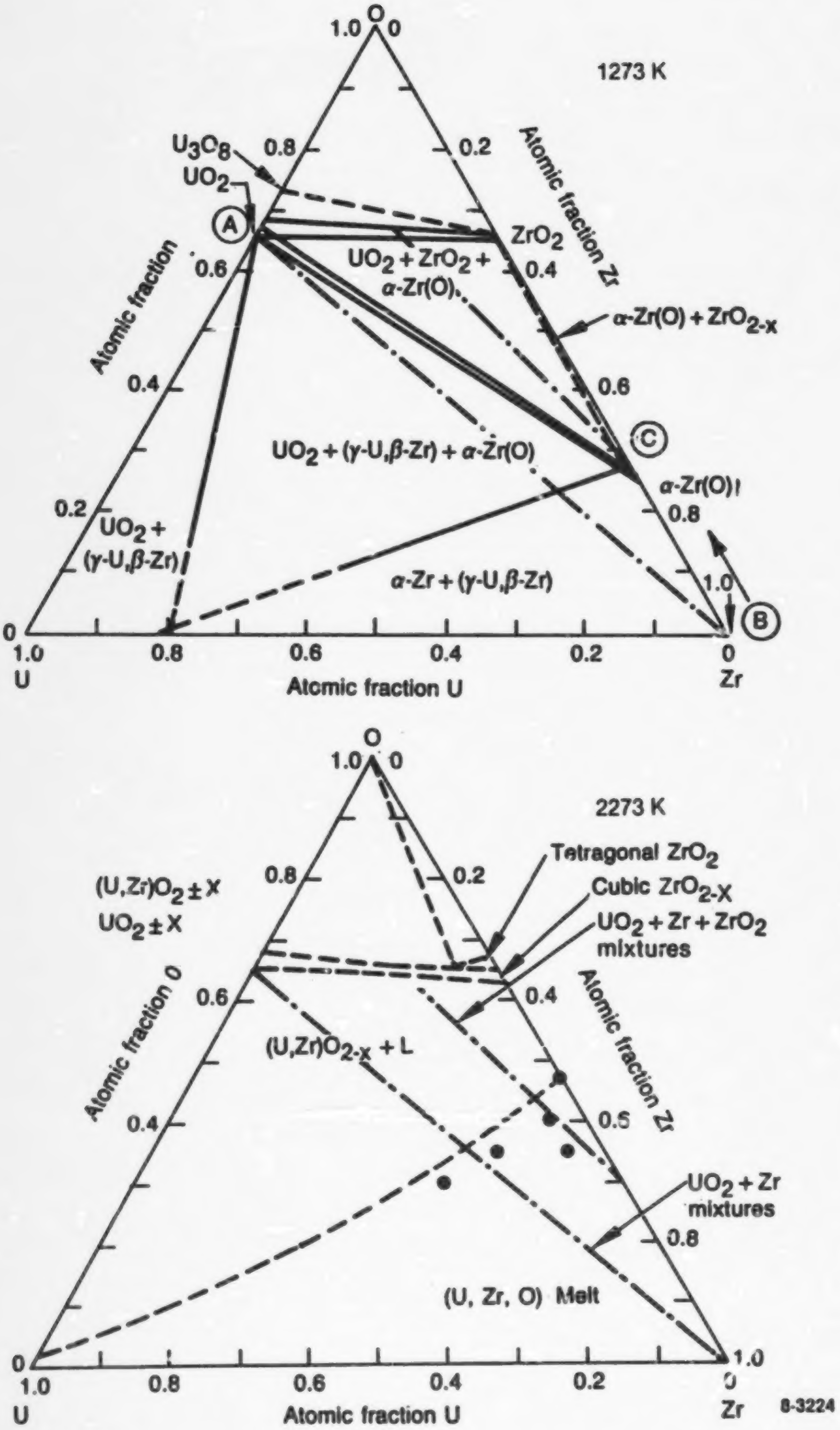

O
1.0
0
1273 K
U_3O_8
UO_2
0.8
0.2
Atomic fraction Zr
Ⓐ
ZrO_2
$UO_2 + ZrO_2 +$
α-Zr(O)
0.6
0.4
Atomic fraction O
α-Zr(O) + ZrO_{2-x}
0.4
0.6
Ⓒ
$UO_2 + (\gamma$-U,β-Zr) + α-Zr(O)
α-Zr(O)
0.2
0.8
$UO_2 +$
(γ-U,β-Zr)
α-Zr + (γ-U,β-Zr)
1.0
Ⓑ
0
1.0
U
0.8
0.6
0.4
0.2
0
Zr
Atomic fraction U
O
1.0
0
2273 K
Tetragonal ZrO_2
Cubic ZrO_{2-x}
$UO_2 + Zr + ZrO_2$
mixtures
(U,Zr)$O_2 \pm X$
$UO_2 \pm X$
0.8
0.2
0.6
0.4
Atomic fraction O
Atomic fraction Zr
(U,Zr)O_{2-x} + L
0.4
0.5
$UO_2 + Zr$
mixtures
0.8
(U, Zr, O) Melt
0
1.0
1.0
U
0.8
0.6
0.4
0.2
0
Zr
Atomic fraction U
8-3224

Figure 29. Equilibrium phase diagram of the (U,Zr,O) ternary system at 1273 and 2273 K, from References 2 and 10.

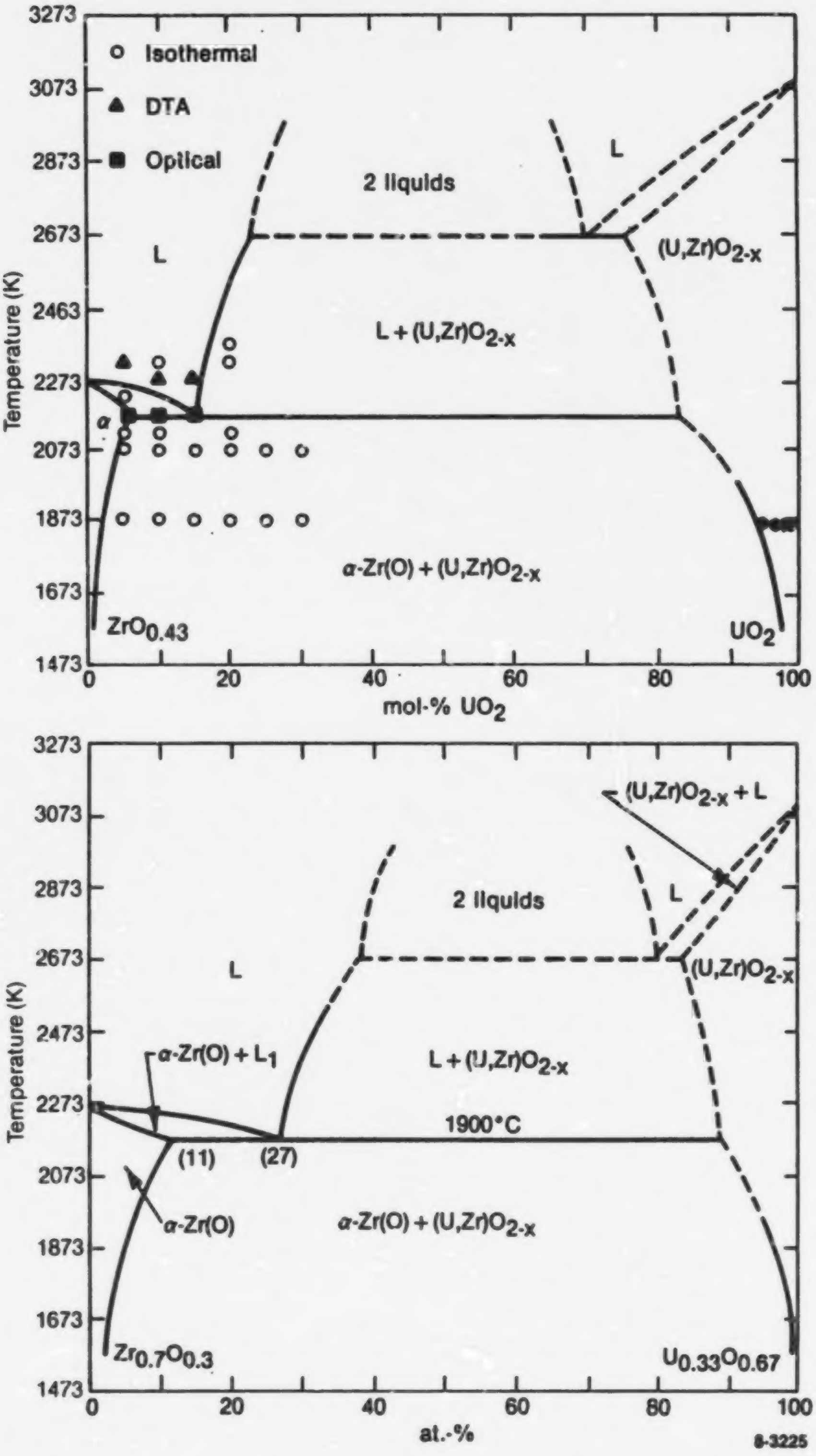

Figure 30. Quasi-binary α-Zr(O)/UO_2 phase diagram in mol% UO_2 and at.% UO_2, from Reference 13.

to room temperature. Note that it is not possible to reach the upper right triangle (α-Zr(O) + UO_2 + ZrO_2) above the tie-line A-C as a result of the UO_2/zircaloy chemical interaction alone, even if the α-Zr(O) is completely oxygen-saturated (30 at.% or 6.7 wt% oxygen). That is, if only one metallic phase [α-Zr(O)] is observed posttest and no (U,Zr) alloy is present, an additional source of oxygen other than UO_2 must have been available (ZrO_2 and/or steam). Melt experiments performed with powder mixtures of $UO_{2.00}$/Zr/$ZrO_{2.00}$ (representing another source of oxygen) confirmed this observation.[1] In every case, only one metallic phase [α-Zr(O)] and one ceramic phase [$(U,Zr)O_2$] were found posttest. The presence of a (U,Zr) alloy therefore indicates that the cladding or the melt picked up little or no additional oxygen from either the atmosphere or dissolved ZrO_2.

Interpretation of the Cross Sections. The fuel rod array of the test train is surrounded by an inner zircaloy liner. Between the zircaloy liner and the zircaloy saddle, high-density ZrO_2 cylinders and low-density ZrO_2 powder were used as insulating material to reduce radial heat loss (Figure 12). After the zircaloy liner failed, the ZrO_2 insulator material entered into the fuel rod bundle region and took part in the chemical interactions. For this reason, the amount of ceramic material in the various cross-section elevations is larger than would be expected in a power reactor fuel rod bundle cross section that has undergone an SFD accident with the same steam availability.

The general appearance of the solidified metallic melt is shown in Figure 31 at different magnifications. The metallic melt penetrated into the solidified ceramic melt along cracks. A fine dendritic structure is visible in the solidified metallic melt, which is shown at higher magnification in Figure 31c. There are three phases present, probably metallic α-Zr(O), a metallic (U,Zr) alloy, and ceramic $(U,Zr)O_2$ particles, which form dendrites on cooldown. The metallic melt interacted with the ceramic melt and was oxidized by steam at free surfaces up to about 80 μm. The presence of the ceramic particles indicates that the metallic material was a heterogeneous (U,Zr,O) melt at temperature. Within the solidified metallic melt are pores of various sizes and a great amount of voidage due to the pullout of material caused by metallographic sample preparation. The etched specimen did not show any additional information compared to the as-polished condition.

The only cross-section elevation where large regions were blocked not only by a ceramic melt but also by a metallic melt is at 0.145 m (Figure 4). Figure 4 shows that the metallic solidified melt is oxidized at all places where the steam had access. A few "coolant channels" formed, similar to those formed during out-of-pile bundle experiments,[4] which are oxidized at their surfaces, e.g., between Rods 1E/2E and 1D/2D, near Rod 2F (90, 180 and 300° orientations), and between Rods 1C/2C and 1D/2D. It appears that the ceramic melt relocated to this elevation first. Then, later in time, the metallic melt reached the same elevation and interacted to a certain extent with the solidified ceramic melt before it solidified itself and was subsequently oxidized at its surface. However, the metallic melt not only interacted with the ceramic solidified melt but also dissolved a part of the fuel and previously oxidized cladding. The strong temperature difference which existed at the 0.145-m cross-section elevation is demonstrated by the intact fuel rods (2A through 5A) compared to the melt-blocked bundle region (Figure 4). At this bundle elevation, the zircaloy liner is still intact, although it is heavily oxidized, and prevented contact between the melt and the ZrO_2 insulator material.

Figure 32 shows a metallic (U,Zr,O) melt which formed at higher elevations and flowed down between the deformed cladding and UO_2 fuel. No chemical interactions between the melt and the solid zircaloy or UO_2 could be recognized. The solidified metallic melt looks two-phase, most probably α-Zr(O) plus a (U,Zr) alloy. The zircaloy cladding shows a very large grain structure (prior β-zircaloy).

Figures 33 through 35 show typical examples of the microstructure of solidified (U,Zr,O) melts, as well as the chemical attack of the previously oxidized cladding by the metallic melt. In Figure 33, one can recognize a part of the previously oxidized cladding surrounded by the metallic melt. (Figure 4 shows the whole cladding circumference.) A higher magnification of the cladding remnant shows several interesting features. The oxidized cladding was strongly attacked by the metallic (U,Zr,O) melt. The metallic melt decomposed during cooldown into α-Zr(O), which contains some uranium, and a (U,Zr) alloy as described previously. The amount of fuel dissolved in the melt was below 35 wt% UO_2.[1,9] In the ZrO_2 phase, α-Zr(O) precipitates form in correspondence with the (Zr-O) phase diagram (Figure 14), since one has to assume that the ZrO_2 was substoichiometric at temperature due to the melt attack, resulting in a dissolution of the

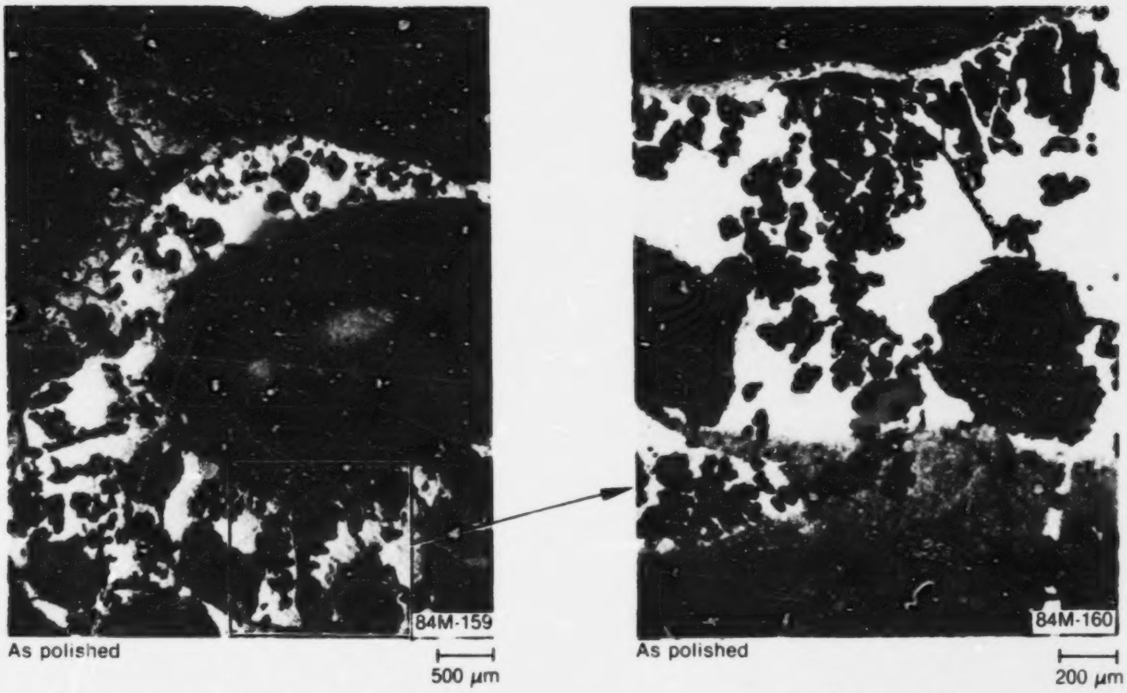
84M-159
As polished
500 μm
84M-160
As polished
200 μm

(a) Penetration of the metallic melt into the solidified ceramic melt by flowing into cracks

(b) Detail of (a)

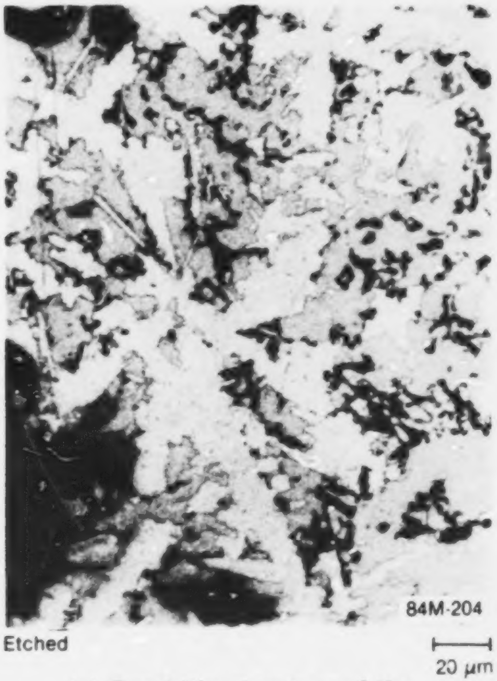
84M-204
Etched
20 μm

(c) Dendritic structure of the metallic melt shown in (a)

4 2040

Figure 31. Solidified ceramic and metallic melts near Rod 4D, 45°, at the 0.145-m cross-section elevation.

BEST COPY AVAILABLE

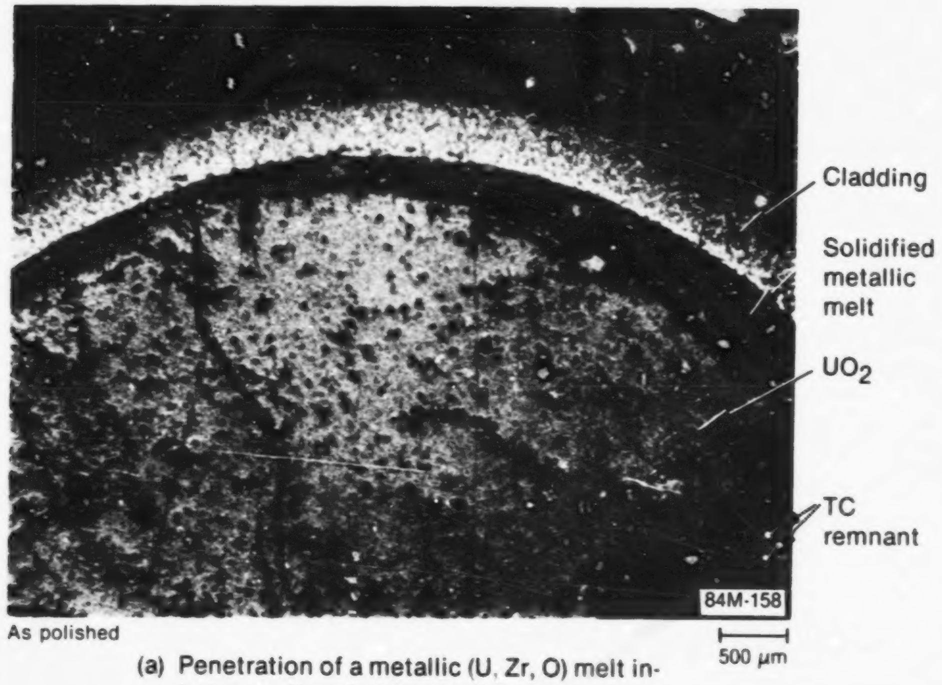
Cladding
Solidified metallic melt
UO2
TC remnant
84M-158
As polished
500 μm

(a) Penetration of a metallic (U, Zr, O) melt in-between the cladding and fuel

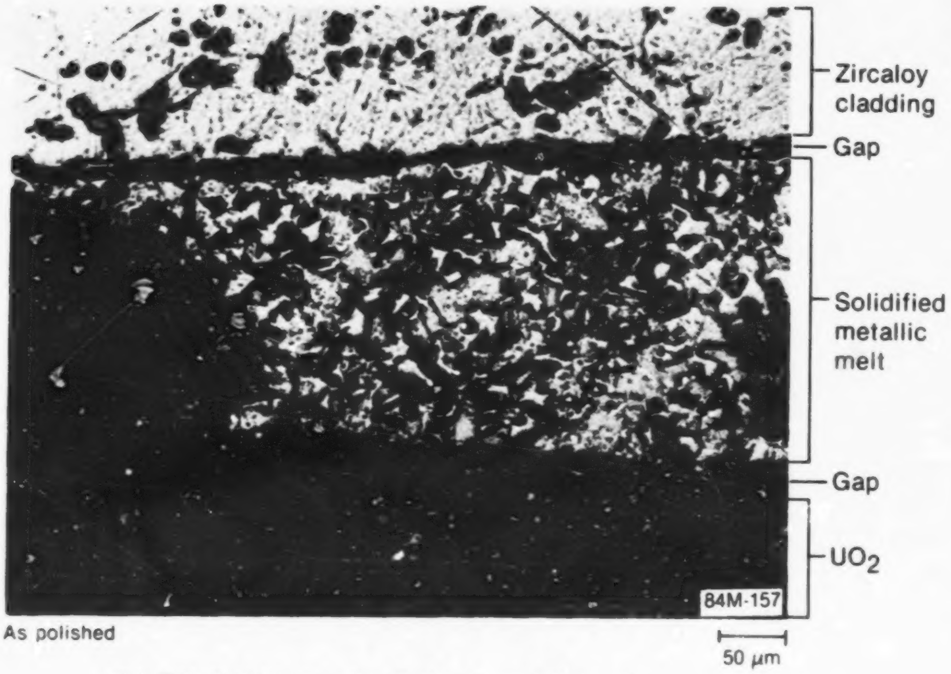
Zircaloy cladding
Gap
Solidified metallic melt
Gap
UO2
84M-157
As polished
50 μm

(b) Detail of (a) showing 2-phase metallic melt

4 2041

Figure 32. Penetration of a metallic (U,Zr,O) melt in between the cladding and fuel gap (Rod 4B, 180°, at the 0.145-m cross-section elevation).

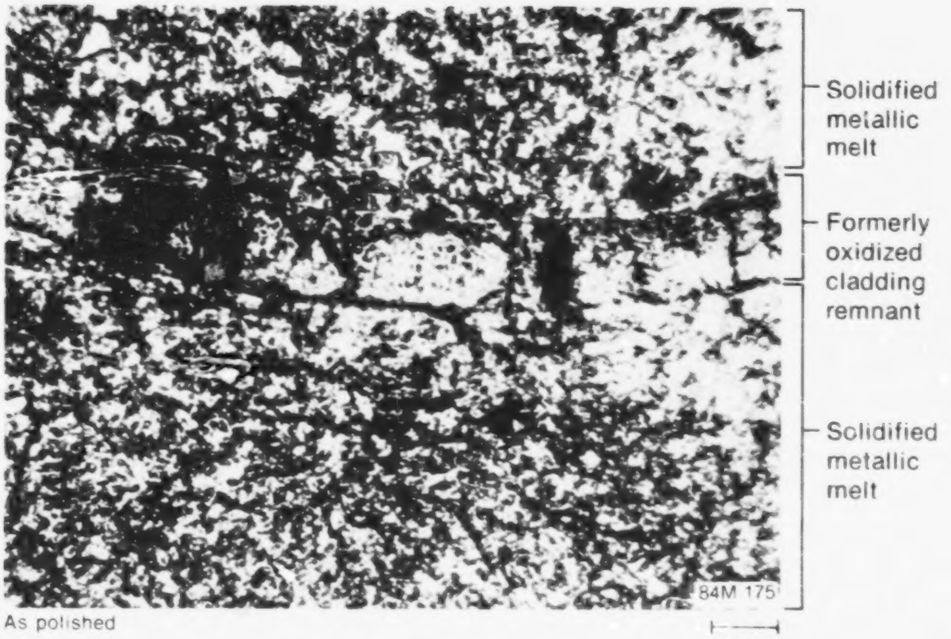
Solidified metallic melt
Formerly oxidized cladding remnant
Solidified metallic melt
84M 175
As polished
200 μm

(a) A part of the formerly oxidized cladding remnant within the melt

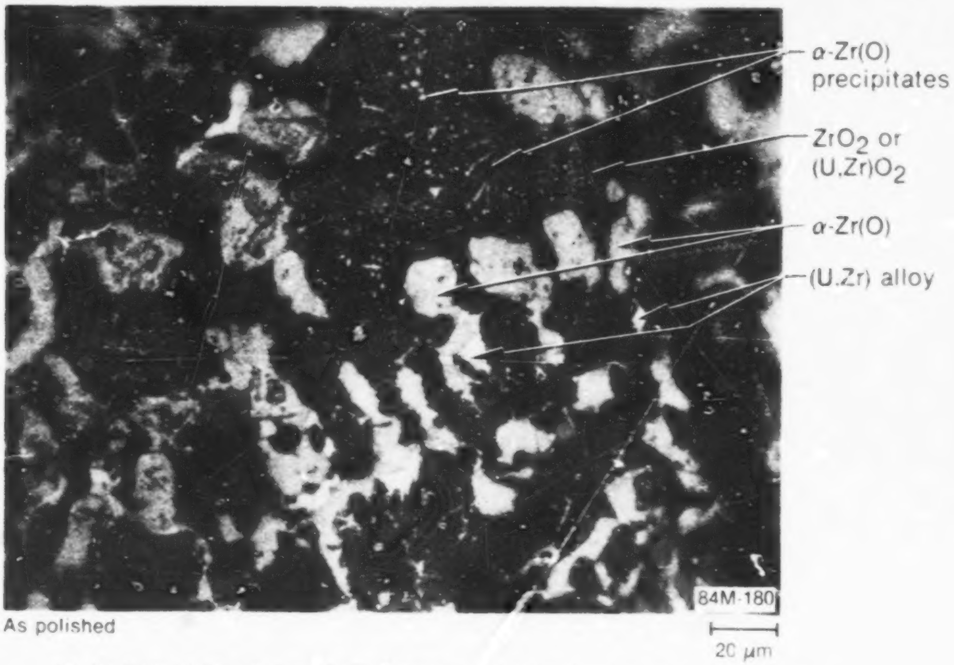
α-Zr(O) precipitates
ZrO_2 or $(U,Zr)O_2$
α-Zr(O)
(U,Zr) alloy
84M-180
As polished
20 μm

(b) Detail of the formerly oxidized and attacked cladding

4 2042

Figure 33. Solidified metallic melt near Rod 2E, 45°, at the 0.145-m cross-section elevation.

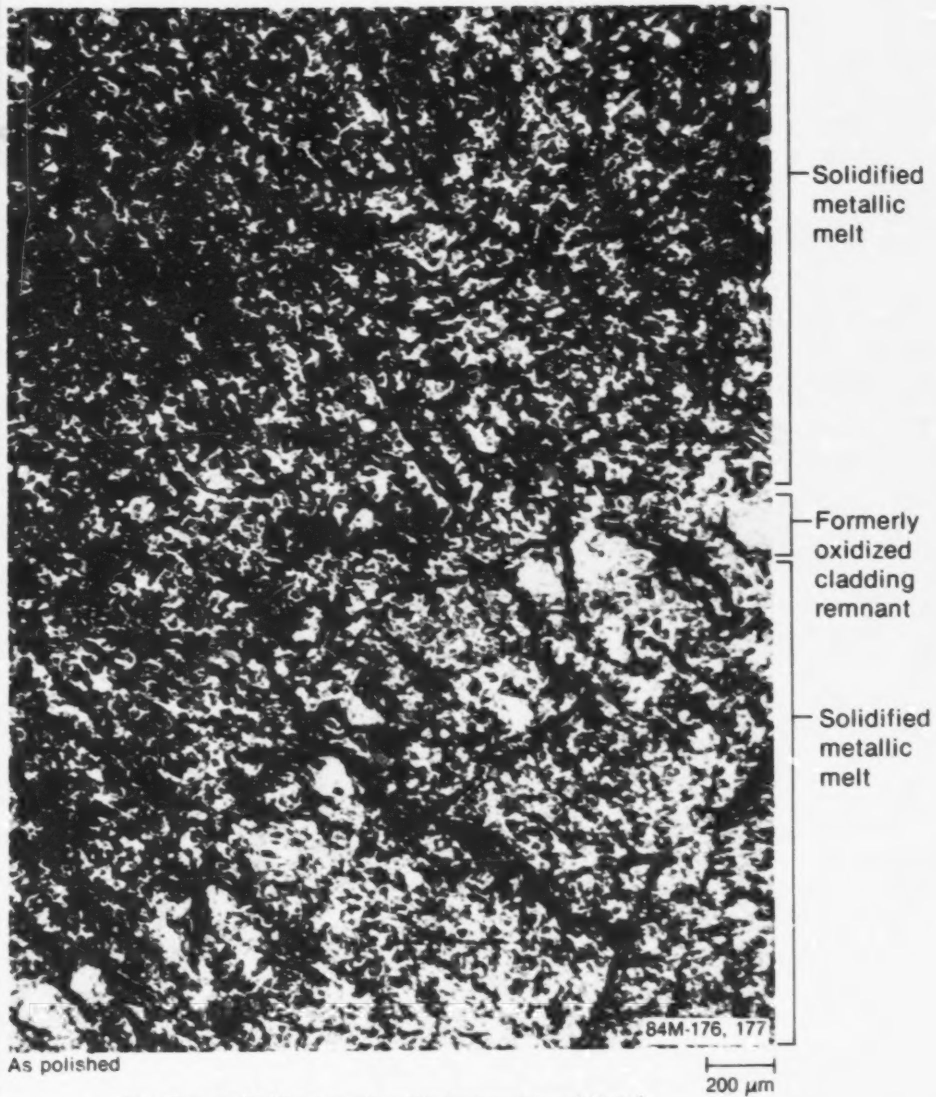
Solidified metallic melt
Formerly oxidized cladding remnant
Solidified metallic melt
84M-176, 177
As polished
200 μm

(a) The solidified melt with formerly oxidized cladding remnant

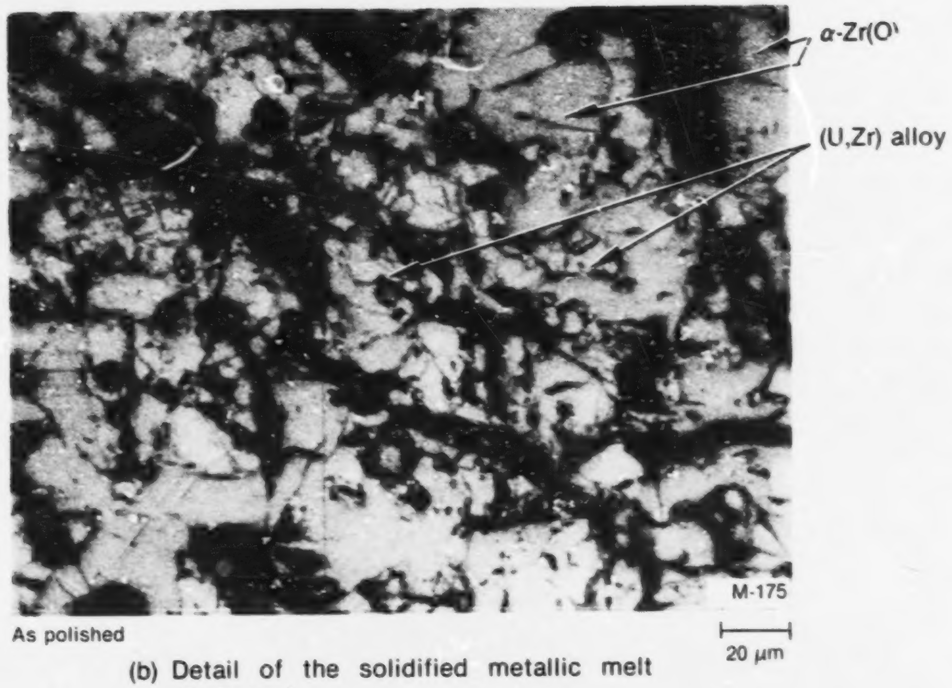
α-Zr(O)
(U,Zr) alloy
M-175
As polished
20 μm

(b) Detail of the solidified metallic melt (2-phases)

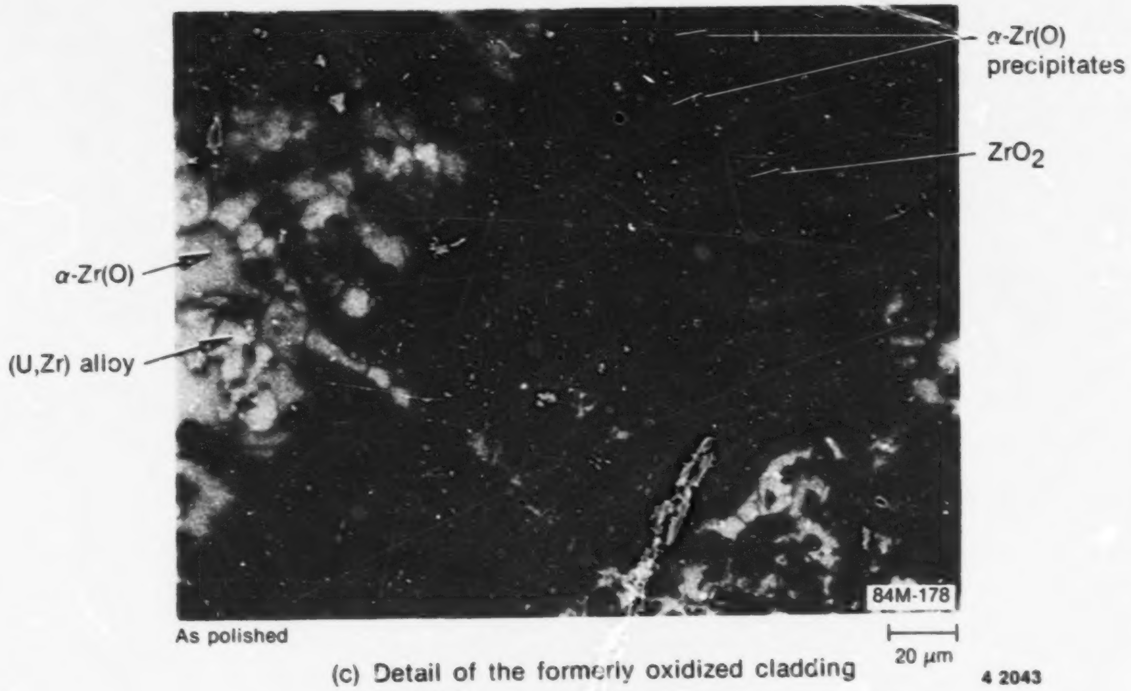
α-Zr(O) precipitates
ZrO_2
α-Zr(O)
(U,Zr) alloy
84M-178
As polished
20 μm

(c) Detail of the formerly oxidized cladding remnant

4 2043

Figure 34. Solidified melt between Rods 2E (45°) and 3D (225°) at the 0.145-m cross-section elevation.

BEST COPY AVAILABLE

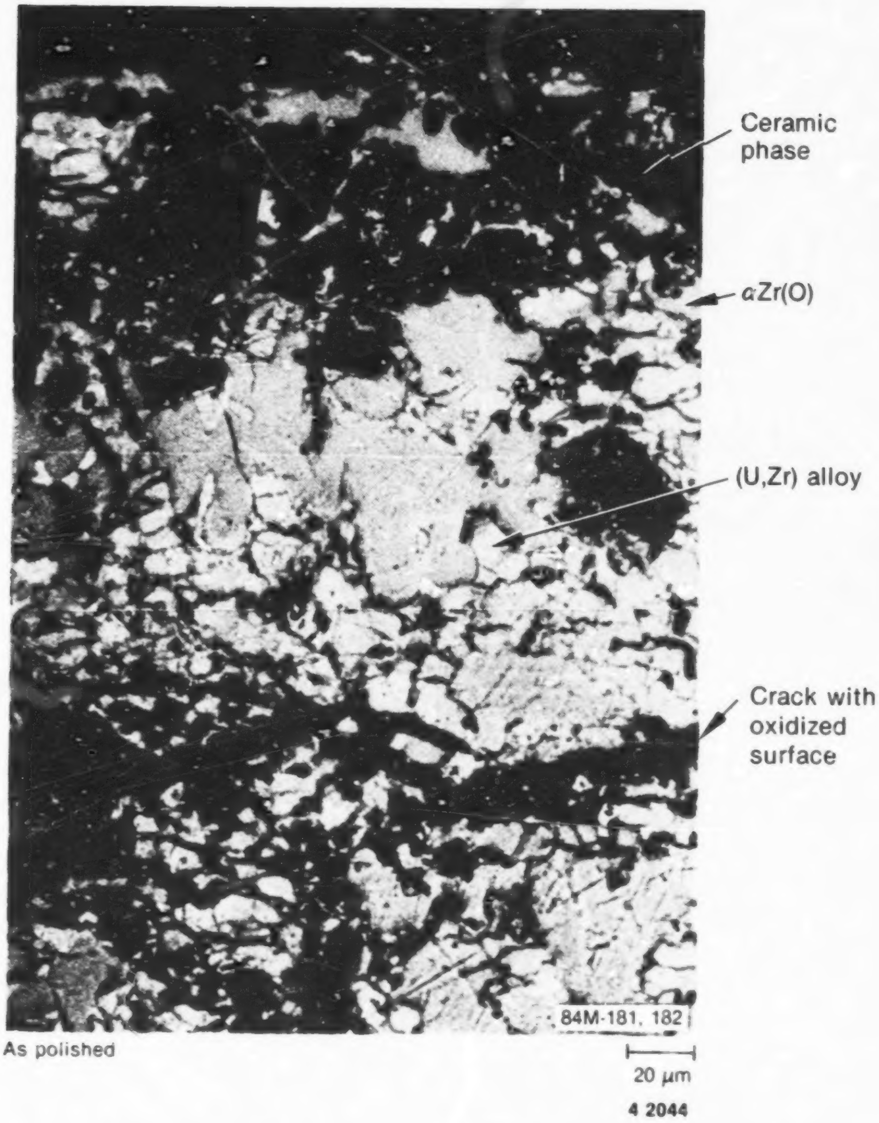
Ceramic phase
αZr(O)
(U,Zr) alloy
Crack with oxidized surface
84M-181, 182
As polished
20 μm
4 2044

Figure 35. Solidified metallic melt between oxidized cladding and UO_2 fuel (Rod 4F, 270°, at the 0.145-m cross-section elevation). The solidified metallic melt was oxidized by steam later in time along open cracks.

ZrO_2. Similar structures can be seen in Figure 34. In this case, the previously oxidized cladding was not as heavily attacked by the metallic melt as in Figure 33. The α-Zr(O) precipitates in the ZrO_2 form a fine, needle-like structure. The etching of the specimen removed most of the metallic phases.

Figure 35 shows details of the metallic (U,Zr,O) melt which completely surrounds the fuel pellets of Rod 4F (270°) and which is itself surrounded by a ceramic melt (Figure 4). Perhaps the unoxidized part of the cladding melted when the ceramic melt reached this elevation. The solidified metallic melt contains cracks whose surfaces are oxidized by steam. Besides the α-Zr(O) and (U,Zr) alloy, one can also recognize a ceramic $(U,Zr)O_2$ phase (Figure 35), probably due to late oxidation of the solidified metallic (U,Zr,O) melt.

Figure 36 shows two solidified metallic (U,Zr,O) melts near Rod 2D (45°) at the 0.055-m cross-section elevation (Figure 3) which are oxidized to different extents at their surfaces. The reason for different degrees of external oxidation may be that the melts formed and/or reached this elevation at different times. With respect to the microstructure, the (U,Zr,O) melt may have dissolved about 20 wt% UO_2. One can recognize the dendritic formation of α-Zr(O), which solidifies first, in the melt. The amount of α-Zr(O) phase at the surface is much higher than in the center of the solidified melt, revealing some oxygen uptake already in the liquid state. The microstructure of this specimen is probably very similar to that of Figure 31 at some locations.

At the 0.245-m cross-section elevation (Figure 6), many areas of various sizes showing metallic phases within the ceramic phase are present. Figure 37 shows a section of one of these solidified metallic melts at different magnifications. One can recognize a pronounced dendritic segregation, resulting in a cored structure of the dendrites. In this case, the metallic melt probably does not consist of a (U,Zr,O) mixture. It probably is a more oxidation-resistant alloy, such as Inconel, thermocouple wire (tungsten/rhodium), or sheath material (molybdenum/rhenium). It also may be a mixture of various elements.

If one compares the microstructure of Figure 37 with that of well defined reference specimens,[9] the melt appears to be an Inconel/zircaloy reaction product. It may also contain some molybdenum, rhodium, rhenium, tungsten, or even uranium. However, this can only be clarified by elemental analysis. The dendrite could exist mainly of a (Zr,Cr,Fe) alloy and the matrix of a (Zr,Ni) mixture.

The coring is a typical effect of the solidification of an alloy over a freezing range, which begins with the appearance of small, solid particles which contain more of the higher-melting component metal than any other subsequently formed solid. Successive layers of the solid phase are deposited on the nucleating crystallites, each layer being a little richer than its predecessor in the low-melting component. The final solid is composed, then, of a "cored" structure, in which each unit has a high-melting central portion surrounded by lower-melting material.[14] A majority of metals freeze by the formation of treelike growths, called dendrites.

During the cooldown of the metallic (U,Zr,O) melts, no coring was observed in either Test SFD-ST (Figure 36) or in all the extensive out-of-pile melting experiments.[1,9] The black areas in Figure 37 are pullouts which formed during metallographic sample preparation.

Similar, but different looking, metallic phases have been observed at other locations of the 0.245-m elevation and at other cross-section elevations (Figures 38 through 40). In most cases, the solidified melts were surrounded by ceramic material. However, apparently no, or only small, chemical interactions took place between the metallic and ceramic materials. Figure 38 shows two other phases beside the dendrite formation. The microstructure of Figure 39 also reveals pronounced dendritic segregation. The chemical composition of the various phases is not known; but, in all cases (Figures 37 through 40) it is probably not a solidified (U,Zr,O) melt. Figure 40c shows one example of the dendrites, which form in the metallic melt during cooldown, consisting of ceramic material. After special etching, the microstructure of the matrix reveals eutectic or eutectoid decomposition.

Another interesting aspect of the metallic inclusions in the solidified ceramic melts is the different wetting behavior of the metallic phase with respect to the ceramic phase. It varies over a broad range, indicating that the chemical composition of the metallic melts also varies, since the chemical composition of the various ceramic materials is considered to be very similar.

If the homogeneous (U,Zr,O) or (Zr,O) melts exceed a certain oxygen concentration due to chemical interactions with steam, UO_2, and/or ZrO_2, solid ZrO_2 or $(U,Zr)O_2$ particles form and the melts become heterogeneous. (The oxygen concentration required for this phenomenon is temperature-dependent.) The metallic melt either decomposes,

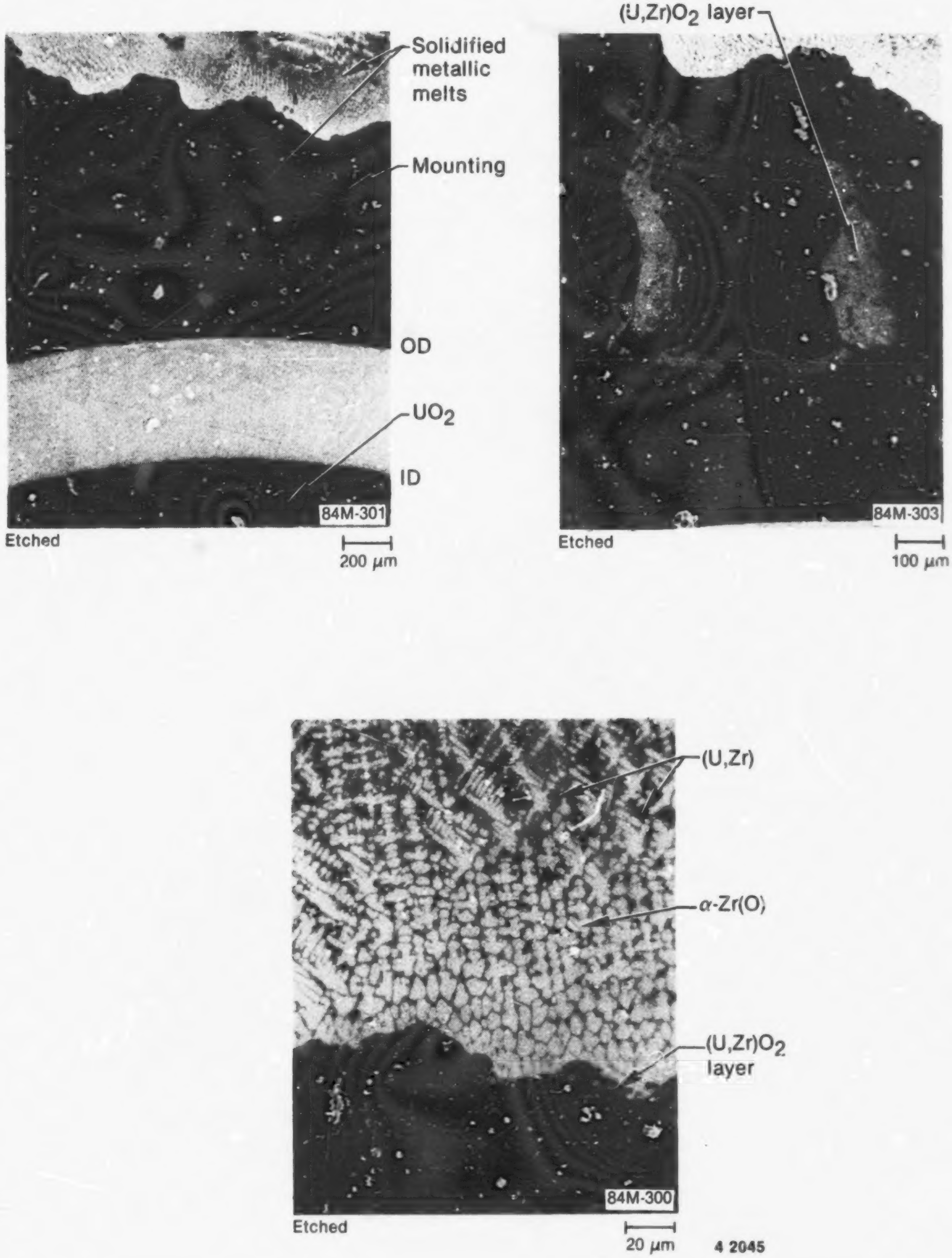
Solidified metallic melts
Mounting
OD
UO2
ID
84M-301
Etched
200 μm
(U,Zr)O2 layer
84M-303
Etched
100 μm
(U,Zr)
α-Zr(O)
(U,Zr)O2 layer
84M-300
Etched
20 μm
4 2045

Figure 36. Solidified metallic (U,Zr,O) melts near Rod 2D, 45° at the 0.055-m cross-section elevation, showing different degrees of external oxidation.

BEST COPY AVAILABLE

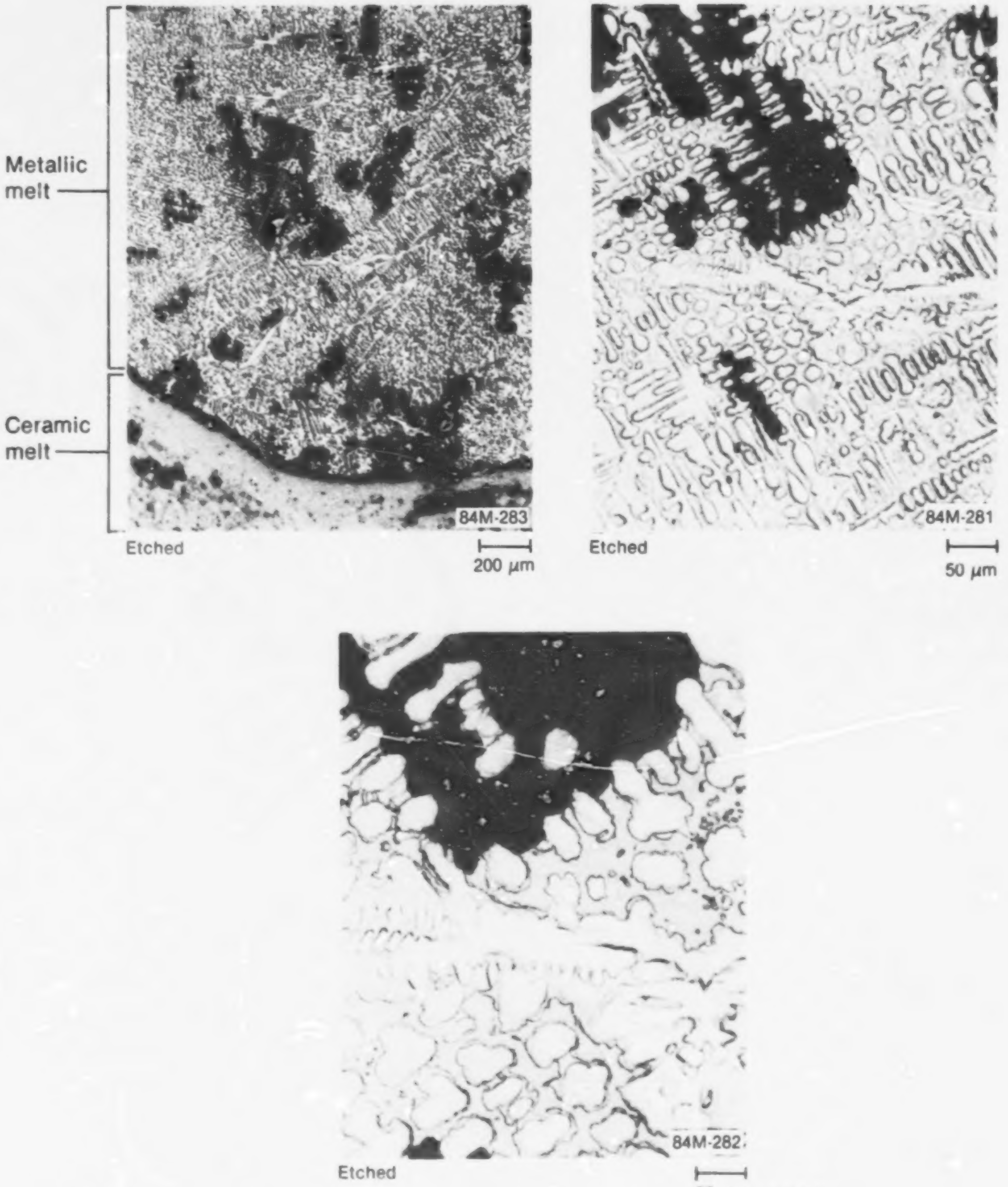
Metallic melt
Ceramic melt
84M-283
Etched
200 μm
84M-281
Etched
50 μm
84M-282
Etched
20 μm
4 2046

Figure 37. Solidified metallic melt near Rod 2D, 30°, at the 0.245-m cross-section elevation, showing pronounced dendritic segregation and coring of the precipitates.

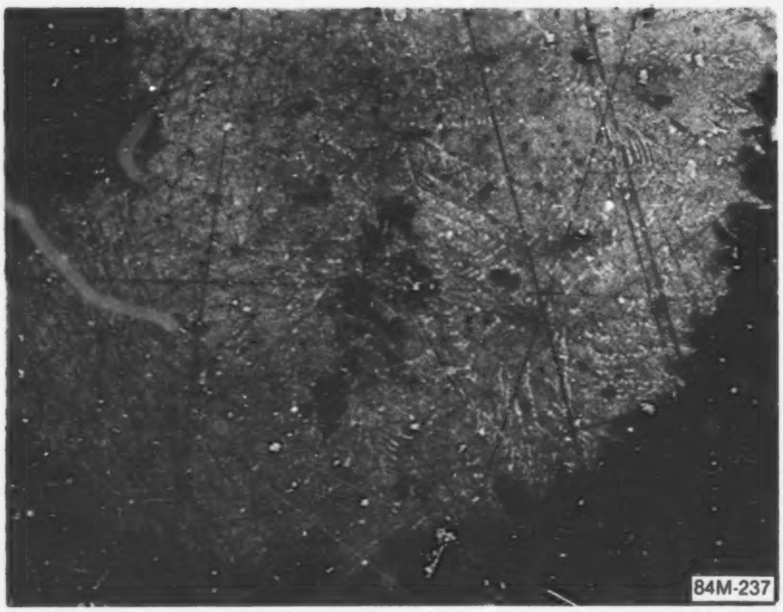
84M-237

As polished

200 μm

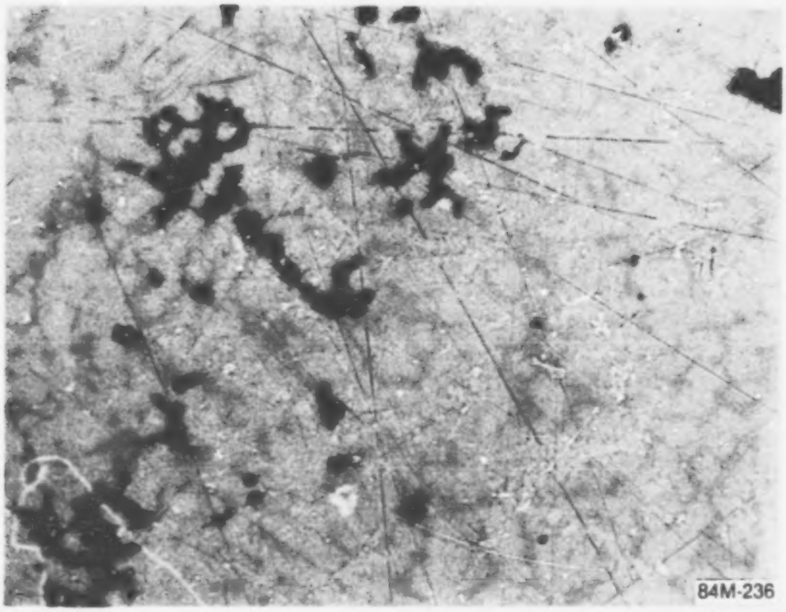
84M-236

As polished

50 μm

4 2047

Figure 38. Solidified metallic melt near Rod 3D, 135°, at the 0.245-m cross-section elevation.

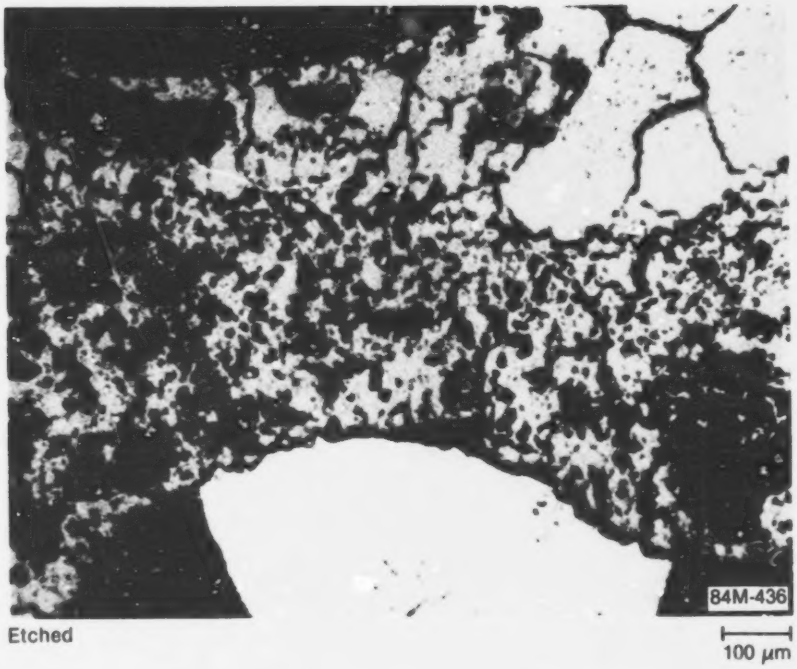
84M-436
Etched
100 μm

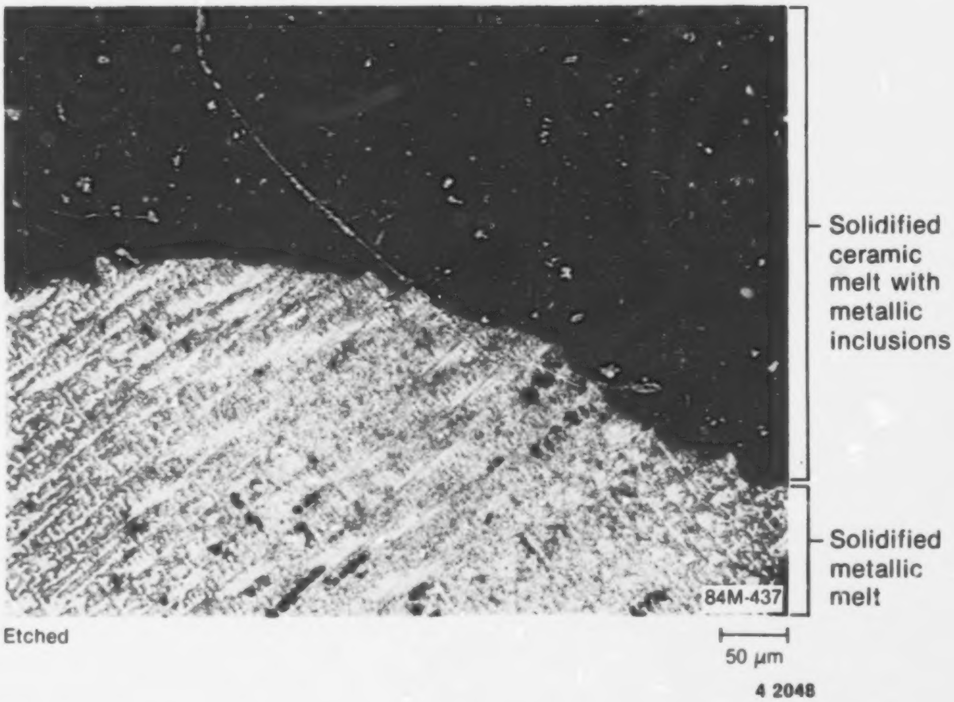
Solidified ceramic melt with metallic inclusions
Solidified metallic melt
84M-437
Etched
50 μm
4 2048

Figure 39. Solidified metallic melt in contact with ceramic material near Rod 6E, 90°, at the 0.27-m cross-section elevation.

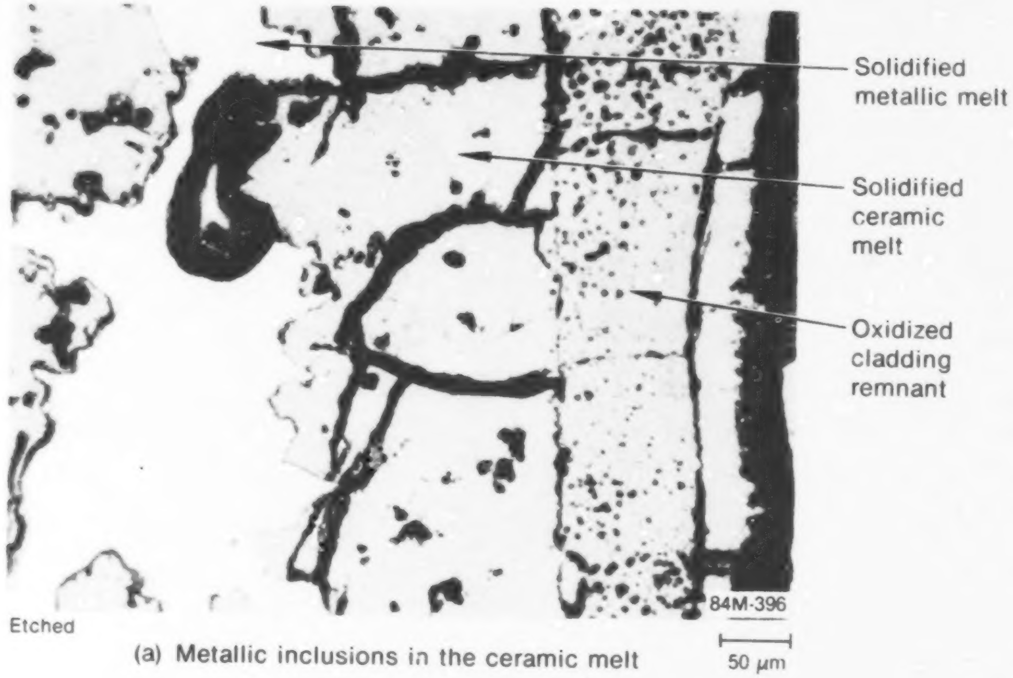
Solidified metallic melt
Solidified ceramic melt
Oxidized cladding remnant
Etched
84M-396
50 µm

(a) Metallic inclusions in the ceramic melt

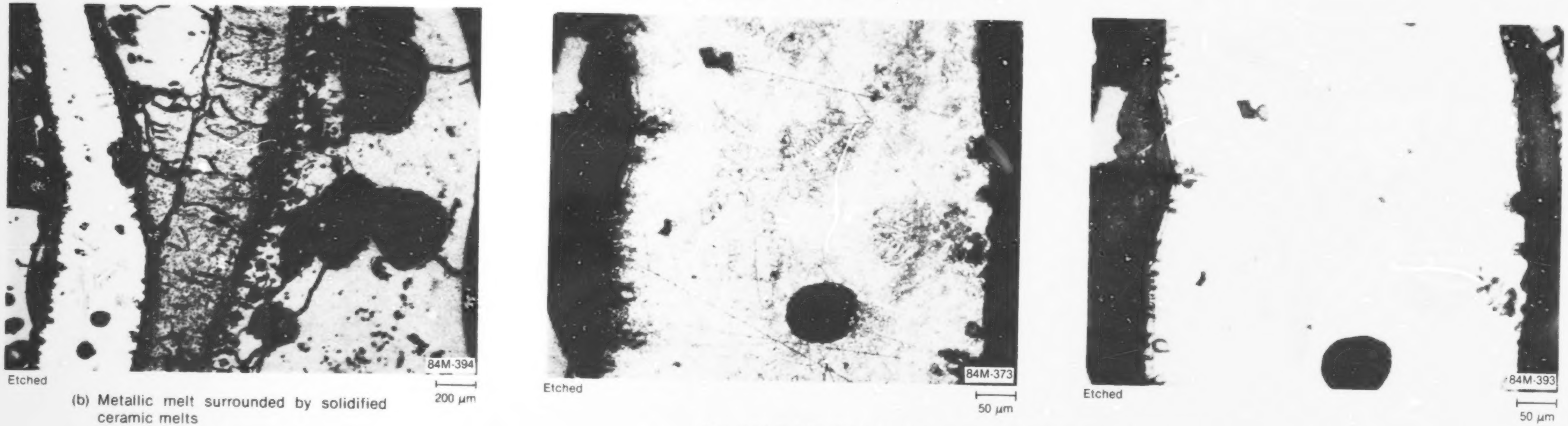
Etched
84M-394
200 µm
Etched
84M-373
50 µm
Etched
84M-393
50 µm

(b) Metallic melt surrounded by solidified ceramic melts

(c) and (d) Details of (b) showing the ceramic dendritic structures and typical eutectic or eutectoid decomposition

4 2049

Figure 40. Metallic inclusions in the ceramic material (object number 10, 315°, at the 0.495-m cross-section elevation.

as described previously, or freezes. For example, depending on its chemical composition, (Zr,O) melt freezes to solid α-Zr(O).

Figures 41 and 42 show typical examples of solidified, heterogeneous (U,Zr,O) melts. The microstructure shows two metallic phases [α-Zr(O) and a (U,Zr) alloy] and one ceramic phase [$(U,Zr)O_2$]. The amounts of dissolved fuel at temperature could be about 60 wt% UO_2 (Figure 41) and 40 wt% UO_2 (Figure 42). The surface of the solidified melt is oxidized. In the etched condition, the specimen does not reveal any additional information. Figure 42 also shows a chemical attack of previously oxidized zircaloy cladding by the metallic melt.

At first glance, Figure 43 shows a microstructure similar to that of Figure 42. However, it looks as though the matrix consists of only one metallic phase which contains a homogeneously distributed ceramic phase. It could be α-Zr(O) containing ZrO_2; however, this area was not examined at higher magnification. In both specimens (Figures 42 and 43), no pronounced dendritic structure is visible, which may indicate that most of the ceramic phases were already present at test temperature and only a few formed during cooldown.

In the following, the physical behavior (wetting behavior) of molten, metallic cladding and its gradual chemical change with time during the temperature transient will be described. The unoxidized metallic part of the cladding will melt first and flow down the fuel pellet stack, penetrating into cracks and open volumes (dishes) of the pellets. At the same time, chemical interactions take place with the UO_2, and also with the environment and the oxidized cladding. As a result, the chemical composition of the melt changes continuously with time. This chemical change has a great impact on the wetting behavior of the solid fuel by molten zircaloy, as extensive wetting experiments have shown.[7,10] As-received (oxygen-poor) zircaloy wets UO_2 very poorly, and the chemical interactions between the melt and the solid UO_2 are initially minor. As the zircaloy melt picks up oxygen, the wetting behavior improves and the contact area between the melt and the UO_2 increases substantially. The reaction rate then increases, and the rate of molten cladding runoff will be reduced. The runoff rate will be reduced further if the melt contains a large amount of ceramic precipitates, as occurs with high-oxygen contents. The melt can solidify due to oxygen uptake to form a $(U,Zr)O_2$ solid solution, and it also solidifies due to the axial temperature drop as it runs down the rod. The oxygen-rich melt, which has good wetting properties, also penetrates into pellet cracks and reacts rapidly with the fuel.[7,10] These phenomena have all been observed in melting experiments with LWR fuel rod simulators or fuel rod segments[4,11,12] and were also observed in Test SFD-ST.

Figure 44 shows a homogeneous metallic (U,Zr,O) melt within cracks of a UO_2 fuel pellet. The melt penetrates laterally through the crack into the fuel (up to 60 μm) and dissolves it. The solidified metallic melt in the crack shows two metallic phases, α-Zr(O) and a (U,Zr) alloy. The amount of dissolved UO_2 in the zircaloy melt should be smaller than about 25 wt% UO_2. At the crack opening, a ceramic phase exists within the solidified metallic melt, and nearly a complete oxidation of the melt surface ($\approx$20 μm) can be recognized, probably due to chemical interactions with steam. Figure 44c shows the onset of UO_2 fuel disintegration due to chemical interactions with the metallic melt. Parts of the solid UO_2 grains are nearly completely surrounded by the melt. In a later step, the loose fuel grains or particles are then dispersed in the melt and are rapidly dissolved because of their large surface area. By this process, the fuel is "liquefied" far below its melting point.[7] However, due to the limited volume of melt in the crack, no sudden disintegration of the solid fuel is expected based on observations in laboratory experiments.[7]

In most cases, the metallic (U,Zr,O) melts which penetrated into UO_2 cracks were finally completely oxidized to a $(U,Zr)O_2$ solid solution. Figure 45 shows a typical example of a fuel pellet in which parts of the cracks are filled with a ceramic material. The photograph of the 0.245-m cross-section elevation (Figure 6) shows that Rod 5B is more than 50% surrounded by ceramic material. The zircaloy cladding has gone. Figure 45a is an overview of a part of the pellet. The cracks which are not filled with a ceramic material probably were not present during the test and formed during cooldown. Figures 45b and 45c show higher magnifications of the crack region. Although the ceramic material within the cracks is in general very porous, the matrix itself looks highly dense and single-phase (Figure 45c) and has, in the unetched state, the same color as the UO_2 fuel. Figures 45d and 45e show the fuel pellet-ceramic melt interface at different magnifications. The solidified ceramic melt looks single-phase in the as-polished condition (except for a few very small metallic inclusions), but two-phase in the etched state (Figure 45d).

Whether or not the ceramic melt which surrounds the pellet of Rod 5B was initially metallic before it oxidized cannot be decided. The same question applies to the whole ceramic blockage at

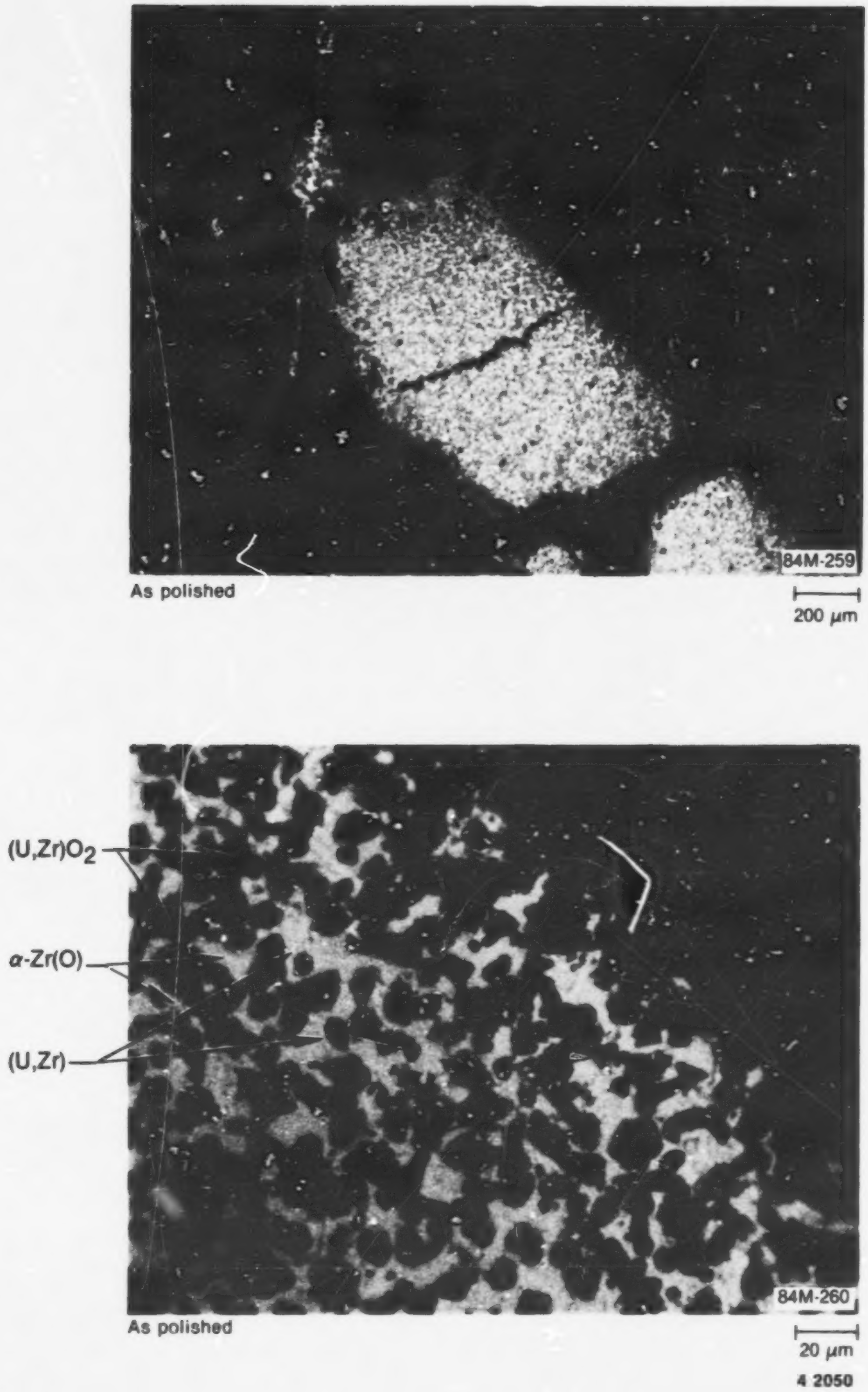
84M-259
As polished
200 μm
(U,Zr)O2
α-Zr(O)
(U,Zr)
84M-260
As polished
20 μm
4 2050

Figure 41. Solidified heterogeneous, metallic (U,Zr,O) melt that contained solid $(U,Zr)O_2$ particles at temperature (debris near Rod 6E, 90°, at the 0.245-m cross-section elevation).

BEST COPY AVAILABLE

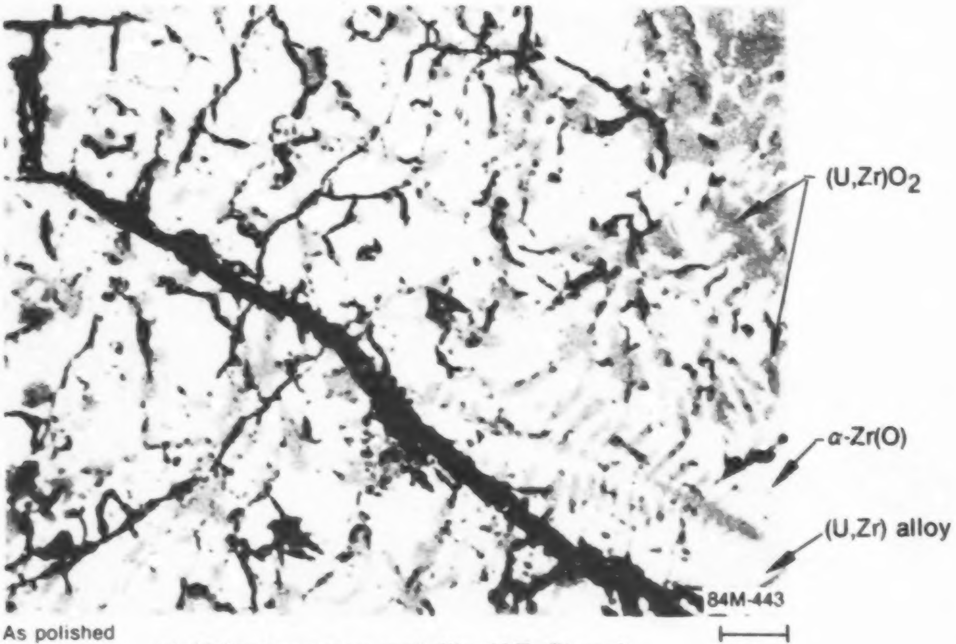
(U,Zr)O$_2$
α-Zr(O)
(U,Zr) alloy
84M-443
As polished
50 µm

(a) Heterogeneous metallic (U,Zr,O) melt

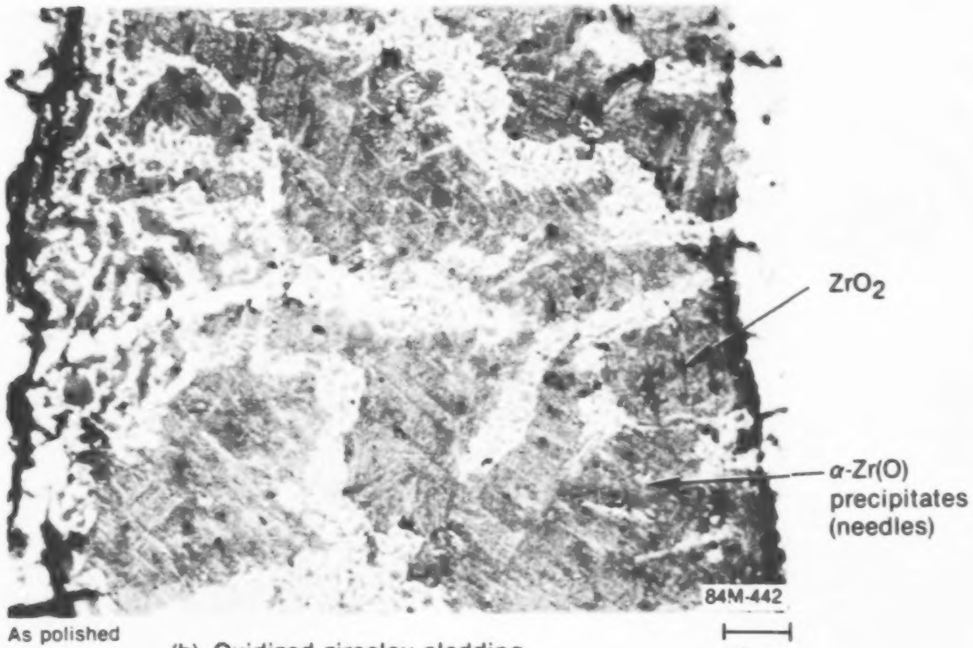
ZrO$_2$
α-Zr(O) precipitates (needles)
84M-442
As polished
50 µm

(b) Oxidized zircaloy cladding

4 2051

Figure 42. Heterogeneous metallic (U,Zr,O) melt attacking formerly oxidized zircaloy cladding (large, semi-metallic mass near 0° orientation at the 0.17-m cross-section elevation).

BEST COPY AVAILABLE

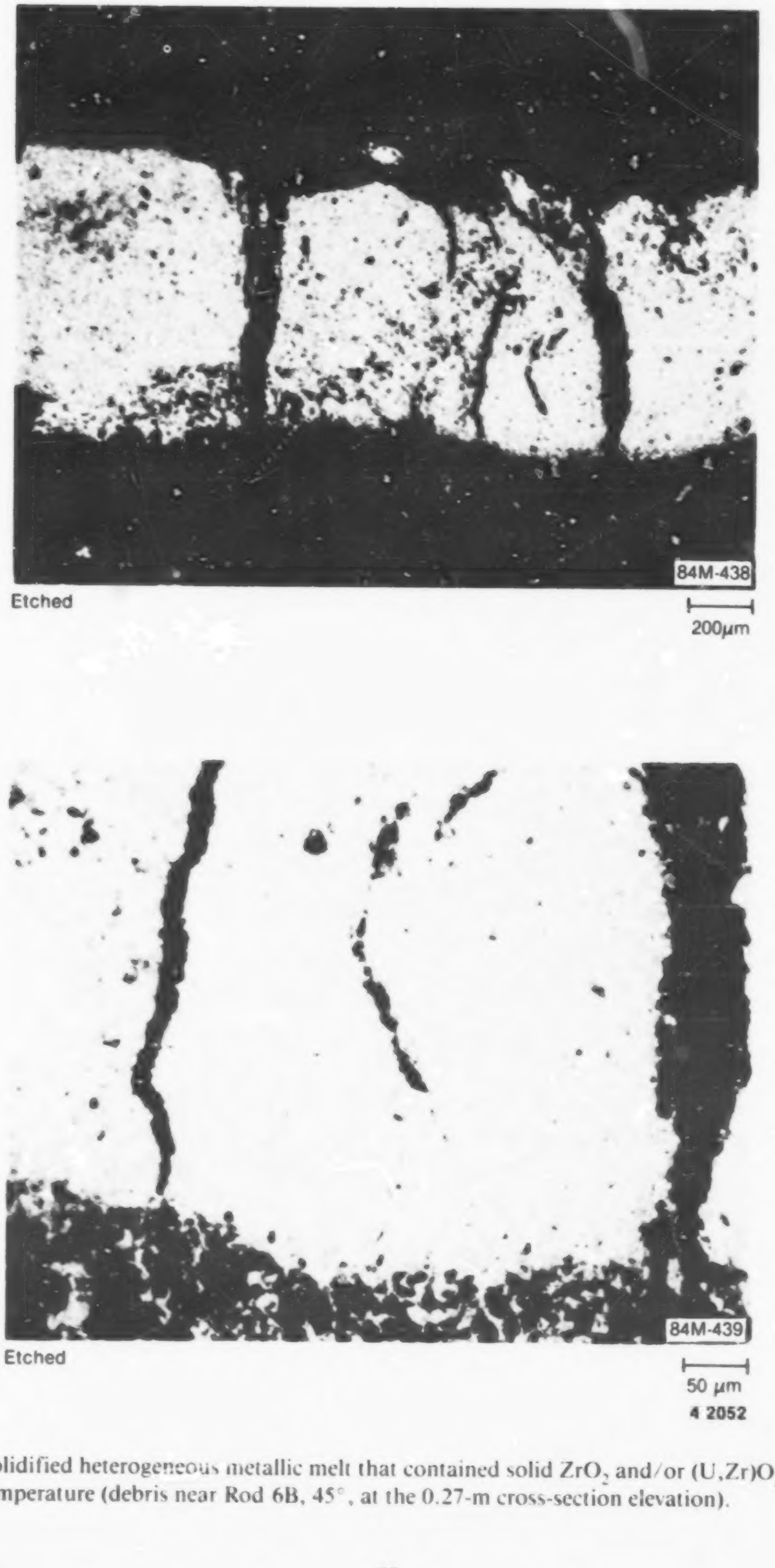
84M-438
Etched
200μm
84M-439
Etched
50 μm
4 2052

Figure 43. Solidified heterogeneous metallic melt that contained solid ZrO_2 and/or $(U,Zr)O_2$ particles at temperature (debris near Rod 6B, 45°, at the 0.27-m cross-section elevation).

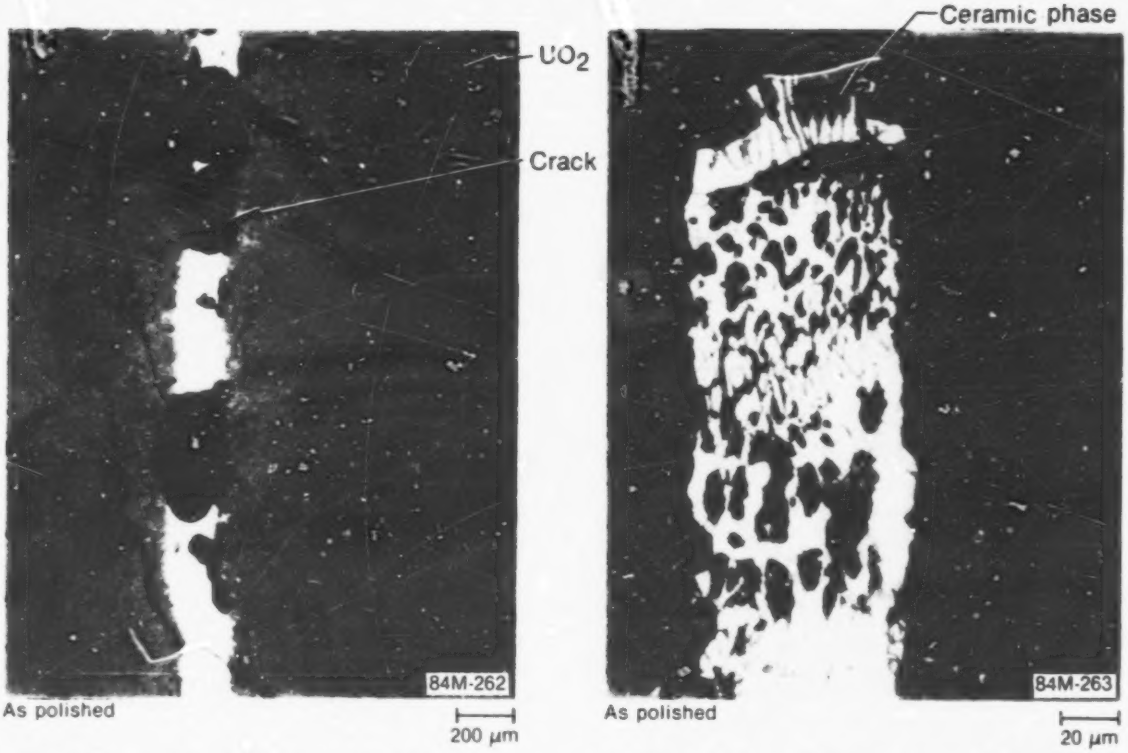
UO2
Crack
84M-262
As polished
200 μm
Ceramic phase
84M-263
As polished
20 μm

(a) Homogeneous metallic (U, Zr, O) melt in fuel crack

(b) Detail of (a) showing a ceramic phase within the metallic melt at the pellet crack opening

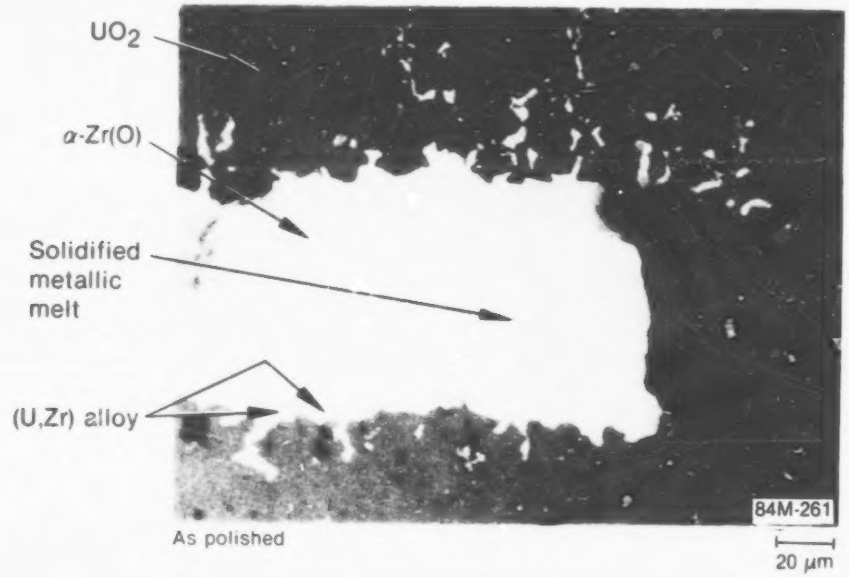
UO2
α-Zr(O)
Solidified metallic melt
(U,Zr) alloy
84M-261
As polished
20 μm

(c) Detail of (a) showing the onset of fuel pellet dissolution by the α-Zr(O) + (U, Zr) alloy metallic melt

4 2053

Figure 44. Homogeneous metallic (U,Zr,O) melt penetrating along a crack into a UO_2 pellet with simultaneous chemical attack (dissolution) of the UO_2 (pellet near Rod 6E, 90°, at the 0.245-m cross-section elevation).

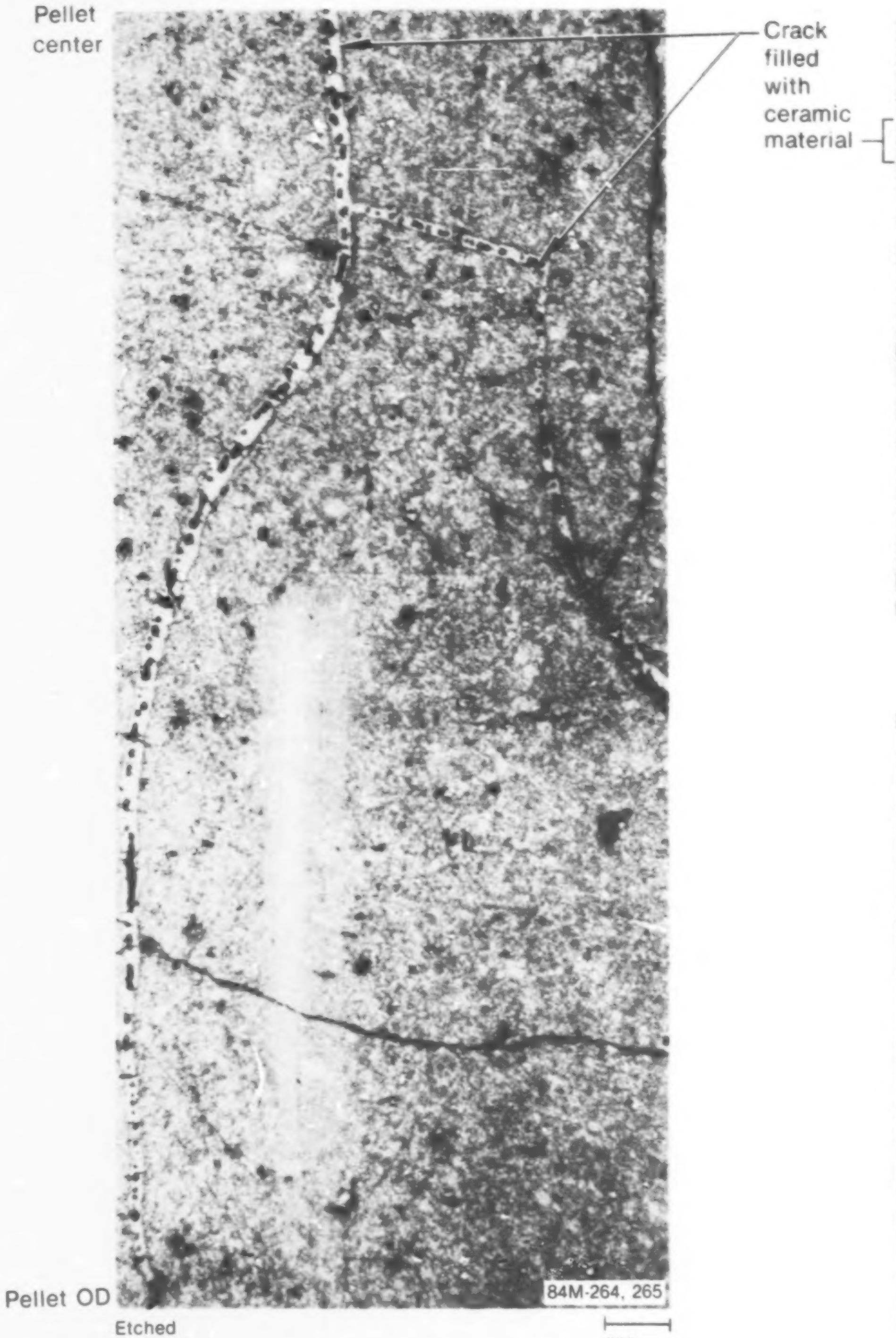
Pellet center
Crack filled with ceramic material
Pellet OD
Etched
84M-264, 265
200 μm

(a) Cracks in a fuel pellet filled with a ceramic material

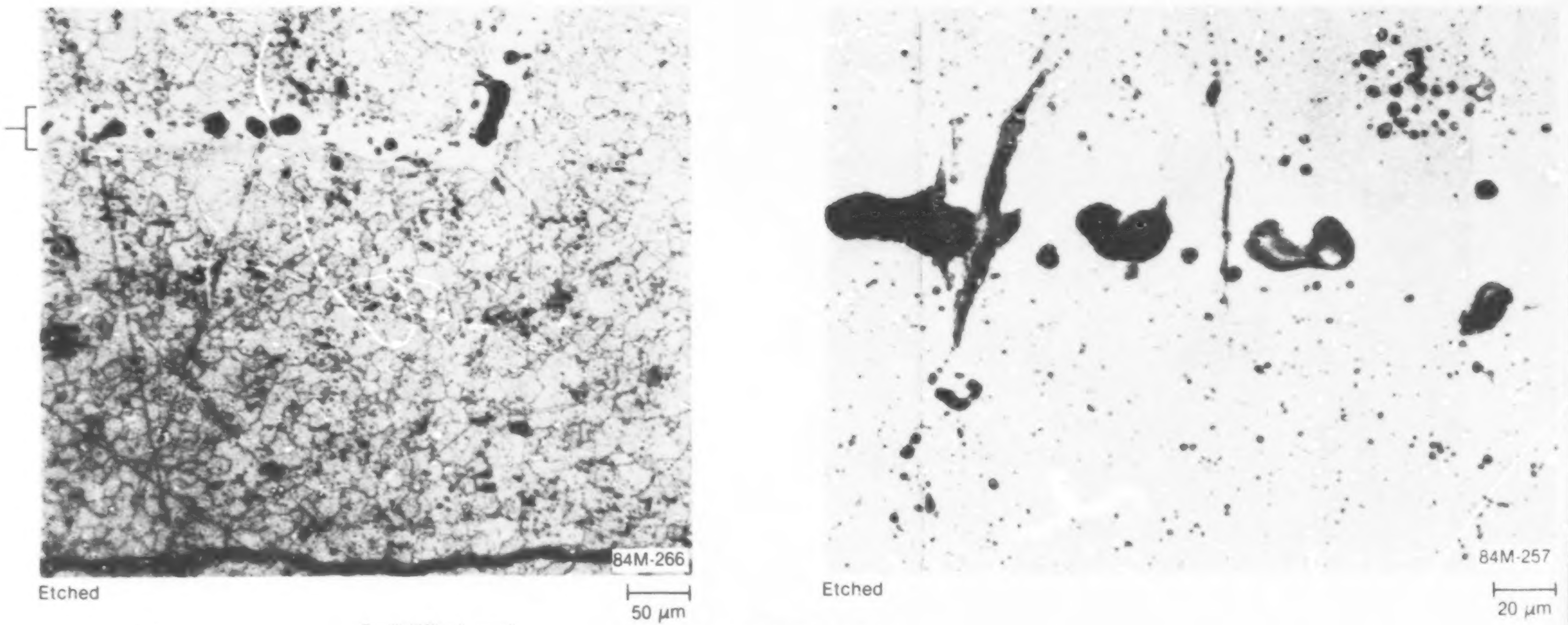
Etched
84M-266
50 μm
Etched
84M-257
20 μm

(b) and (c) Details of (a)

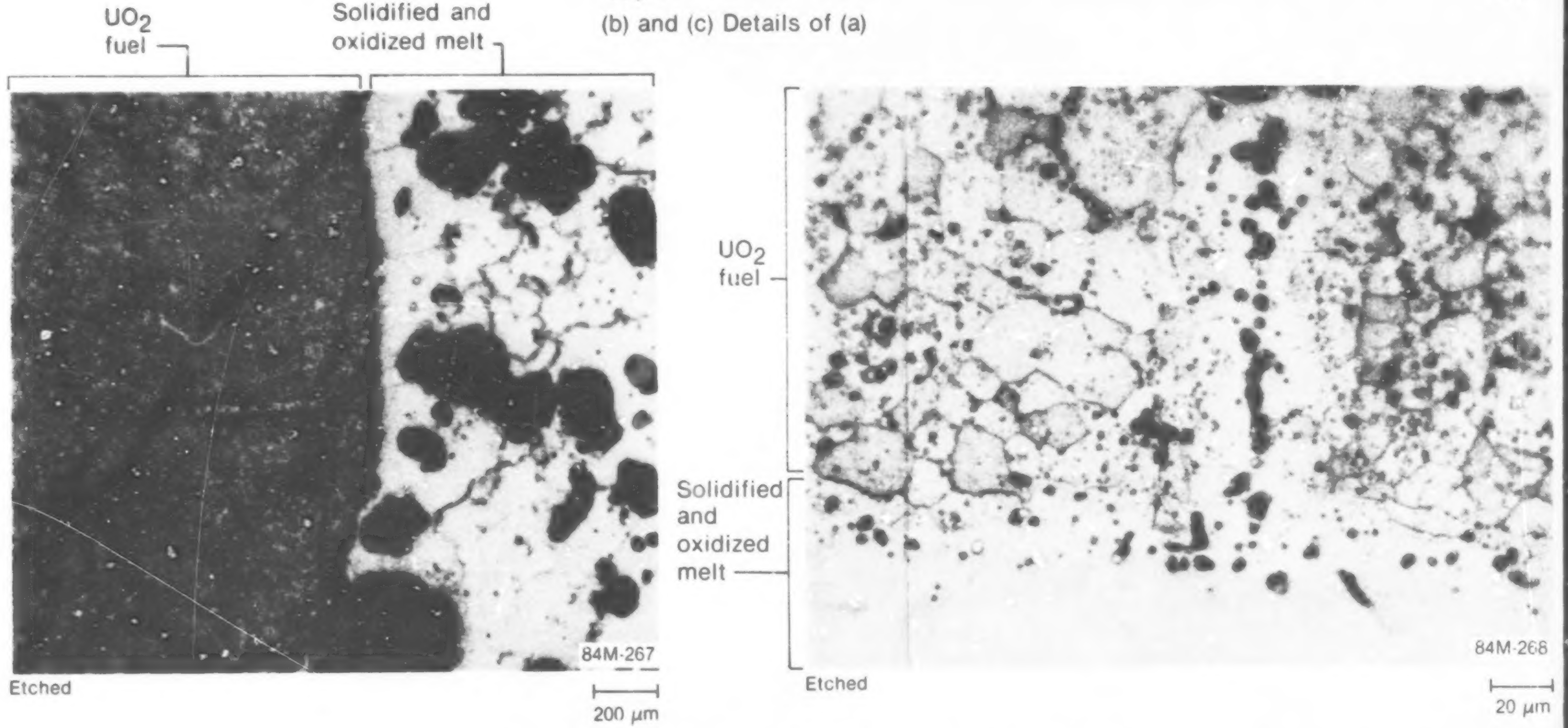
UO2 fuel
Solidified and oxidized melt
Etched
84M-267
200 μm
UO2 fuel
Solidified and oxidized melt
Etched
84M-268
20 μm

(d) and (e) Details of (a) showing the ceramic melt-pellet interface

4 2054

Figure 45. Cracks in the UO_2 pellet filled with a ceramic material. This ceramic was probably a formerly metallic (U,Zr,O) melt which penetrated into the cracks (see Figure 42) before it was oxidized to $(U,Zr)O_2$ (Rod 5B, 180°, at the 0.245-m cross-section elevation).

the 0.245-m cross-section elevation (Figure 6). Also, with respect to the ceramic material within the UO_2 cracks, it is not clear if the previously metallic (U,Zr,O) melt was oxidized due to interactions with fuel or steam. The pronounced pore formation within the material in the UO_2 cracks may indicate that the previously metallic melt solidified and was oxidized later in time.

The figures also show a homogeneous UO_2 grain structure over the whole pellet cross section with many small pores, preferentially along the grain boundaries, and some second-phase precipitations within the grains (Figure 45e). The melt/fuel interface (Figure 45d) shows chemical attack between the melt and the fuel. Thus, there exists a strong possibility that the ceramic material around the pellet of Rod 5B, and also across the whole blocked bundle cross section, was once molten. This is indicated by the strong pore formation in the solidified material (Figures 6 and 45d), but it cannot be decided if the ceramic material was initially metallic.

Figure 46 shows, in great detail, the typical appearance of the ceramic material of the 0.245-m cross-section elevation in contact with a UO_2 pellet. The UO_2 was not molten, but it interacted chemically with the melt. Also, the metallic inclusions in the ceramic material were molten. Other regions showed an onset of fuel disintegration, as in Figure 47, similar to that of out-of-pile molten zircaloy/solid UO_2 interaction experiments.[1,7] This again raises the question as to whether or not the ceramic material was initially metallic. The disintegration of the solid fuel may have been caused by a metallic (U,Zr,0) melt. However, in a previously metallic melt one would not expect metallic inclusions of the shape and size shown in Figures 46 and 47. Only the assumption that the previously metallic melt was oxidized, beside oxidation-resistant elements like nickel, rhenium, rhodium, molybdenum, and tungsten, with a subsequent temperature increase up to the melting point of the ceramic material, might result in a structure similar to the ceramic material.

The fuel pellet of Rod 4B at the 0.245-m cross-section elevation in contact with ceramic material shows a great amount of porosity along the UO_2 grain boundaries (Figure 48). At a higher magnification, another phase can be recognized within the grain-boundary pores (Figure 48c). In out-of-pile experiments,[7] a similar microstructure of partly disintegrated solid UO_2 fuel due to chemical interactions with molten zircaloy was observed. In that case, the pores were formed during sample preparation because of uranium metal pullout. The UO_2 is reduced by the zircaloy to hypostoichiometric UO_{2-x}. If the fuel is reduced below the $UO_{2-x}/(UO_{2-x} + U)$ phase boundary, metallic uranium (liquid above 1403 K) is present in addition to the UO_{2-x} (Figure 49)[2] and forms preferentially along the grain boundaries. If a specific amount of uranium in the UO_{2-x} structure is exceeded, then the solid structure disintegrates.[7] When the UO_{2-x} is cooled down, additional metallic uranium forms in the fuel, since the hypostoichiometric UO_{2-x} decomposes into stoichiometric $UO_{2.00}$ and metallic uranium (Figure 49). The uranium pulls out very easily from the UO_2 during preparation, and pores remain similar to those shown in Figure 48. If the metallic uranium stays in the UO_2 matrix, it will be oxidized very quickly to UO_2 on its surface, even at room temperature, and can no longer be distinguished from the fuel in the photographs. The small particles that can be seen in some of the pores (Figure 48c) may be oxidized uranium that formed due to the metallic (U,Zr,O) melt/solid fuel interaction described above.

The strong chemical attack of the (U,Zr,O) on the solid UO_2 melt and partial disintegration of the fuel are shown in Figure 50. The melt also penetrated along rather broad cracks (≅400 μm) into the UO_2 pellet. At all melt/UO_2 interfaces, the UO_2 dissolution process can be recognized (Figures 50c and 50d) to different extents. The strongest disintegration and subsequent dissolution of UO_2 is shown in Figure 50a at the pellet surface/melt interface, where fuel grains and small fuel fragments are dispersed in the melt. The solidified melt looks ceramic and consists of at least three different phases, plus small metallic inclusions (probably TC remnants). The light gray matrix phase (Figures 50b, c, e) may be $Zr0_2$ containing some uranium and the darker phase may be a $(U,Zr)O_2$ solid solution with higher uranium content. The two-phase appearance of the darker phase could be caused by oxidation products of the formerly decomposed metallic (U,Zr) alloy. Figure 51[2] shows the binary uranium-zirconium phase diagram. At higher temperatures, up to the solidus line, uranium and zirconium are completely miscible (isomorphous system). At lower temperatures (<1136 K), the solid solution decomposes, depending on its composition, into either α-Zr(O) + δ, δ, or δ + α-uranium. The δ phase contains about 50 wt% uranium. In general, one would assume that this type of microstructure was created by the previously metallic (U,Zr,O) melt solidifying before it was oxidized. [At least the

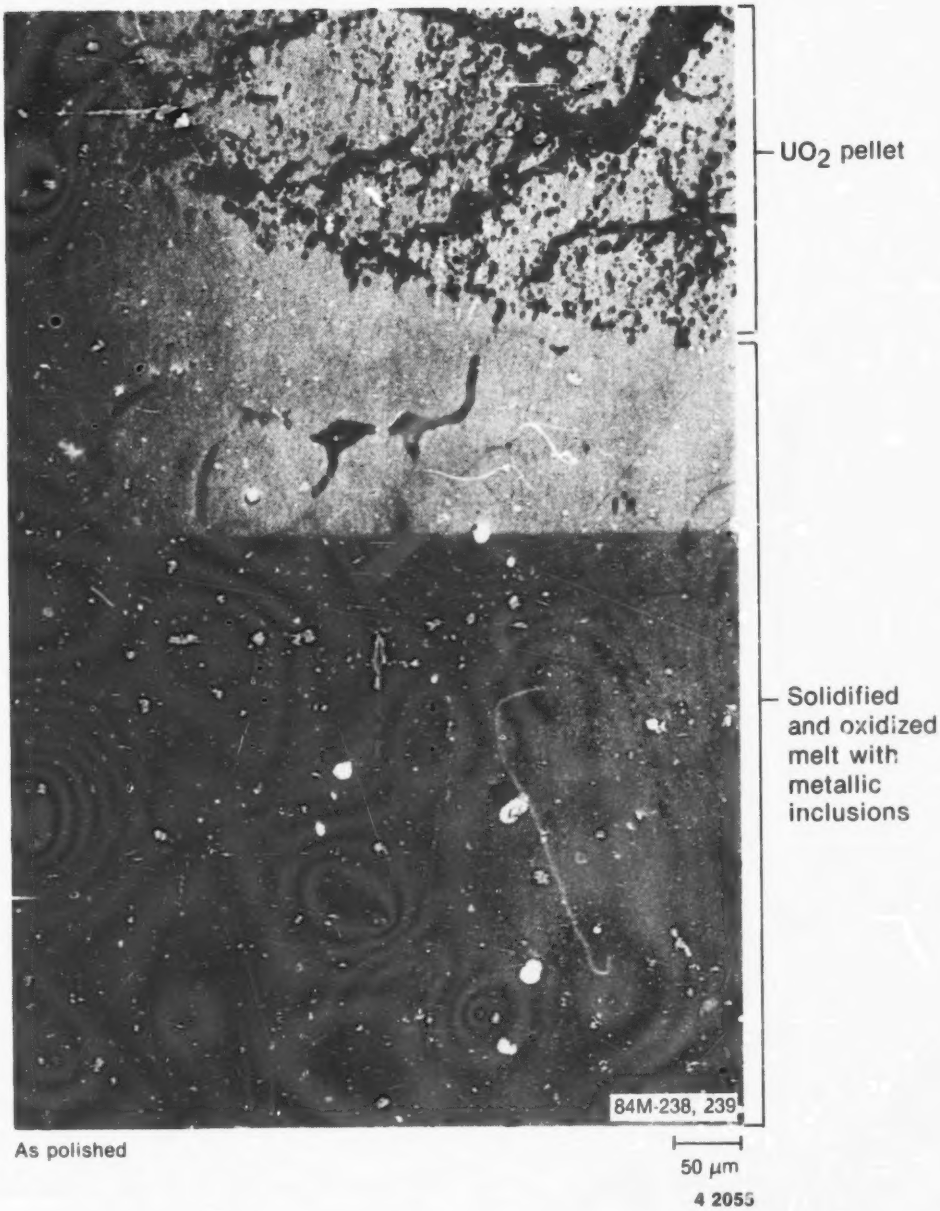
UO2 pellet
Solidified and oxidized melt with metallic inclusions
84M-238, 239
As polished
50 μm
4 2055

Figure 46. Solidified material in contact with UO_2 fuel pellet (Rod 4F, 90°, at the 0.245-m cross-section elevation). Note the small metallic inclusions in the two-phase ceramic matrix material which was probably a formerly metallic melt.

BEST COPY AVAILABLE

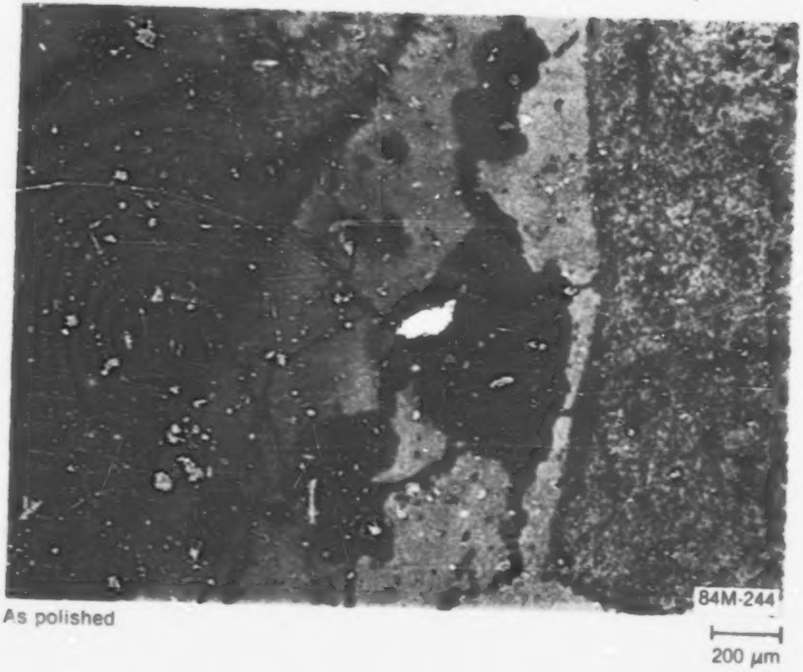
84M-244
200 μm

As polished

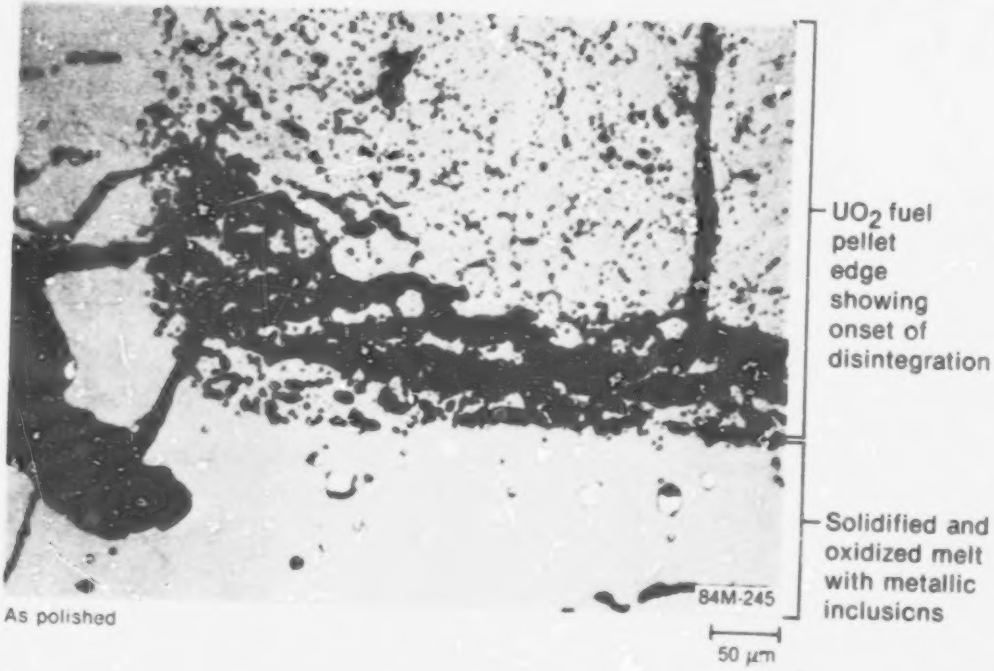
84M-245
50 μm
UO2 fuel pellet edge showing onset of disintegration
Solidified and oxidized melt with metallic inclusions
4 2058

As polished

Figure 47. Ceramic material, which was probably a formerly metallic melt, in contact with UO_2 fuel pellet at its circumference and within large cracks (Rod 3E, 80°, at the 0.245-m cross-section elevation).

BEST COPY AVAILABLE

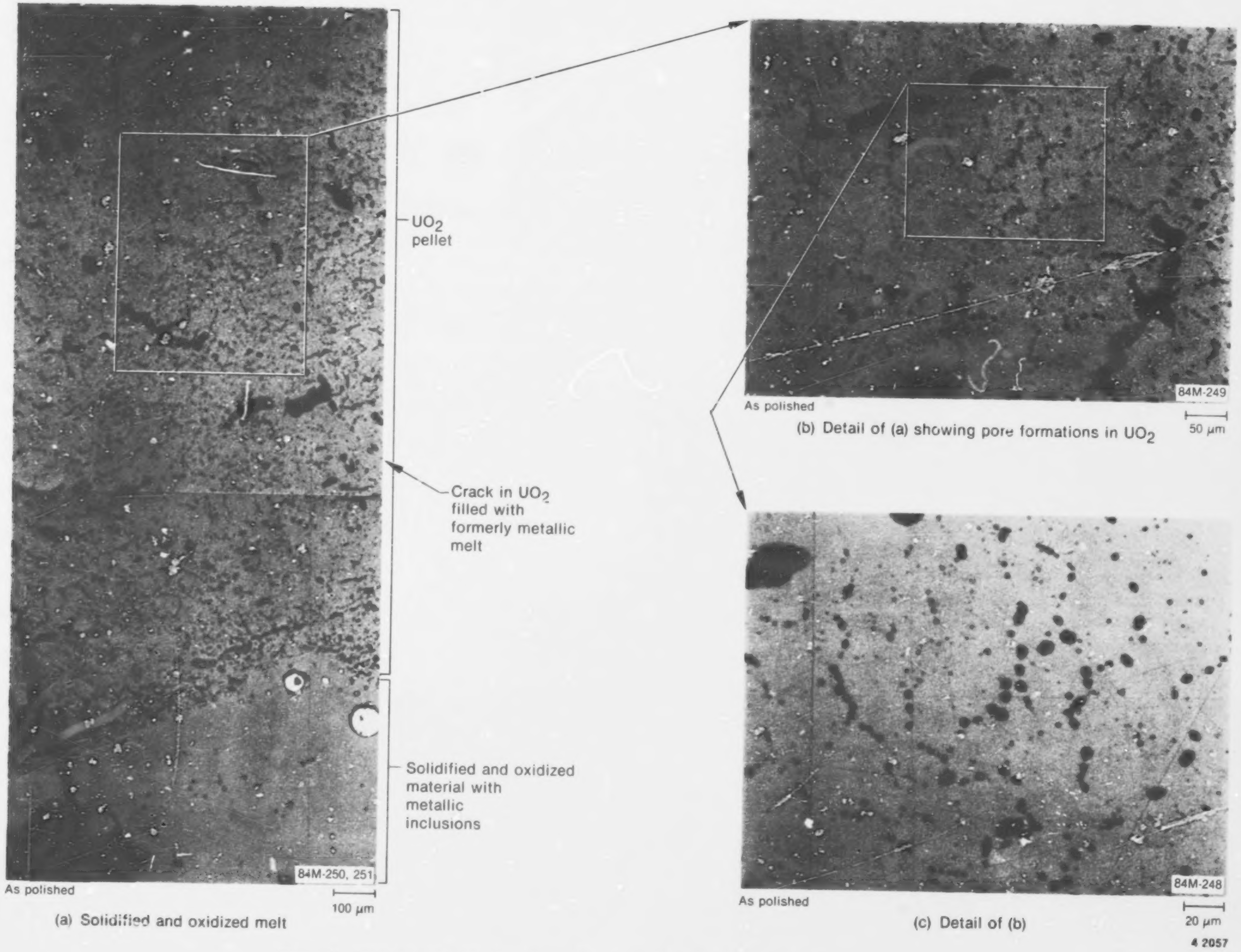
UO$_2$ pellet
Crack in UO$_2$ filled with formerly metallic melt
Solidified and oxidized material with metallic inclusions
84M-250, 251
As polished
100 µm
84M-249
As polished
50 µm
84M-248
As polished
20 µm
4 2057

(a) Solidified and oxidized melt

(b) Detail of (a) showing pore formations in UO$_2$

(c) Detail of (b)

Figure 48. Solidified and oxidized melt in contact with a UO$_2$ pellet, showing strong pore formation within the fuel, preferentially along grain boundaries. In some of the small pores, another phase is present (Rod 4B, 135°, at the 0.245-m cross-section elevation).

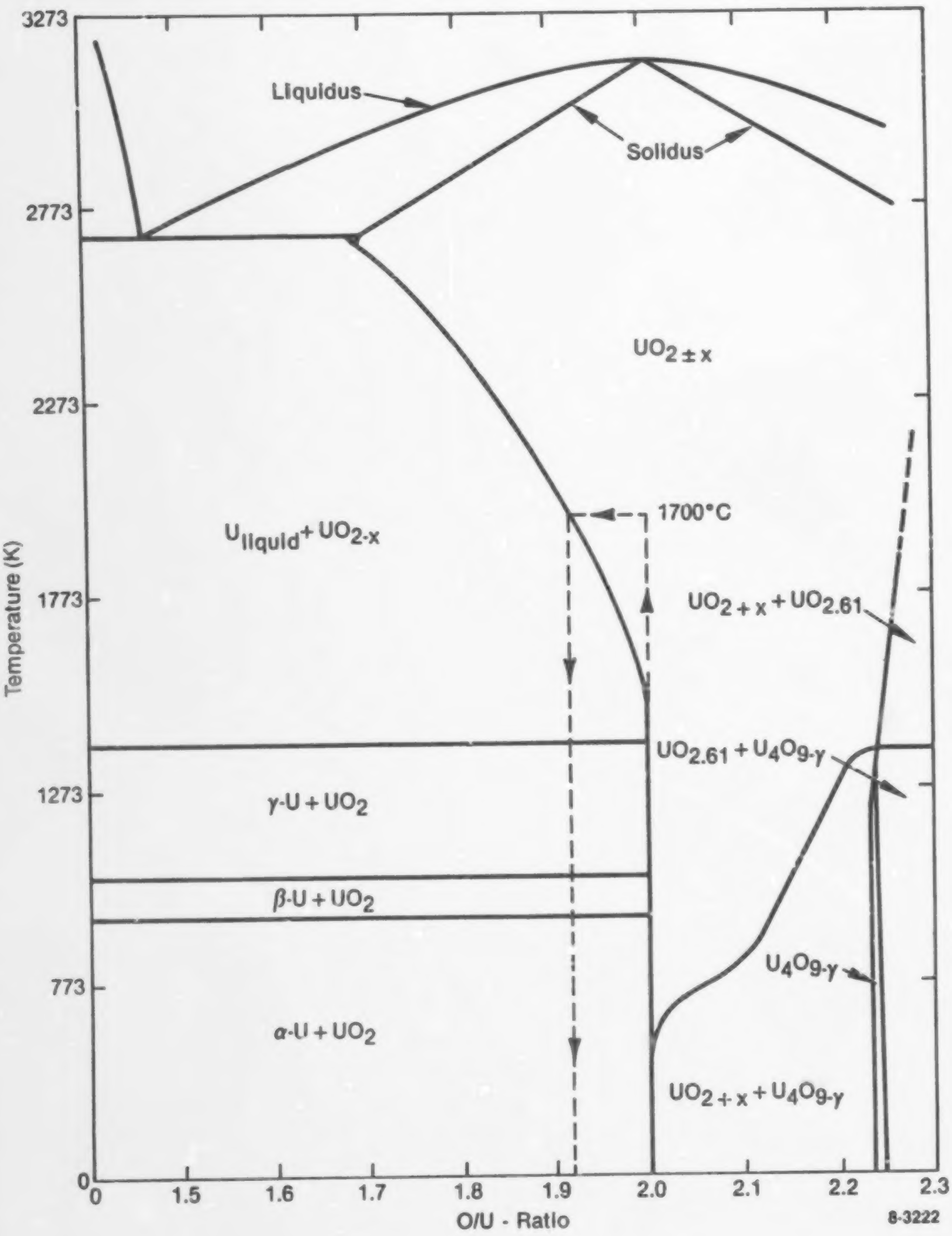

Figure 49. Detail of the uranium-oxygen phase diagram, from Reference 2.

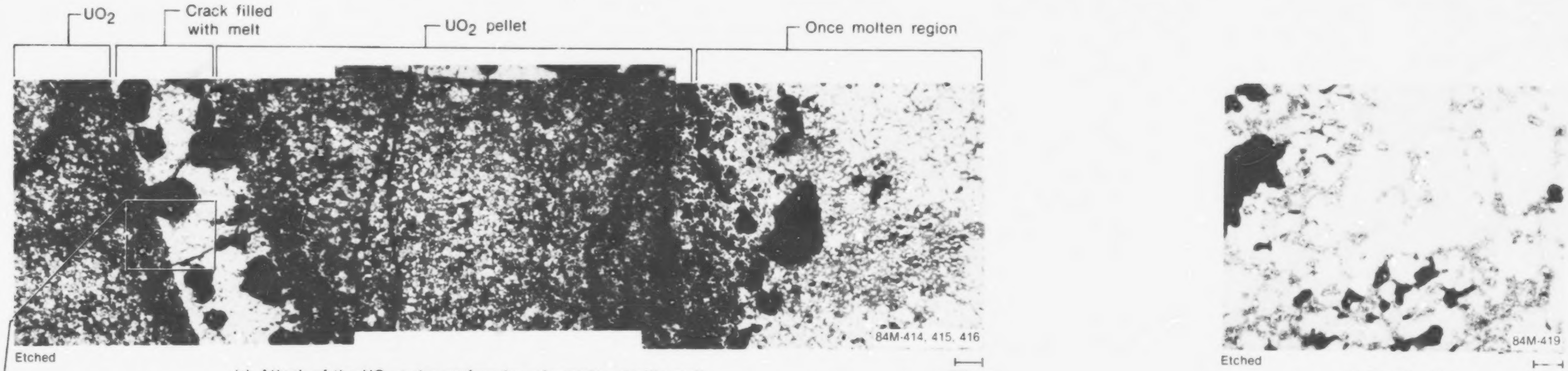

UO2
Crack filled with melt
UO2 pellet
Once molten region
84M-414, 415, 416
Etched
200 μm
84M-419
Etched
50 μm

(a) Attack of the UO_2 outer surface by a formerly metallic melt

(b) Detail of (a) melt

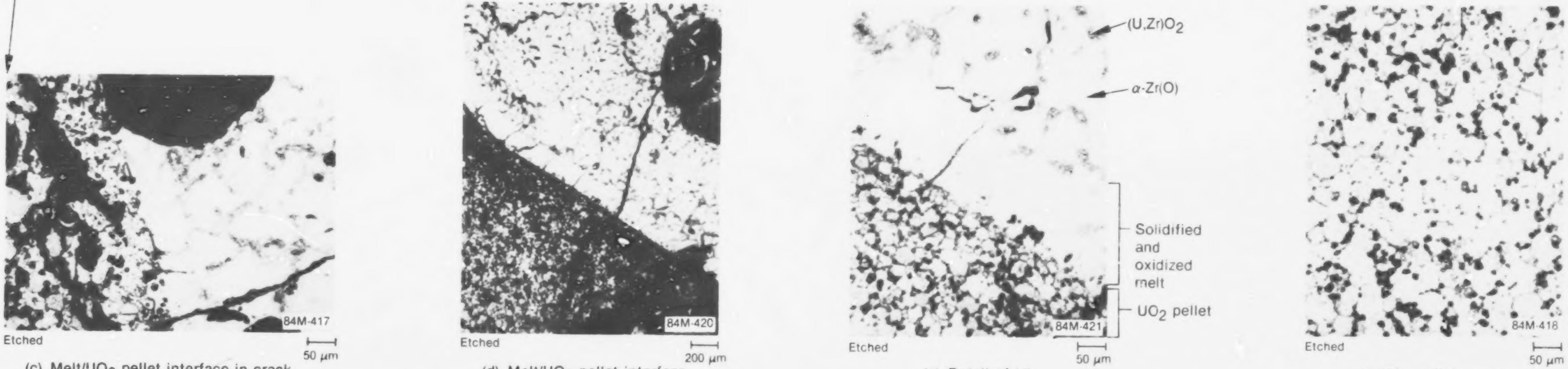

84M-417
Etched
50 μm
84M-420
Etched
200 μm
(U,Zr)O2
α-Zr(O)
Solidified and oxidized melt
UO2 pellet
84M-421
Etched
50 μm
84M-418
Etched
50 μm

(c) Melt/UO_2 pellet interface in crack

(d) Melt/UO_2 pellet interface

(e) Detail of (d)

(f) UO_2 pellet center

4 2059

Figure 50. Attack of the UO_2 outer surface by a formerly metallic (U,Zr,O) melt, as well as penetration of the melt into UO_2 cracks before it was oxidized by steam (Rod 6E, 180°, at the 0.27-m cross-section elevation).

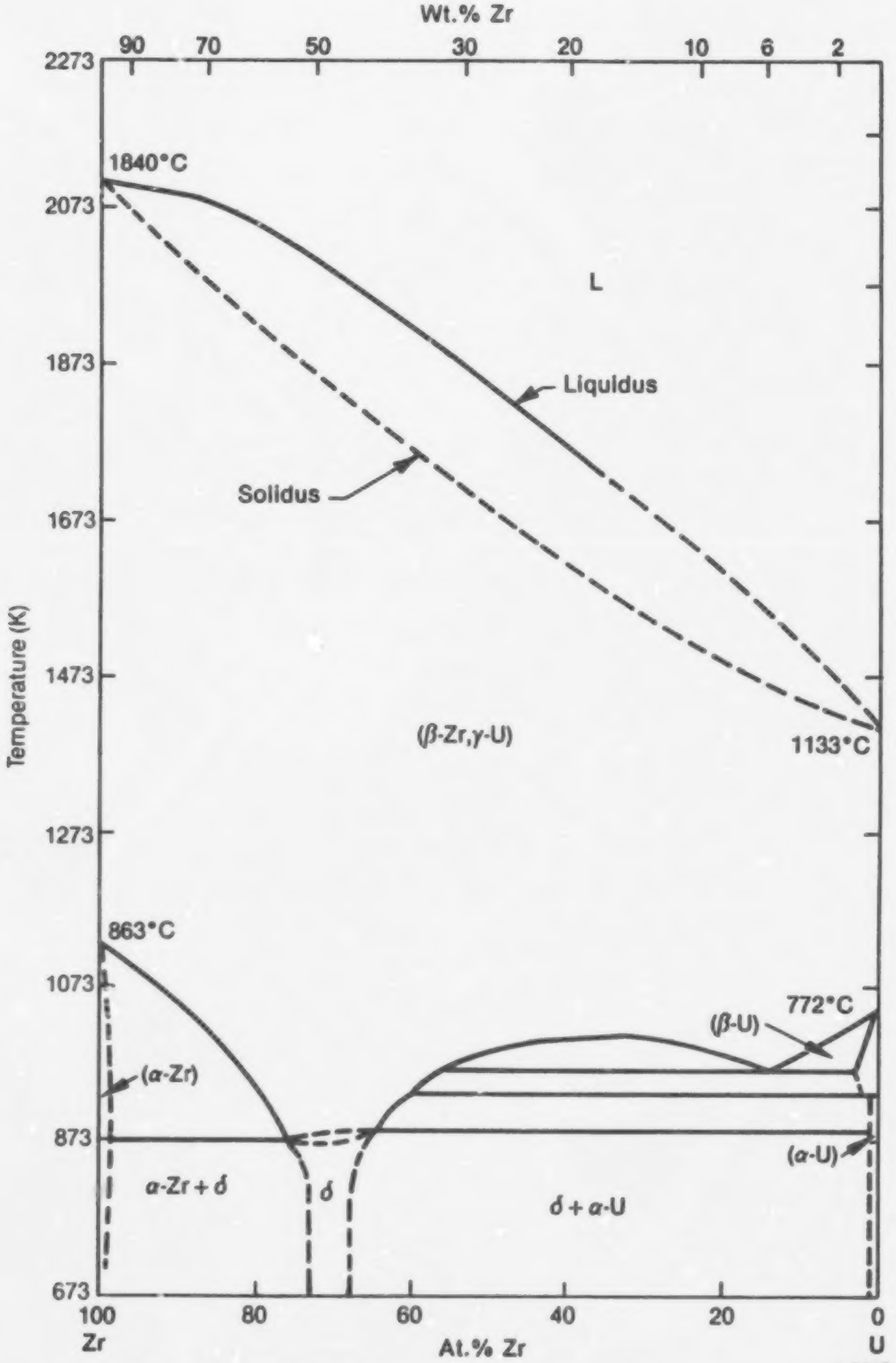

D. Summers - Smith (1954)
A. N. Holden, W. E. Seymour (1956)

Figure 51. Uranium-zirconium phase diagram, from Reference 2.

α-Zr(O) should have been solidified before oxidation, due to the much higher melting point.] If the melt is oxidized at temperature, one would expect a more homogeneous oxidation product. The melt oxidizes until it solidifies into $(U,Zr)O_2$ solution.

Evidence for the speculation that the ceramic-looking material may have been a previously solidified (U,Zr,O) melt which was later oxidized is shown in Figure 52. One can recognize the initially oxidized cladding with its typical columnar grain structure. The ZrO_2 shell was in contact with melts both on the outside and inside. The melt between the oxidized cladding and the fuel partially caused a strong pellet disintegration, resulting in UO_2 liquefaction. Then the metallic melt was solidified, forming pores of various sizes, and was oxidized later by steam. If the ceramic material was liquid during the transient, the ZrO_2 cladding shell should also have been molten or attacked in a different (stronger) way than shown in Figure 52a. The melt penetrated up to the pellet center, and the matrix looks single-phase (Figure 52c). Parts of the melt show a structure where even individual grains are visible. This type of structure apparently formed only in the pellet center.

Figure 53 shows a solidified melt in a pellet void which looks like the dished volume at the pellet interfaces (same cross section as Figure 52). Typical melt formations at other cross-section elevations are shown in the following figures. Figure 54 shows the central part of a formerly partially molten fuel pellet. The onset of UO_2 melting resulted in a very porous (foam-like) microstructure. The microstructure of the matrix is single-phase and reveals no visible structure (as-polished). The conclusion that the UO_2 was molten means that very high temperatures (≥ 3123 K) were reached locally within the bundle for a very short time. The 0.915-m cross-section elevation (Figure 11) shows a few UO_2 pellets which look less dense than the other pellets (for example, Rods 2E, 4E, 1D, 2D, 5D, 6D, and 6C), even at this low magnification. In all these cases, the cladding is either gone or is completely oxidized. Apparently no fuel melt runoff occurred. Figure 55 shows the transition regions from the porous, previously molten UO_2 pellet to the as-fabricated fuel structure at the same cross-section elevation. A densified zone, showing no structure but small pores, lies between the two regions. Figure 56 shows solidified ceramic material at the 0.145-m cross-section elevation with small (≤ 10 μm) metallic inclusions. The ceramic matrix seems to be single-phase. The metallic inclusions appear multiphase, according to the etched structure, and may consist of oxidation-resistant TC or Inconel alloying elements. There are many other regions where the ceramic material looks similar to that in Figure 56, with various amounts of metallic inclusions. Sometimes the ceramic looks two-phase, with a very small amount of a second, barely noticeable, ceramic phase along grain boundaries. Figure 57 shows strongly deformed (ballooned) cladding tubes which touched each other and were later completely oxidized. Later in the transient, the oxidized cladding and the fuel were attacked (dissolved) to different extents by an initially metallic (U,Zr,O) melt. In Figure 57, one recognizes the oxidized melt within the fuel/cladding gap and on the oxidized cladding OD. Other regions exist at the same cross-section elevation where the oxidized cladding was completely dissolved by the previously metallic melt.

There is one region with unusual ceramic phase formations which was observed only at the 0.145-m cross-section elevation (Figure 58). It is located between (or near) Rod 6E and the zircaloy liner (Figure 12), where one of the temperature-profile detectors was mounted in the fuel rod bundle (one at 135° and the other at the 315° orientation). The detectors were housed in an alumina (Al_2O_3) tube. The Al_2O_3 tube (melting point $\simeq 2323$ K) may be the reason for chemical interaction with UO_2, ZrO_2, or $(U,Zr)O_2$, resulting in the eutectic microstructure shown in Figure 58. This microstructure is typical of solidified multicomponent compounds with different melting points forming phases on cooldown. The primary constituent could be UO_2 or a $(U,Zr)O_2$ compound, with melting points above $\simeq 2873$ K, and the secondary constituent (which may also be called the eutectic constituent) could be mainly an Al_2O_3/UO_2 or an Al_2O_3 mixture, with a melting point of about 2173 K or lower. UO_2 and Al_2O_3 form a eutectic system. The eutectic point is located at the chemical composition of about 75 mol% Al_2O_3, and the eutectic temperature is about 2173 K. The eutectic point of the ZrO_2/Al_2O_3 system is located at the chemical composition of about 40 wt% Al_2O_3, with a eutectic temperature below 2173 K. The low-melting-point eutectic materials produced during the test apparently had a high vapor pressure, resulting in the large pore formation shown in Figure 58c. A subsequent examination in the same cross-section region revealed similar structures near the Al_2O_3 temperature profile detector with different amounts of the individual phases (Figure 59).

BEST COPY AVAILABLE

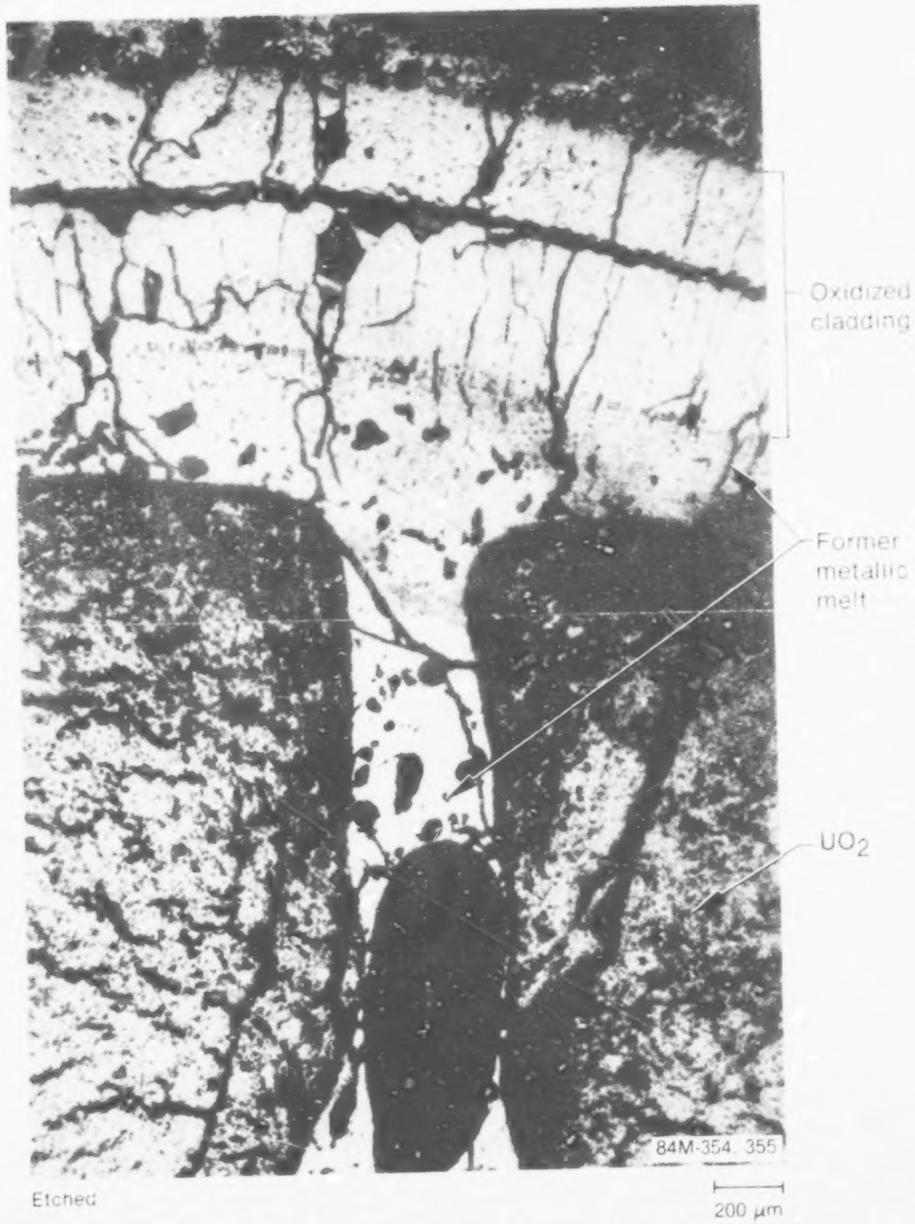
Oxidized cladding
Former metallic melt
UO$_2$
84M-354, 355
Etched
200 µm

(a) Melt penetration into the cracks of the UO$_2$ pellet

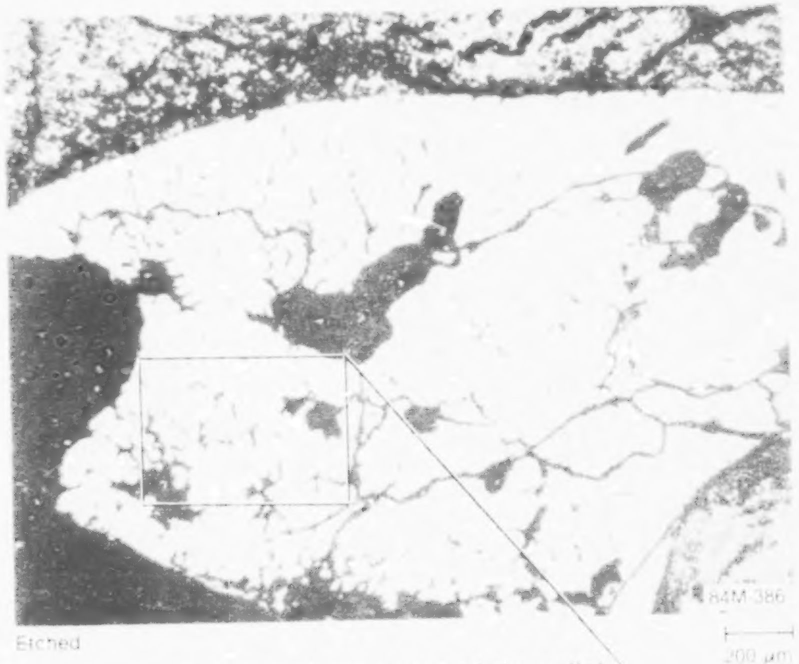
84M-386
Etched
200 µm

(b) Melt near the center of the pellet

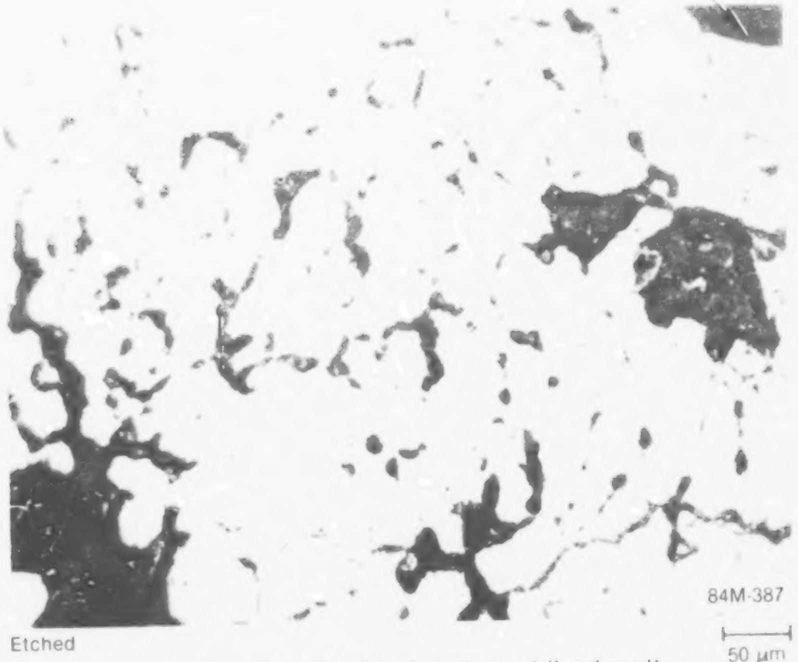
84M-387
Etched
50 µm

(c) Detail of (b) showing the oxidized melt

4 2061

Figure 52. Melt penetration into UO$_2$ pellet cracks (object number 4, 280°, at the 0.495-m cross-section elevation).

BEST COPY AVAILABLE

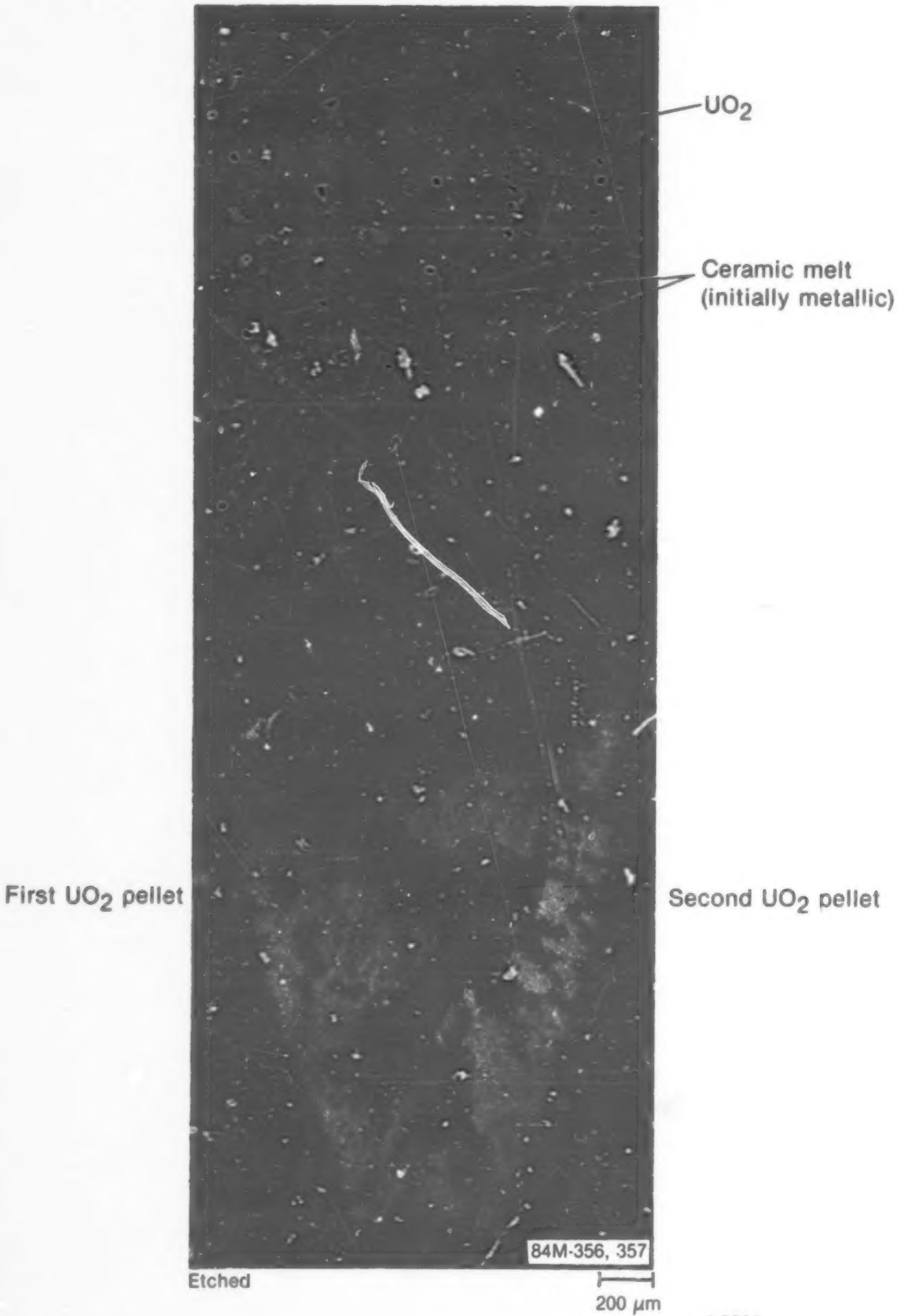
UO$_2$
Ceramic melt
(initially metallic)
First UO$_2$ pellet
Second UO$_2$ pellet
84M-356, 357
Etched
200 μm

4 2062

Figure 53. Melt penetration into UO$_2$ pellet interfaces (dishing volume) (object number 5 at the 0.495-m cross-section elevation).

BEST COPY AVAILABLE

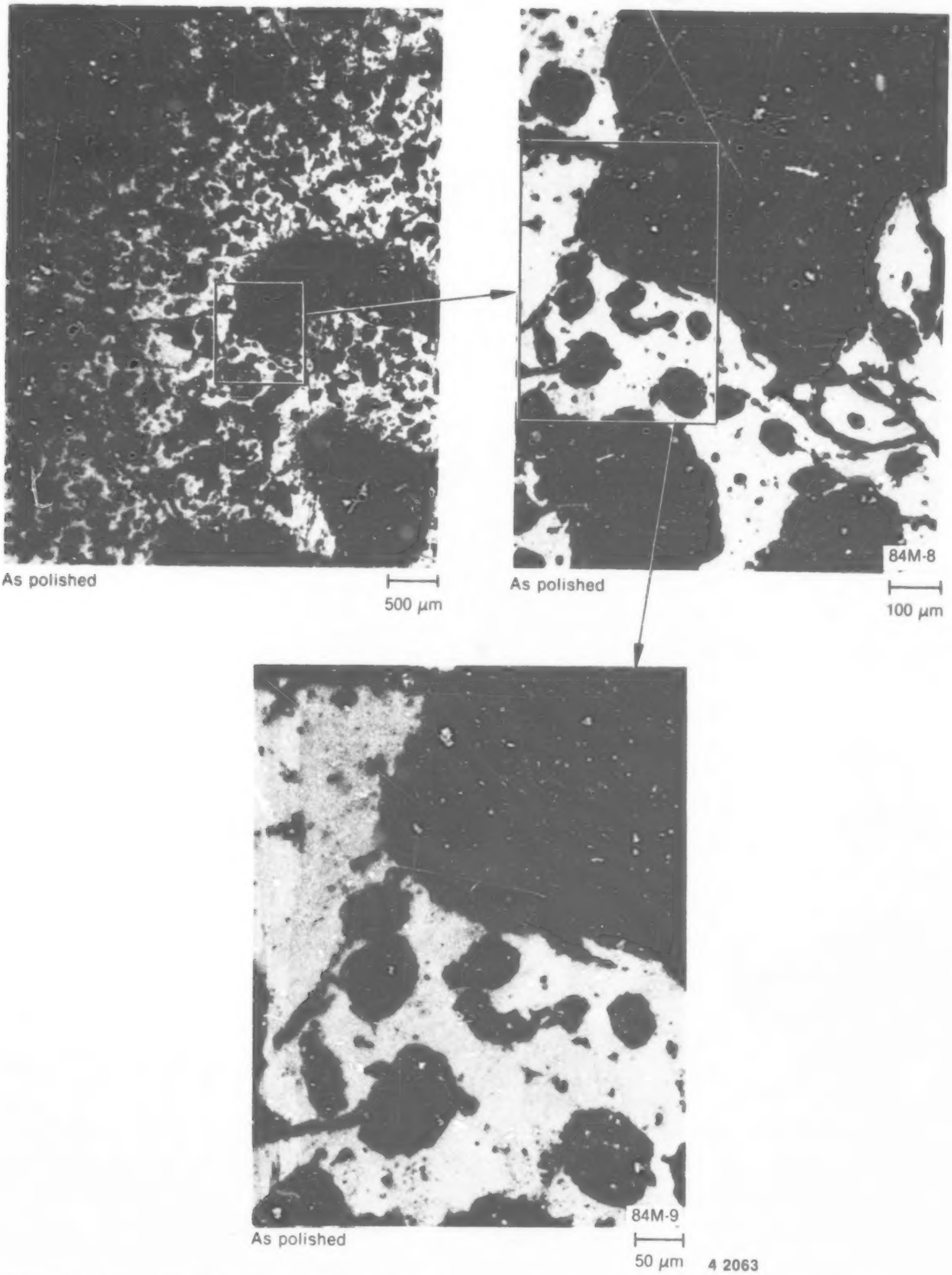
As polished
500 µm
As polished
84M-8
100 µm
As polished
84M-9
50 µm
4 2063

Figure 54. Onset of UO_2 fuel melting in pellet cracks (Rod 4E, at the 0.915-m cross-section elevation).

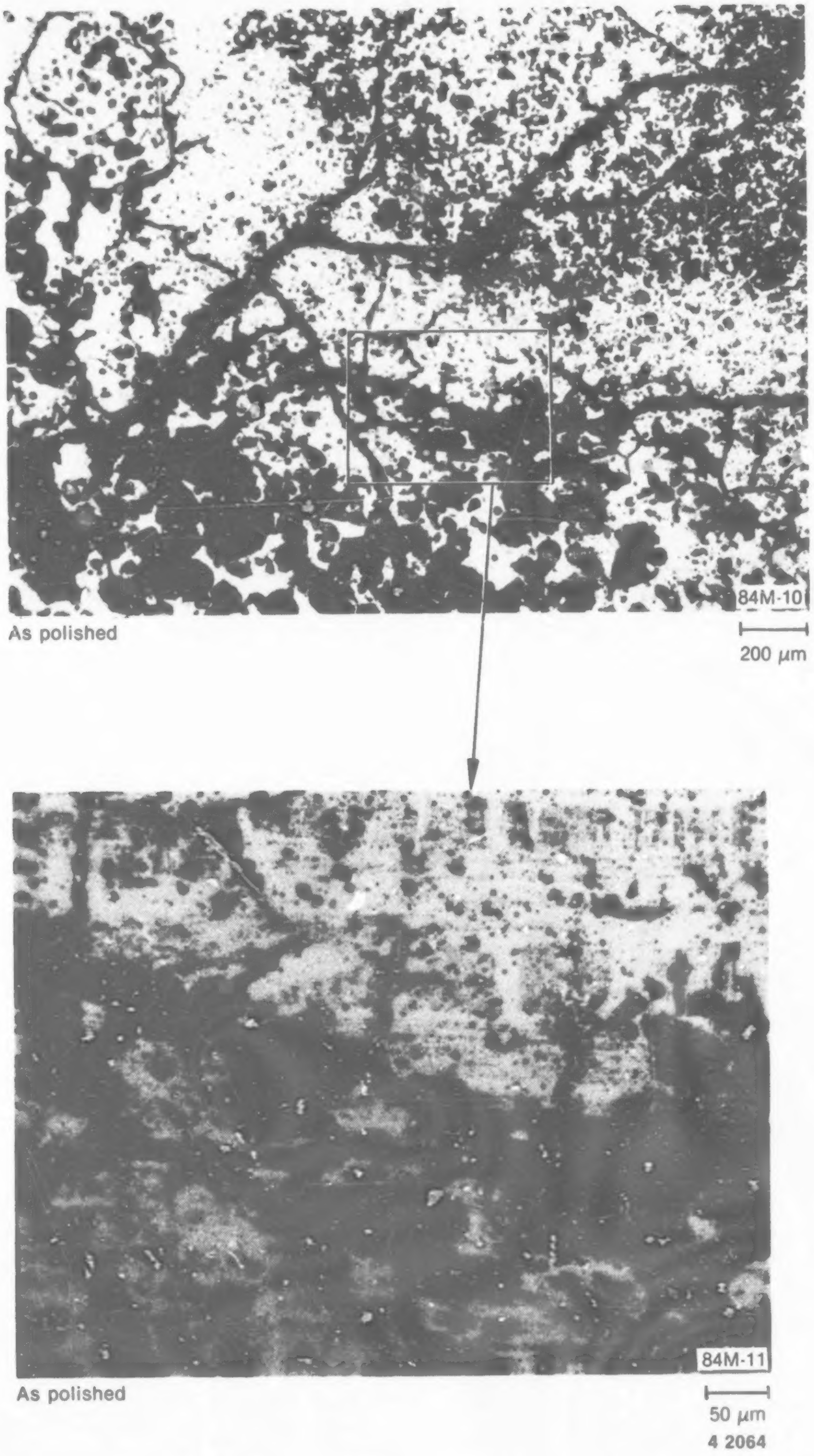
84M-10
As polished
200 μm
84M-11
As polished
50 μm
4 2064

Figure 55. Transition region from porous, previously molten UO_2 pellet to as-fabricated fuel structure with densified zone in between (Rod 2D, 0°, at the 0.915-m cross-section elevation).

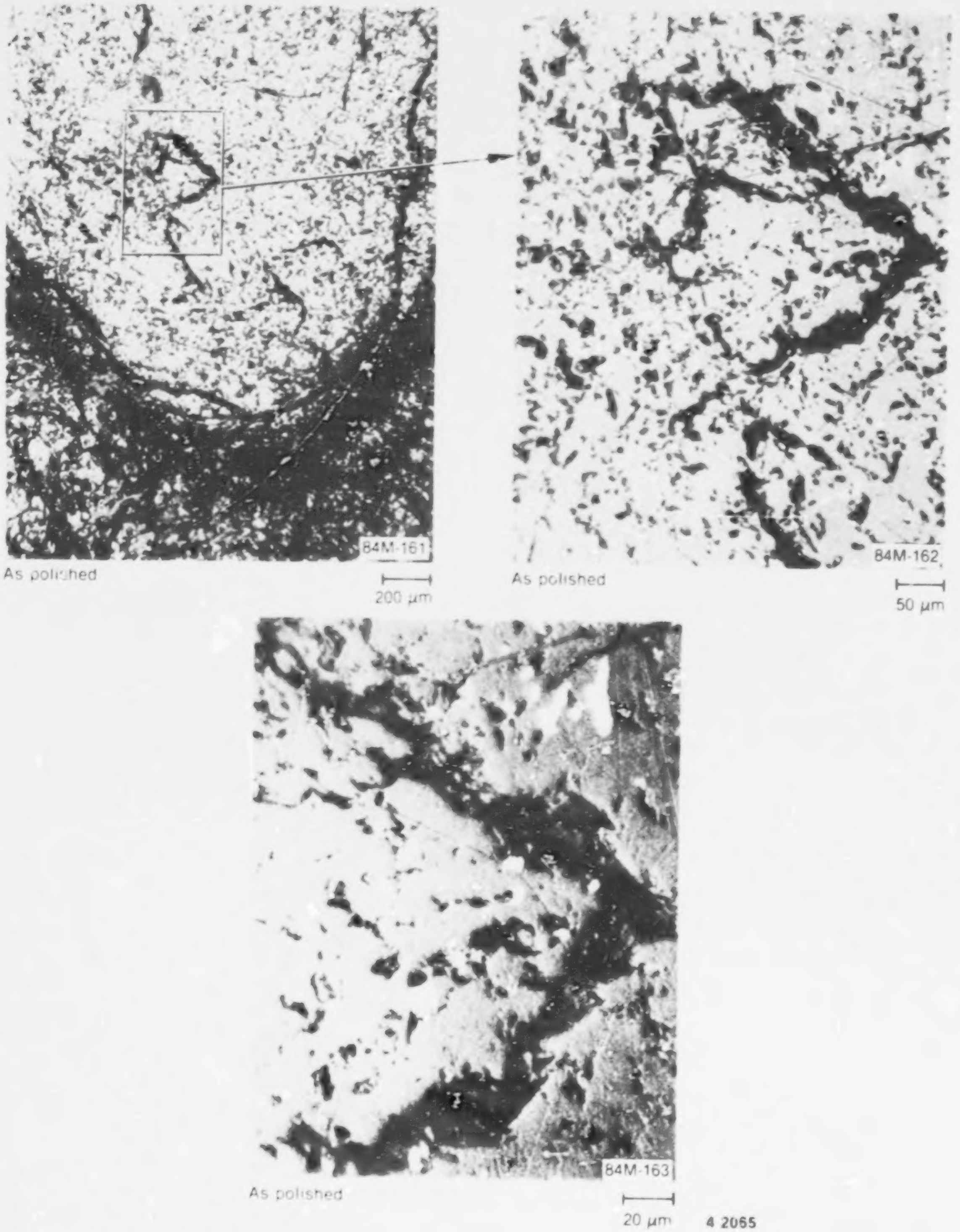
84M-161
As polished
200 µm
84M-162
As polished
50 µm
84M-163
As polished
20 µm
4 2065

Figure 56. Solidified ceramic material with small metallic inclusions (between Rods 4D, 5D, and 4E, 5E, at the 0.145-m cross-section elevation).

BEST COPY AVAILABLE

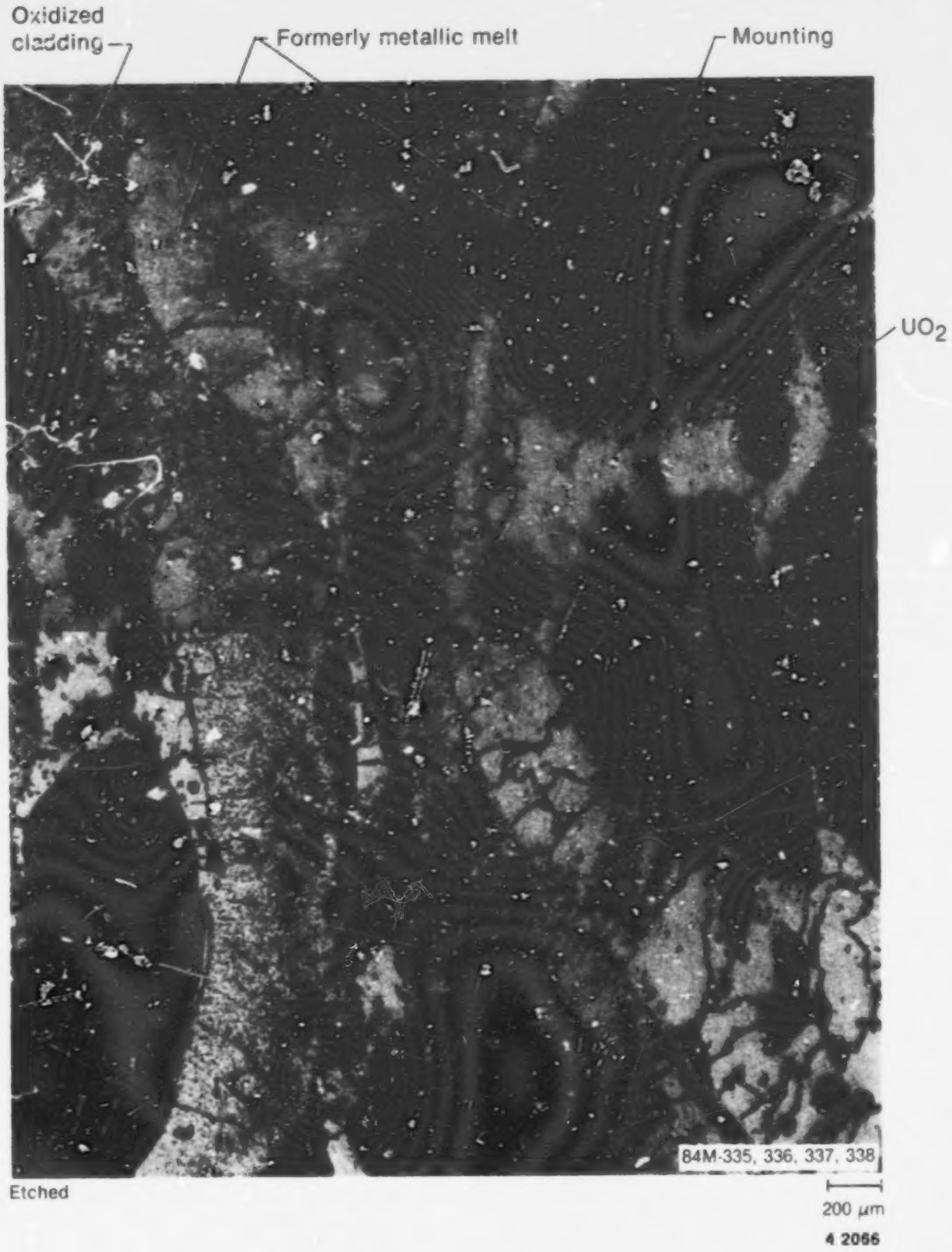
Oxidized cladding
Formerly metallic melt
Mounting
UO2
84M-335, 336, 337, 338
Etched
200 μm
4 2066

Figure 57. Ballooned cladding touching each other with subsequent oxidation. Melt attack occurred on the cladding OD and ID surfaces as well as the fuel surface (object number 1, 0°, at the 0.495-m cross-section elevation).

BEST COPY AVAILABLE

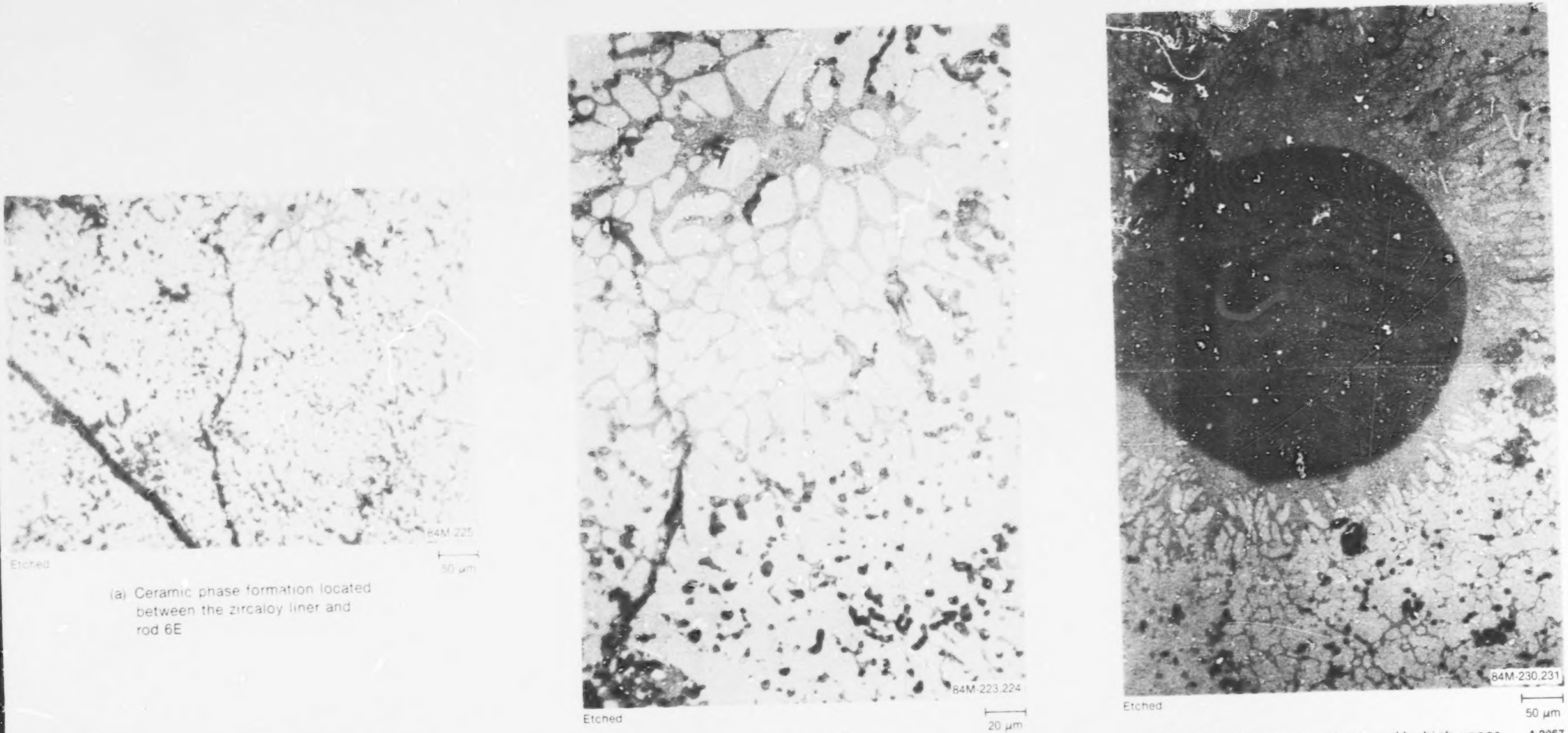
84M-225
Etched
50 μm
84M-223,224
Etched
20 μm
84M-230,231
Etched
50 μm
4 2067

(a) Ceramic phase formation located between the zircaloy liner and rod 6E

(b) Detail of (a)

(c) Pore formation apparently caused by high vapor pressure of the low-melting-point eutectic

Figure 58. Ceramic phase formation located between the zircaloy liner and Rod 6E at the 0.145-m cross-section elevation. This is a typical microstructure of a solidified multicomponent system, probably a eutectic chemical interaction between the Al_2O_3 temperature profile detector tube and UO_2 or $(U,Zr)O_2$.

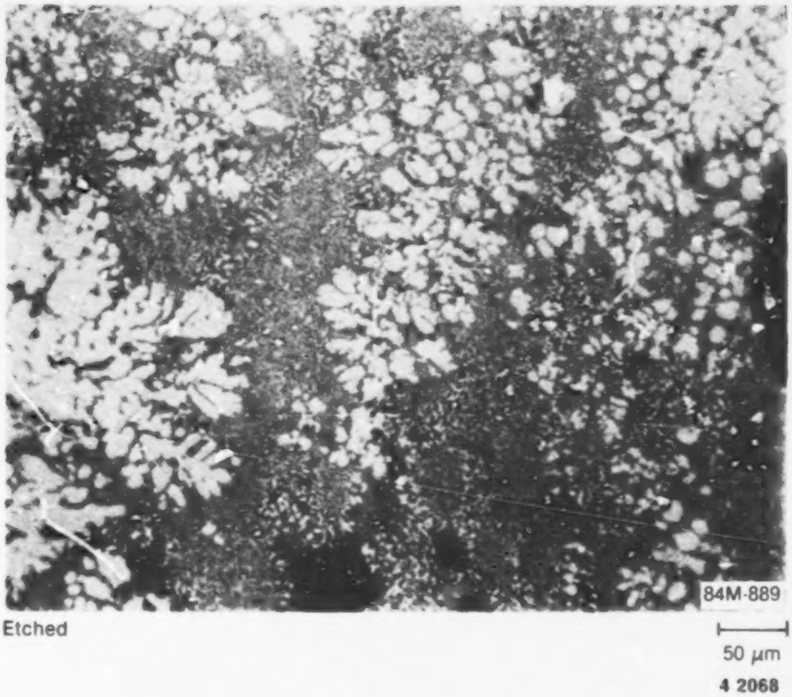

Figure 59. Microstructure in the same region as that of Figure 58.

Mechanical and Chemical Behavior of the Spacer Grids

There were three spacer grids (Inconel 718)[a] in the fuel-rod bundle. The upper two melted and/or reacted with other materials. Part of the oxidation-resistant components of the Inconel (high nickel) may be alloyed with TC material which was visible as metallic inclusions in the solidified ceramic melts (Figures 40, 41, 46, 47, 48, 49, 56). Only the lowest spacer grid in the bundle remained more or less intact or can be recognized in the metallographic cross section at the 0.055-m elevation (Figure 3). At various locations, limited chemical interactions occurred between the spacer grid and metallic and ceramic melt droplets which reached this cross-section elevation, resulting in localized destruction of the spacer grid (Figure 3).

The offsets of the spacer grid parts shown in Figure 60 are probably due to local melt contacts which resulted in severe temperature differences and shifting (bending) of the material. Figure 61 shows the metallographic appearance of previously molten zones of the spacer grid in contact with solidified ceramic material. At the low magnification, except for some localized surface oxidation, no additional phases in the previously molten Inconel can be recognized. The wetting behavior between the metallic melt and earlier solidified ceramic material is, as expected, poor.[10] The temperature reached in this region must have been above the melting point of Inconel 718 (≅1773 K) but below the melting point of zircaloy (≅2033 K), since no melting of the zircaloy cladding or the zircaloy liner occurred, although they also were in contact with the ceramic melt. Or, it could be that the heat transferred from the melt to the cladding and/or liner was removed more rapidly (due to thermal conductivity) than from the spacer grid, which has a smaller mass.

Figure 62 shows chemical interactions between a metallic melt and the spacer grid material. Probably due to this melt contact, the spacer grid melted and relocated. The microstructure of the chemical interaction region (Figure 62b and 62c) looks like that of the Inconel/zircaloy out-of-pile reference

---

[a] 53 wt% nickel, 19 wt% chromium, 18.4 wt% iron, 5.2 wt% tantalum, 3.5 wt% molybdenum, 0.5 wt% aluminum.

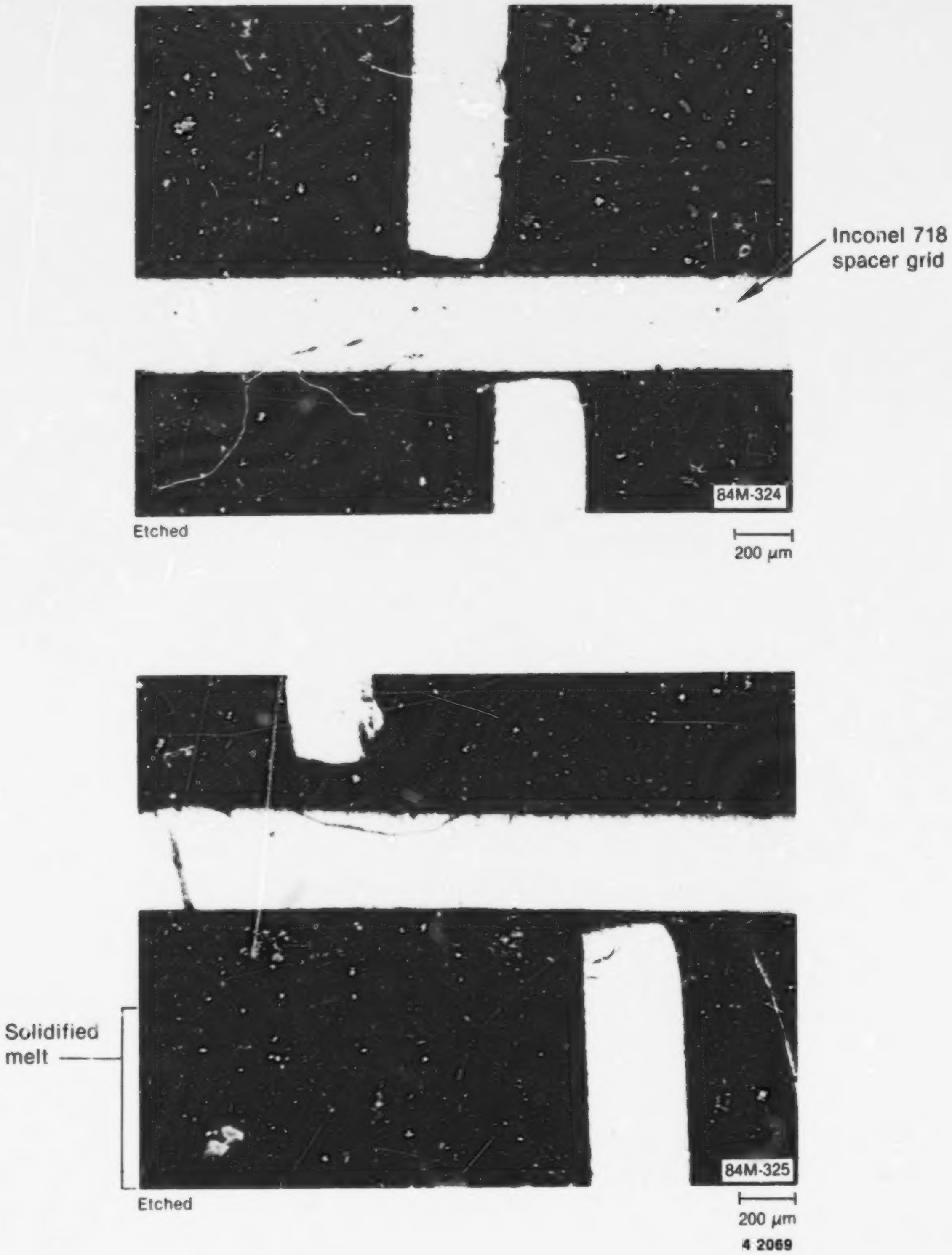
Inconel 718 spacer grid
84M-324
Etched
200 µm
Solidified melt
84M-325
Etched
200 µm
4 2069

Figure 60. Spacer grid junctions between Rods 4F and 5E (upper photograph) and Rods 5F and 6E (lower photograph) at the 0.055-m cross-section elevation.

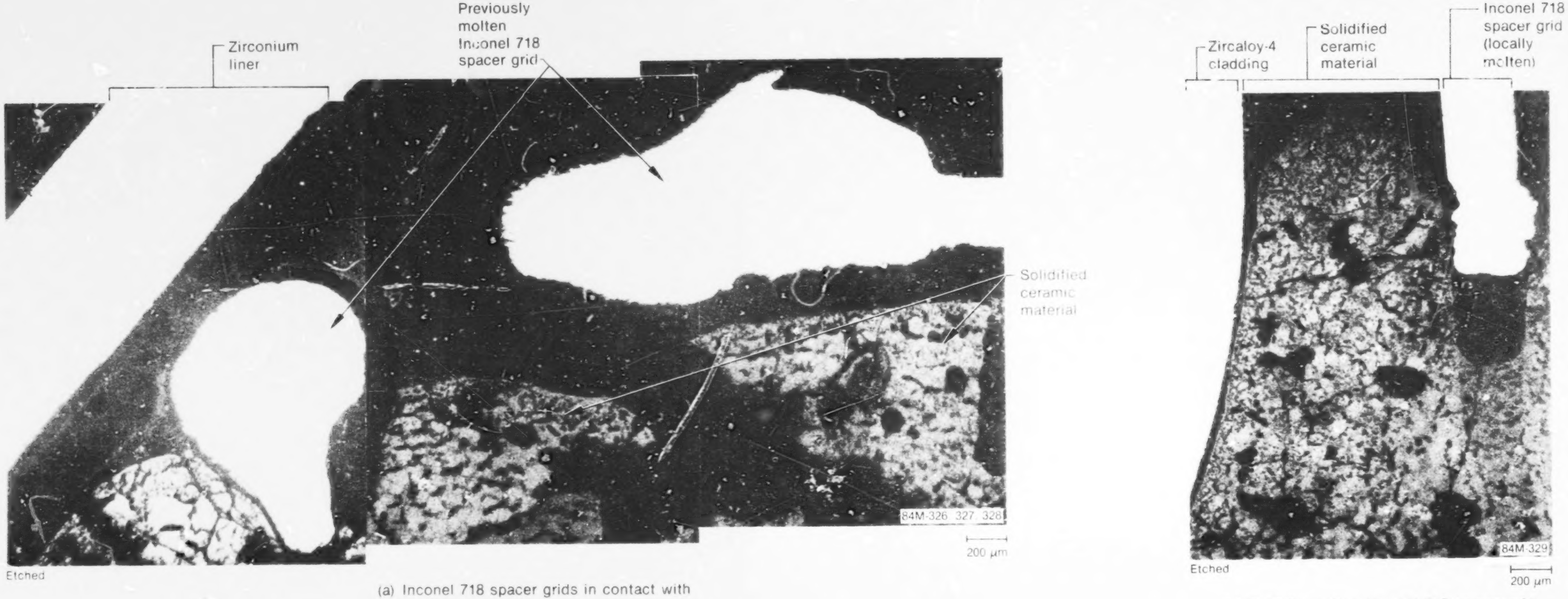
Zirconium liner
Previously molten Inconel 718 spacer grid
Solidified ceramic material
84M-326, 327, 328
200 µm
Etched
Zircaloy-4 cladding
Solidified ceramic material
Inconel 718 spacer grid (locally molten)
84M-329
Etched
200 µm

(a) Inconel 718 spacer grids in contact with solidified ceramic material

(b) Partially molten Inconel 718 spacer grid and intact zircaloy-4 cladding

4 2070

Figure 61. Metallographic appearance of the previously molten Inconel 718 spacer grids in contact with solidified ceramic material near Rod 6E, 135°, at the 0.055-m cross-section elevation.

BEST COPY AVAILABLE

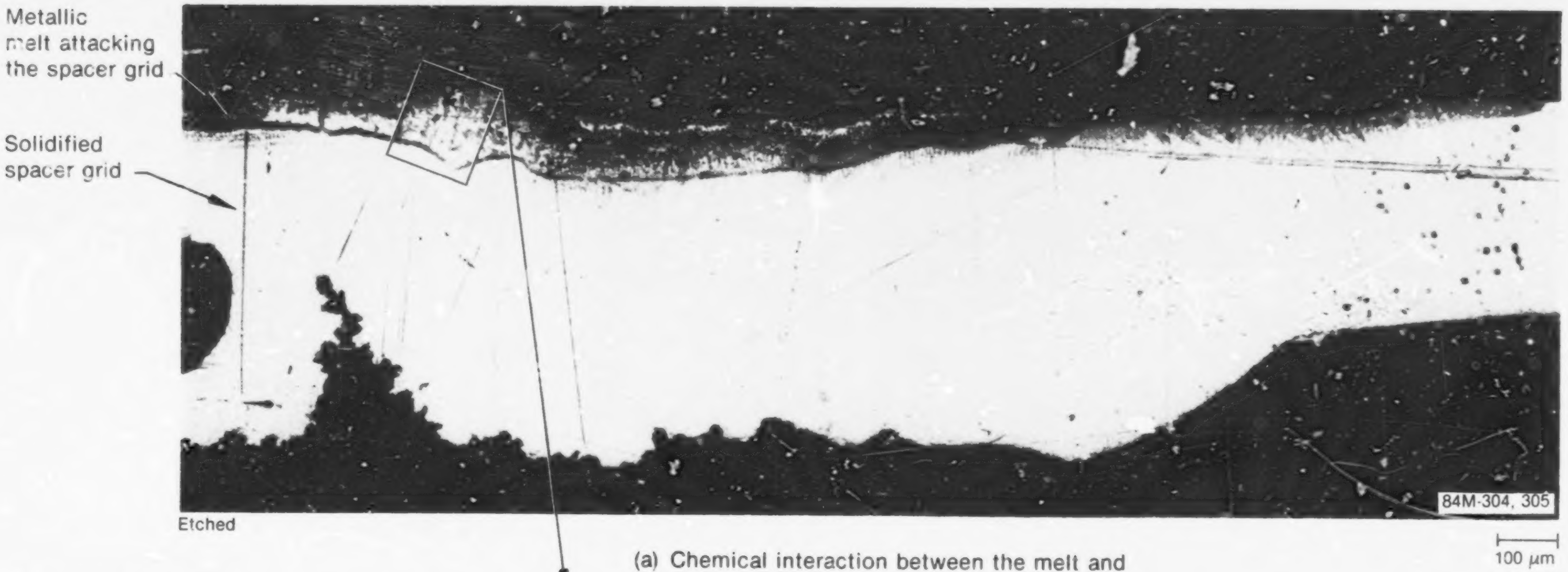
Metallic melt attacking the spacer grid
Solidified spacer grid
Etched
84M-304, 305
100 µm

(a) Chemical interaction between the melt and partially molten Inconel 718 spacer grid

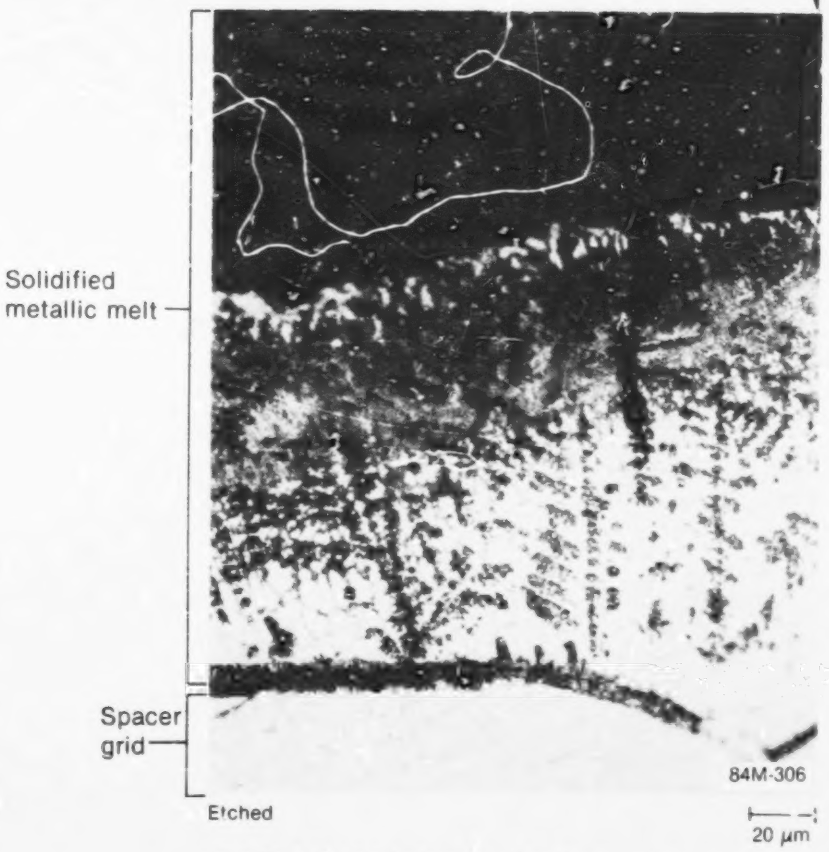
Solidified metallic melt
Spacer grid
84M-306
Etched
20 µm

(b) Detail of (a) showing the interaction layer

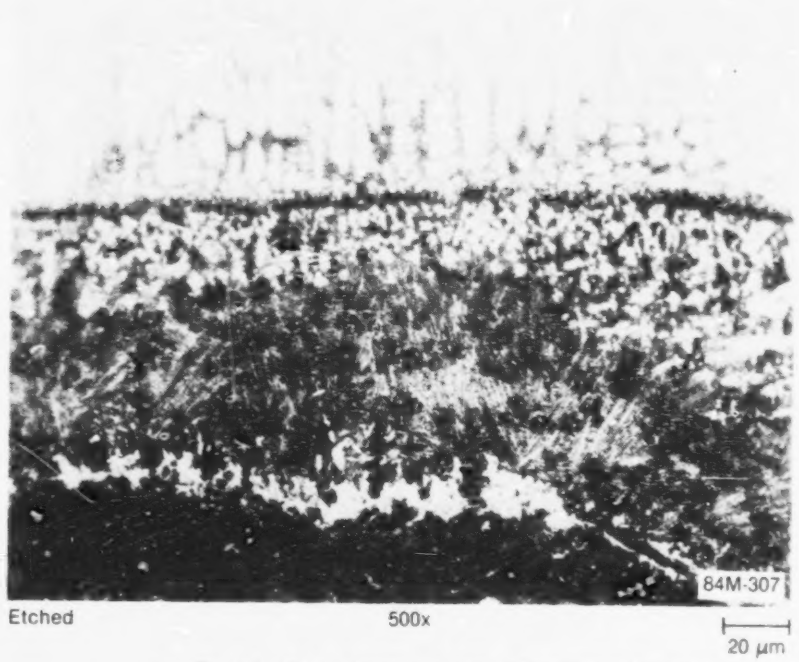
84M-307
Etched
500x
20 µm

(c) Detail of (a) showing the interaction layer

Figure 62. Metallographic appearance of the chemical interaction between the melt and partially molten Inconel 718 spacer grid between Rods 4C and 4D at the 0.055-m cross-section elevation.

melting experiments.[9] The chemical interaction produces a melt which results in the formation of dendrites during cooldown, aligned along the concentration gradient in this region. On the opposite side of the molten spacer grid, slight oxidation of the Inconel occurred on its surface. The melt/Inconel reaction product may have a composition similar to that described for Figure 37.

Mechanical and Chemical Behavior of the Inner Zircaloy Liner

General Remarks. Depending on the elevation of the cross sections, the inner zircaloy liner (zircaloy-2) was either present in its original location [as in the lowest cross section examined (Figure 3)] or the liner had completely disappeared [as at the 0.245-, 0.27-, and 0.495-m elevations (Figures 6, 7, and 9)]. The zircaloy liner was oxidized to different degrees up to full transformation into ZrO_2. It cannot be determined whether the liner failed mechanically before or after it was oxidized. However, at the 0.825- and 0.915-m cross-section elevations, the zircaloy liner was deformed before it was oxidized (Figures 10 and 11), since ZrO_2 probably cannot be deformed in such a strong way at the estimated temperature. At these elevations, an overpressure combined with locally high temperatures existed.

After the liner failed, the zircaloy liner material and part of the ZrO_2 insulation material could participate in the chemical interactions with the fuel rods. As a result of the interaction with steam, the liner contributed to the H_2 generation, whereas the ZrO_2 insulator acted as an additional oxygen donor.

The chemical state of the zircaloy liner reveals that severe temperature differences existed at the same cross-section elevation. Figure 4 shows, for example, that the side where the melts contacted the liner (90 through 270° orientation) was heavily attacked, whereas only weak interactions took place on the opposite side.

In the following, the different oxidation states of the zircaloy liner will be described in detail.

Chemical State of the Zircaloy Liner. The oxidation state of the liner at the 0.145-m cross-section elevation covers the range from slightly oxidized to completely oxidized (Figure 63). Figure 63b shows the liner near Rod 1B slightly oxidized on both surfaces. The thickness of the [α-Zr(O) + ZrO_2] double layer is about 50 μm. The transformed β-zirconium structure reveals that the liner has reached temperatures above 1243 K at this location [(α + β)/β-zirconium transformation temperature]. However, the zircaloy liner does not show any deformation compared to that at 135 and 210° orientation. At the latter two locations (and also in between), the liner is strongly deformed and completely oxidized (Figures 63a, 63c), both of which were conditions caused by much higher temperatures in this region. Figure 63c shows that chemical interactions between the liner and the ZrO_2 cylinder took place. The zircaloy liner seems to consist of two ZrO_2 layers at this location.

The metallographic cross section at the 0.245-m elevation (Figure 6) shows a zircaloy liner remnant which has experienced different degrees of oxidation (shown in Figure 64). The two photographs were taken near one another. The upper photograph shows uniform oxidation of the zirconium liner at both surfaces, resulting in an [α-Zr(O) + ZrO_2] double layer thickness of about 200 μm on each side (Figure 64). The lower photograph reveals much higher temperatures, since there is no prior β-zirconium present any more [only α-Zr(O) (Figure 64)]. The ZrO_2 layer at the ZrO_2/α-Zr(O) interface was hypostoichiometric and decomposed (eutectoid) into stoichiometric ZrO_2 and α-Zr(O) during cooldown. With respect to the (Zr-O) phase diagram, the temperature was apparently above the tetragonal/cubic ZrO_2 phase transition temperature of about 1753 K (Figure 14). A few tin precipitates are visible in the center of the α-Zr(O) phase.

Microstructural features of the zircaloy liner are shown in Figures 65 and 66. Figure 65a shows the zircaloy liner oxidized on both sides (low magnification). The oxide layer toward the saddle (external) is about 350 μm thick, and the oxide layer toward the bundle (internal) is between 550 and 650 μm at this location. In between is α-Zr(O) containing ZrO_2 precipitates (250 to 300 μm thick). The microstructure of the metallic α-Zr(O) indicates that this part was molten, which implies that temperatures above 2223 K [the melting point of oxygen-saturated α-Zr(O)] were exceeded (Figures 65b and 65c). The composition of the melt was probably slightly hypostoichiometric (>40 at. % oxygen, Figure 14) and may have been a homogeneous or heterogeneous melt, depending on temperature. During cooldown of the melt, ZrO_2 precipitated randomly before the (Zr,O) melt solidified. With respect to the (Zr,O) phase diagram (Figure 14), the ZrO_2 precipitates should be hypostoichiometric and decompose (eutectoid)

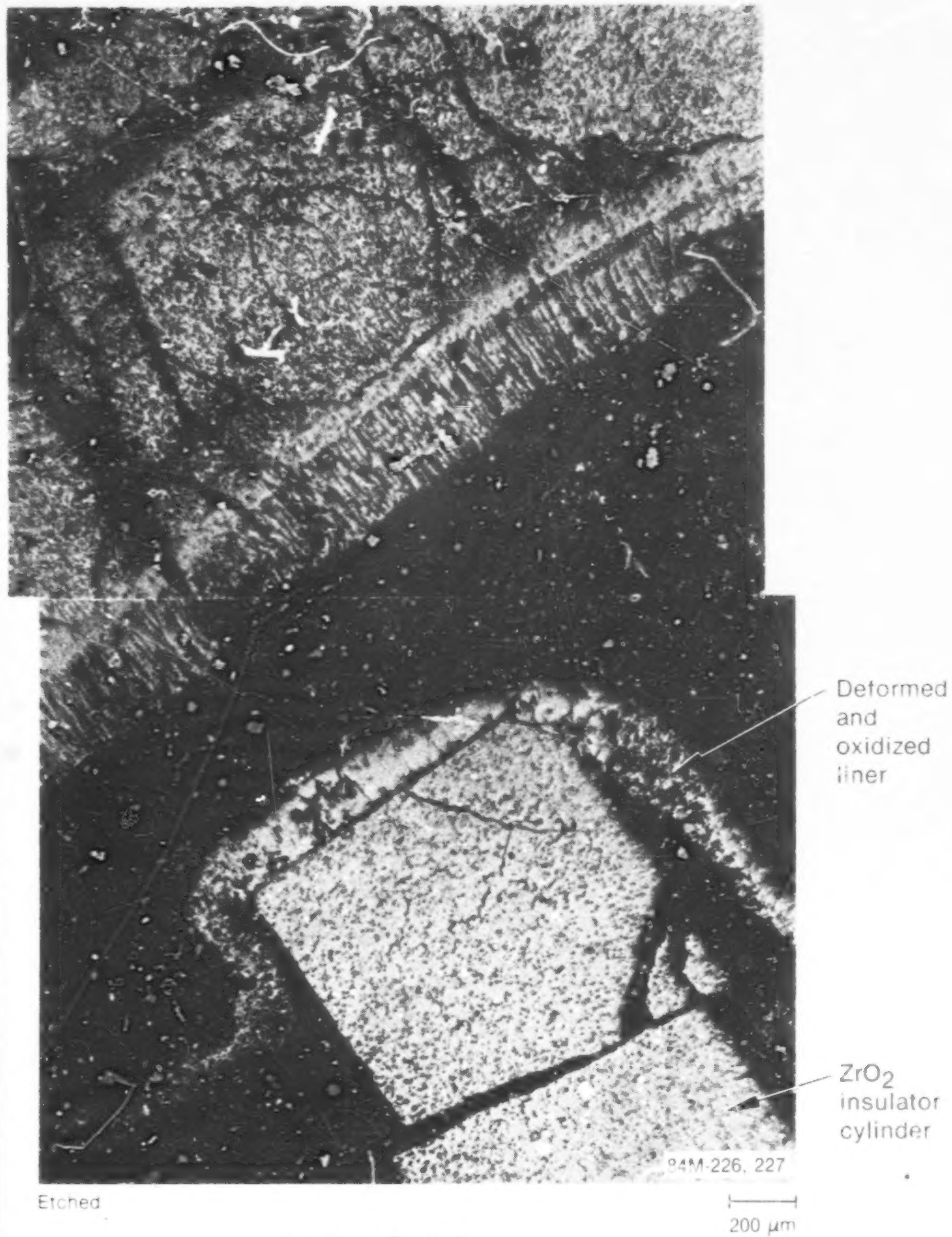
Deformed and oxidized liner
ZrO$_2$ insulator cylinder
84M-226, 227
Etched
200 μm

(a) Near Rod 6E

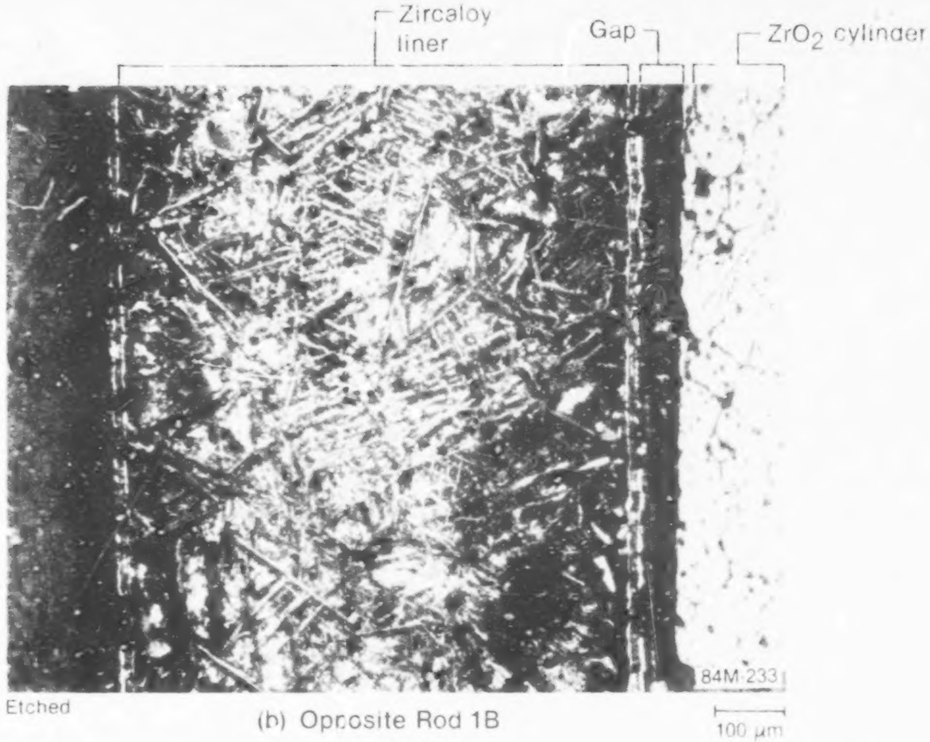
Zircaloy liner
Gap
ZrO$_2$ cylinder
84M-233
Etched
100 μm

(b) Opposite Rod 1B

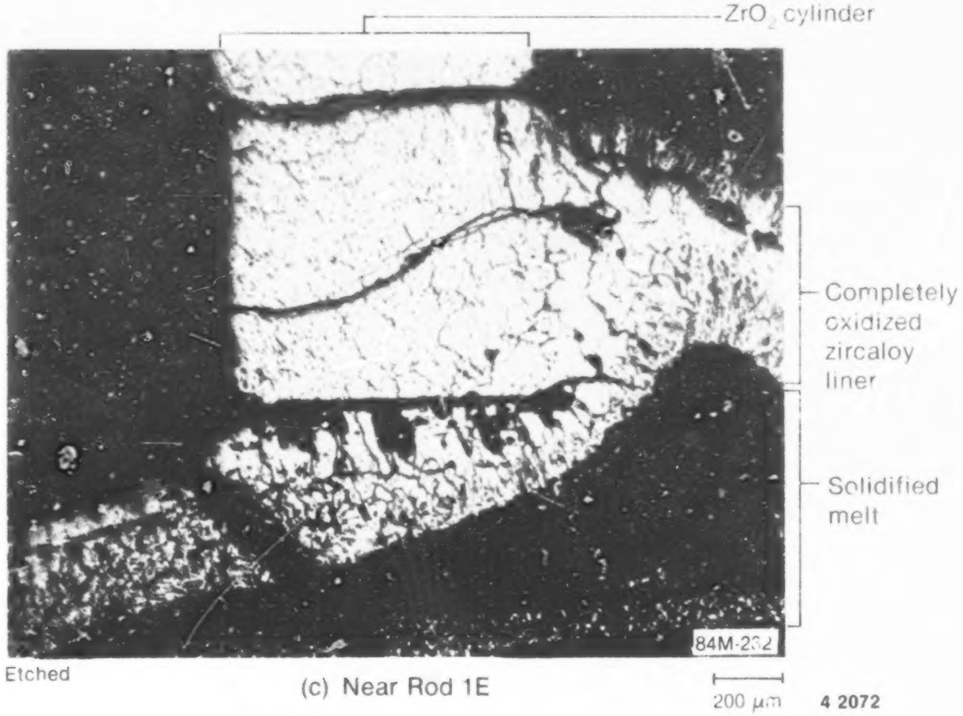
ZrO$_2$ cylinder
Completely oxidized zircaloy liner
Solidified melt
84M-232
Etched
200 μm
4 2072

(c) Near Rod 1E

Figure 63. Deformed and undeformed zircaloy liner in different chemical oxidation states at the 0.145-m cross-section elevation.

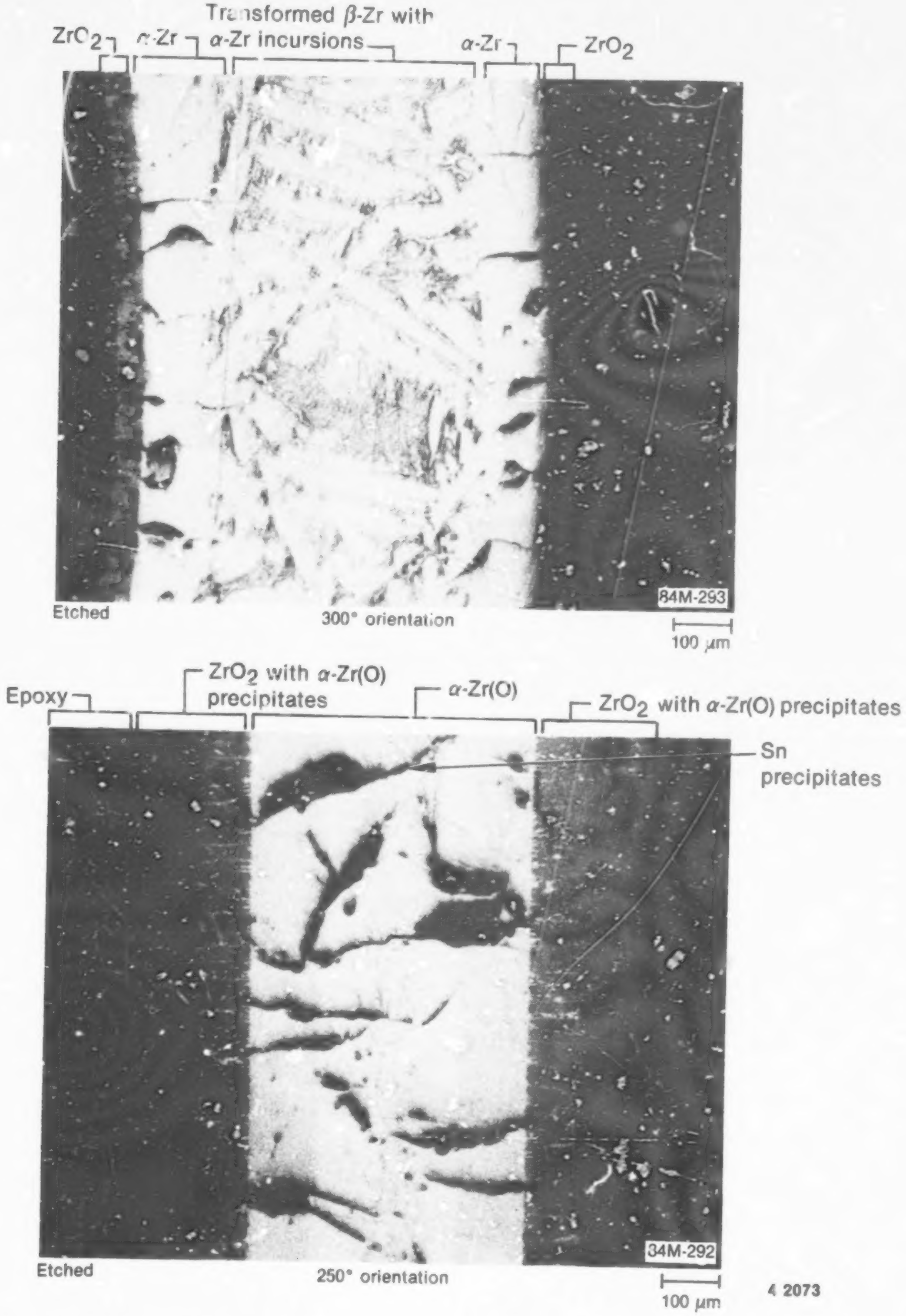
Transformed β-Zr with α-Zr incursions
ZrO2
α-Zr
α-Zr
ZrO2
Etched
300° orientation
84M-293
100 μm
Epoxy
ZrO2 with α-Zr(O) precipitates
α-Zr(O)
ZrO2 with α-Zr(O) precipitates
Sn precipitates
Etched
250° orientation
84M-292
100 μm
4 2073

Figure 64. Chemical state of the zircaloy liner remnant at the 0.245-m cross-section elevation.

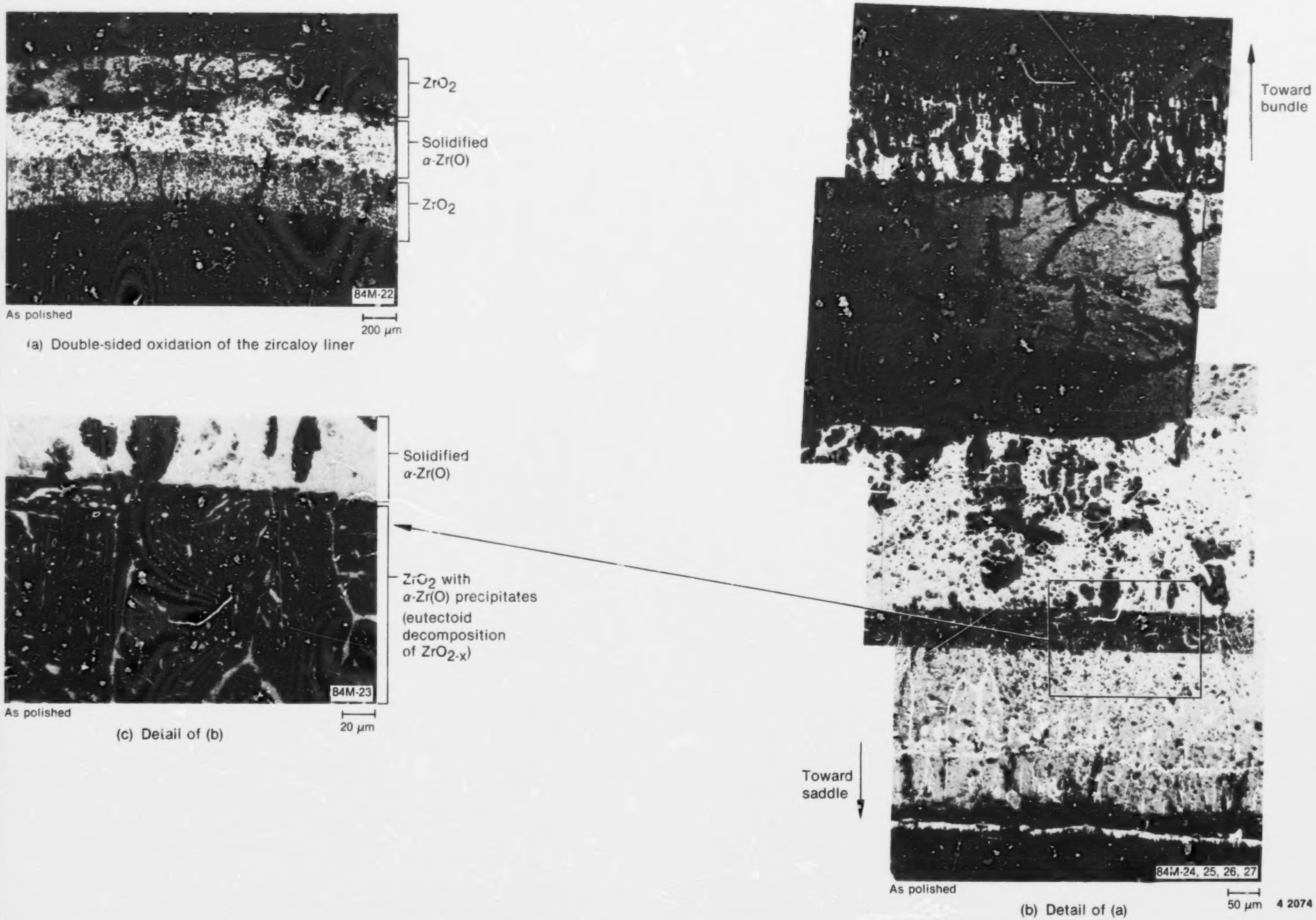

ZrO2
Solidified α-Zr(O)
ZrO2
84M-22
As polished
200 µm
Toward bundle
Solidified α-Zr(O)
ZrO2 with α-Zr(O) precipitates (eutectoid decomposition of ZrO2-x)
84M-23
As polished
20 µm
Toward saddle
84M-24, 25, 26, 27
As polished
50 µm
4 2074

(a) Double-sided oxidation of the zircaloy liner

(c) Detail of (b)

(b) Detail of (a)

Figure 65. Appearance of the zircaloy liner, 180°, at the 0.915-m cross-section elevation. The metallic part of the liner reached temperatures above 2223 K, the melting point of oxygen-stabilized α-Zr(O).

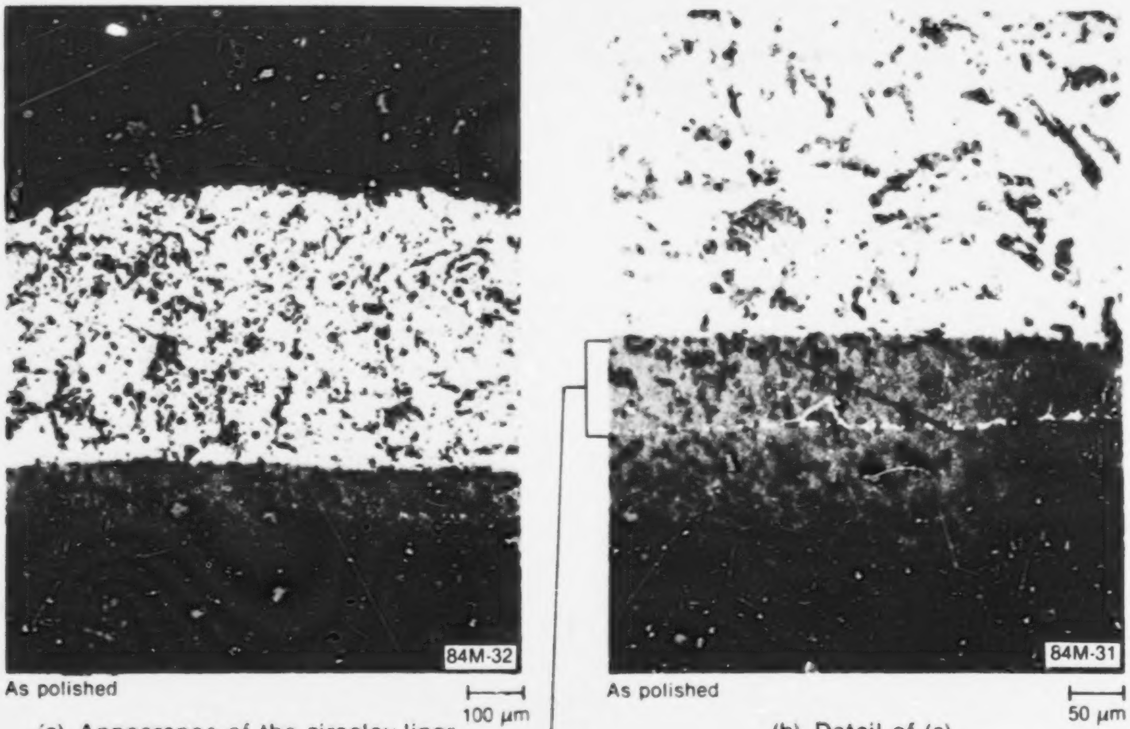
84M-32
As polished
100 μm
84M-31
As polished
50 μm

(a) Appearance of the zircaloy liner

(b) Detail of (a)

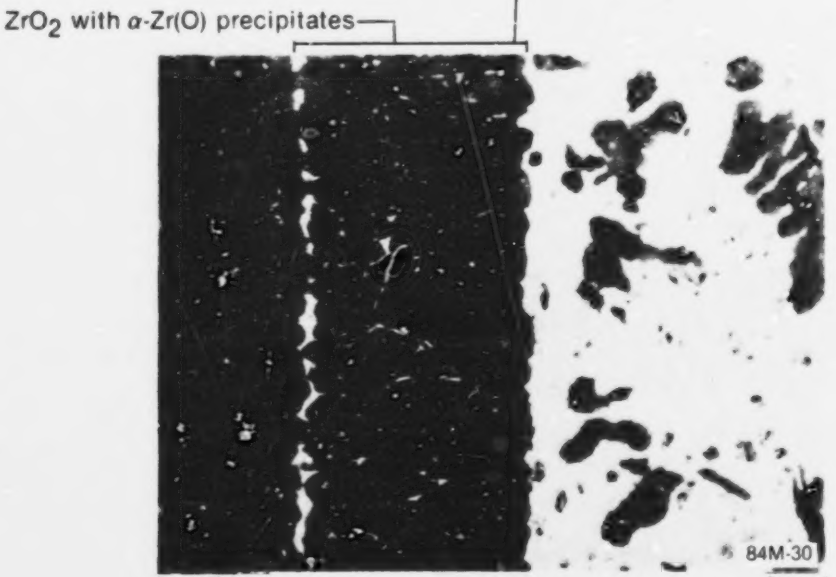
ZrO2 with α-Zr(O) precipitates
84M-30
As polished
20 μm
4 2075

(c) Detail of (b)

Figure 66. Appearance of the zircaloy liner, 135°, at the 0.915-m cross-section elevation. The metallic part of the liner reached temperatures above 2223 K, the melting point of oxygen-stabilized α-Zr(O).

during further cooldown into stoichiometric ZrO_2 and α-Zr(O). For this reason, metallic α-Zr(O) should be present within the ZrO_2 precipitates. Figure 65c shows that some α-Zr(O) formed in at least one ZrO_2 precipitate. A similar microstructure with a higher amount of ZrO_2 in the solidified (Zr,O) melt can be seen at another location of the zircaloy liner, as shown in Figure 66.

Figures 65 and 66 clearly show that the ZrO_2 layer on the internal surface of the liner was stoichiometric, whereas the ZrO_2 layer on the external surface was hypostoichiometric and decomposed into stoichiometric $ZrO_{2.00}$ + α-Zr(O) during cooldown, as described above for the ZrO_2 precipitates. This indicates that the eutectoid decomposition of the hypostoichiometric ZrO_{2-x} may have occurred at different temperatures across the oxide layer, since an oxygen gradient within the ZrO_{2-x} layer has to be assumed (Figures 65b and 66c). In the zirconium-ZrO_2 system, two eutectoid reaction isotherms exist; and, depending on its chemical composition, the ZrO_{2-x} decomposes either at about 1773 K or below 1273 K (Figure 14). The microstructures of the internal and external ZrO_2 layers clearly indicate that enough steam was available within the bundle for oxidation reactions with the liner but not toward the saddle (external), where steam starvation conditions apparently existed. This also resulted in the different thicknesses of the ZrO_2 layers.

Figure 67 shows a possible zircaloy liner remnant, located near the zircaloy saddle, that is almost completely transformed into ZrO_2. The microstructure shows that it was still a hypostoichiometric ZrO_2, maybe with a tiny amount of liquid α-Zr(O) present at temperature, which underwent eutectoid decomposition into $ZrO_{2.00}$ + α-Zr(O). The fine α-Zr(O) needles within the ZrO_2 grains are typical of this type of decomposition. Similar structures could be noticed in almost fully oxidized zircaloy cladding when high temperatures (>2033 K, the melting point of zircaloy) were reached during transient out-of-pile tests with LWR fuel rod segments under oxidizing conditions.[12]

Mechanical and Chemical Behavior of the ZrO_2 Insulator

After the zircaloy liner failed, the ZrO_2 insulator material[a] (high-density cylinders and low-density powder) had access to the bundle region and could contribute to the chemical interactions. The insulator material acted as an additional oxygen source, since solid and liquid metallic zircaloy can reduce ZrO_2 and form α-Zr(O). However, since the amount of fuel that can be dissolved by molten zircaloy depends on the oxygen content of the (Zr-O) melt and decreases with increasing oxygen content, the reaction of molten zircaloy with the ZrO_2 insulator could influence fuel dissolution. In any case, the ZrO_2 insulator material resulted in a larger proportion of ceramic material in the bundle region than could be expected in a fuel rod bundle of a power reactor undergoing an SFD accident with similar steam availability.

The intact microstructure of a high-density ZrO_2 cylinder is shown in Figure 68. Some porosity exists within the grains; the larger black spots are pull-outs. The ZrO_2 cylinders were attacked by (U,Zr,O) melts and/or the zircaloy liner to different degrees, as shown in Figures 63, 69 and 70. As a result of the chemical interaction, the zircaloy cylinder was partly dissolved and the high-density insulators disintegrated preferentially along the grain boundaries. (This is similar to the UO_2 disintegration.) Figure 70 shows a higher magnification of the ZrO_2/(U,Zr,O)-melt interface. Due apparently to the reduction of ZrO_2 to α-Zr(O) and the high temperature which has to be assumed, the α-Zr(O) phase was liquid and is the reason for the loss of cohesion of the individual ZrO_2 grains, and also within the grains themselves.

It is important to point out that the ZrO_2 can only be reduced by a metallic (U,Zr,O) or (Zr,O) melt. However, since the solidified melt which attacked the ZrO_2 insulators now looks ceramic, it had to be oxidized later in the test transient. This is another example which shows that the final microstructure and the chemical state of the various materials that can be recognized were, in many cases, changed due to oxidation by steam. There is only a very limited tendency for the oxidized melts to interact with ZrO_2 to form a type of solid solution.

Mechanical and Chemical Behavior of the Zircaloy Saddle

The zircaloy saddle remained intact and did not deform at any examined location (Figures 3 through 11). There was no indication of an interaction with steam (Figure 71), probably due to the rather low temperatures reached at the saddle location during the test. The microstructure of the saddle (Figure 72) shows that the maximum

---

[a] Chemical composition: 90.5 wt% ZrO_2, 8 wt% Y_2O_3, 1.5 wt% HfO_2).

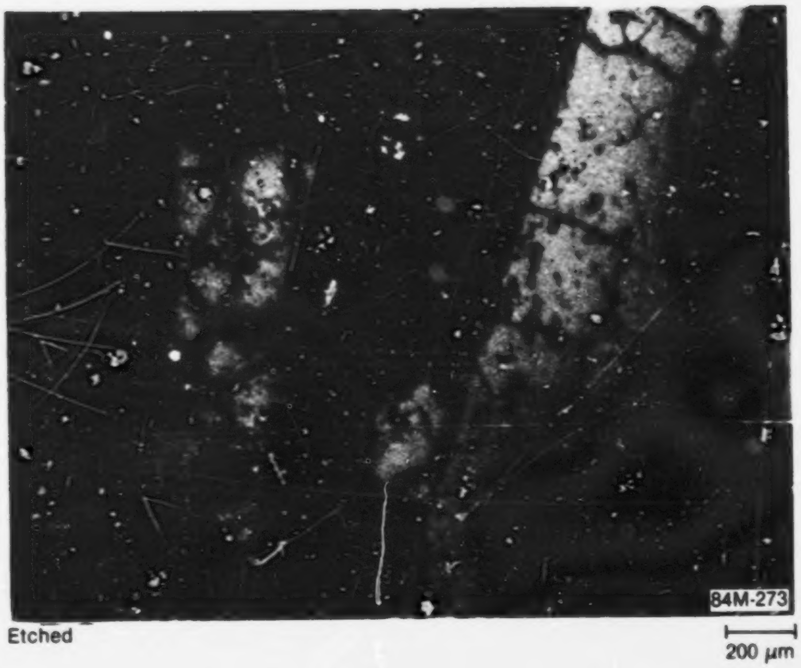
84M-273
Etched
200 μm

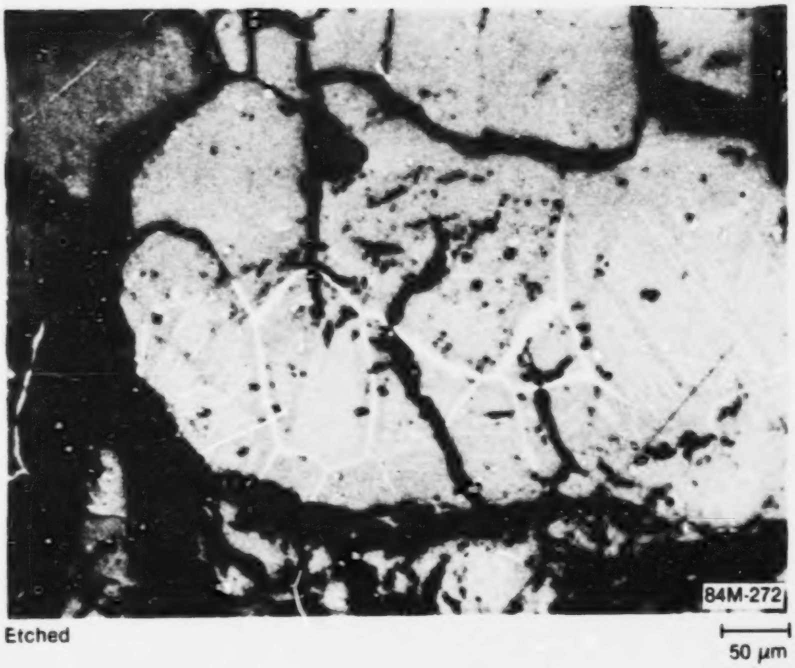
84M-272
Etched
50 μm
4 2076

Figure 67. Possible zircaloy liner remnant which is almost completely transformed into ZrO_2 (near the saddle, 90°, at the 0.245-m cross-section elevation).

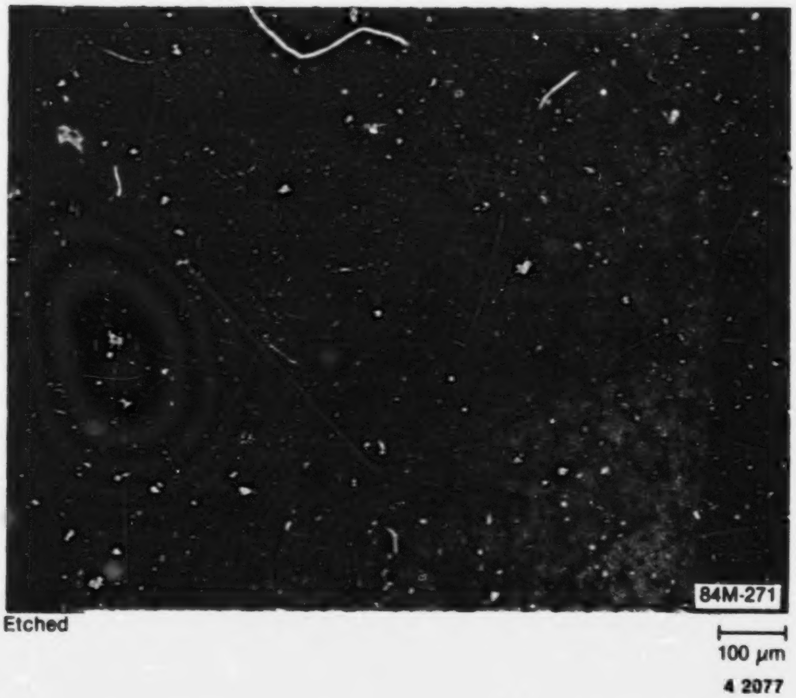
84M-271
Etched
100 μm
4 2077

Figure 68. High-density ZrO_2 cylinder (near the saddle, 90° at the 0.245-m cross-section elevation).

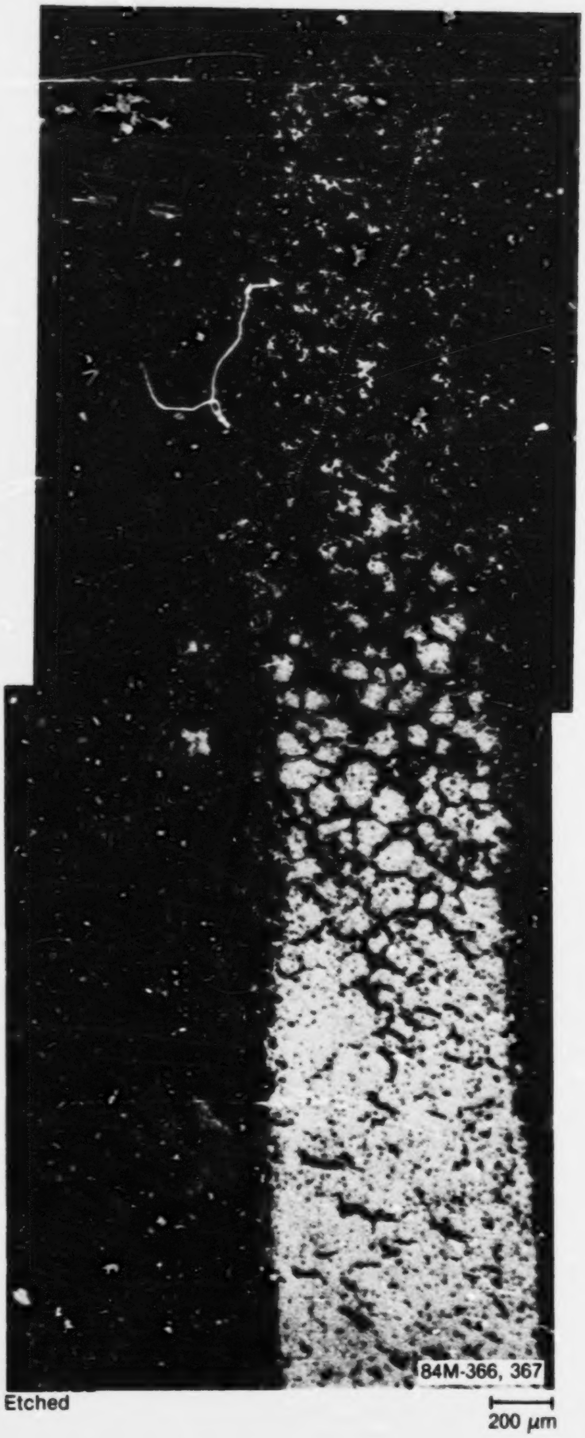
84M-366, 367
Etched
200 μm
4 2078

Figure 69. Attack of a ZrO_2 insulator cylinder by a (U,Zr,O) melt with partial disintegration (object number 8 at the 0.495-m cross-section elevation).

BEST COPY AVAILABLE

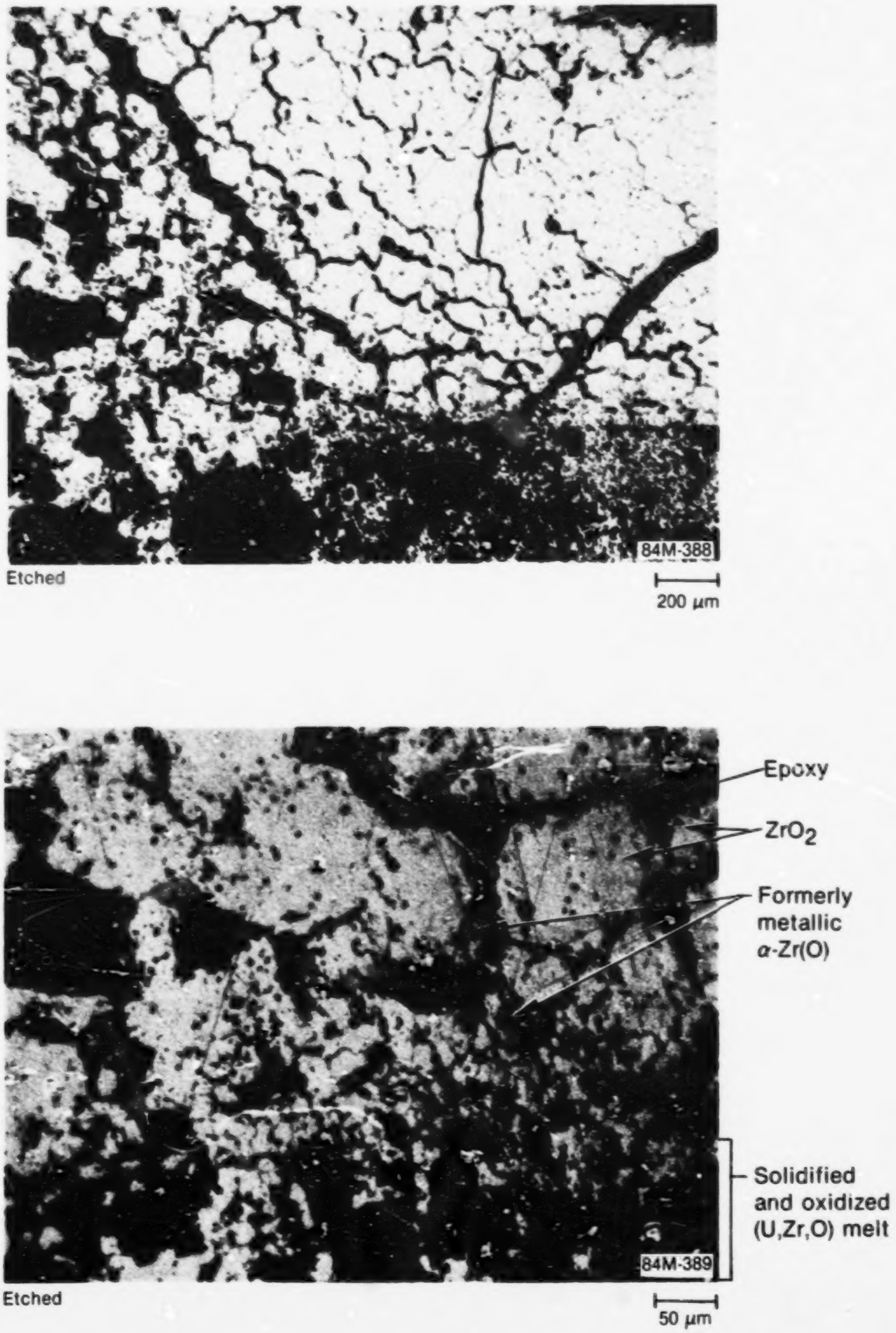
84M-388
Etched
200 μm
Epoxy
ZrO_2
Formerly metallic α-Zr(O)
Solidified and oxidized (U,Zr,O) melt
84M-389
Etched
50 μm

4 2079

Figure 70. Chemical attack of a ZrO_2 insulator cylinder by a (U,Zr,O) melt with partial disintegration (near object number 4, 315°, at the 0.495-m cross-section elevation).

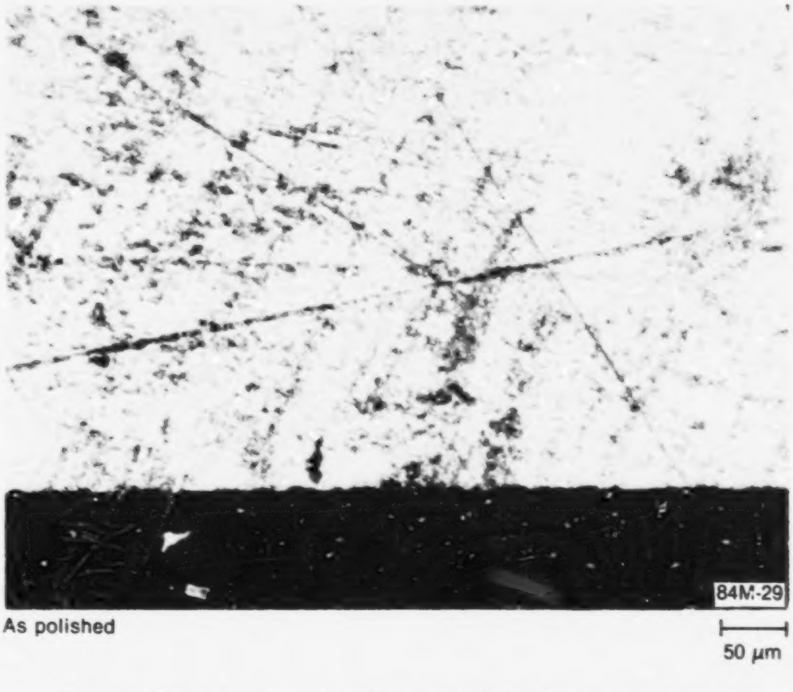
84M-29
As polished
50 μm

Figure 71. Zircaloy saddle, 180°, at the 0.915-m cross-section elevation.

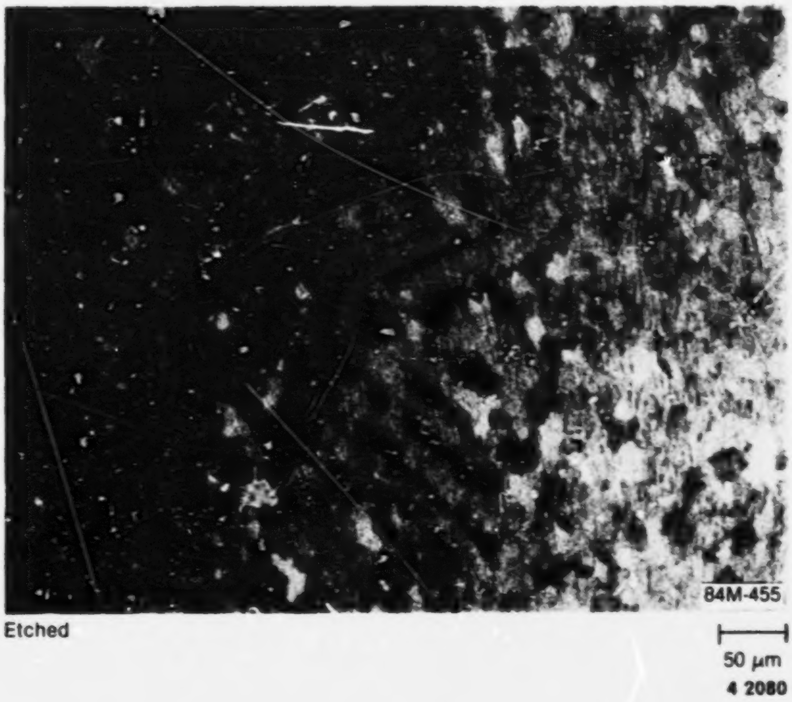
84M-455
Etched
50 μm
4 2080

Figure 72. Zircaloy saddle, 0°, at the 0.17-m cross-section elevation.

temperatures reached were below 1173 K. The zircaloy structure is still α-zircaloy, with no onset of $\alpha/(\alpha + \beta)$-phase transformation visible. (The $\alpha/(\alpha + \beta)$-phase transformation starts at about 1093 K and is completed at 1243 K.)

Chemical Behavior of the Thermocouples

The TC wires consisted of a tungsten/rhodium (W/Rh) alloy and were electrically insulated by beryllium oxide (BeO). Several different TC sheath materials were used: (a) zirconium/ZrO_2 and zirconium/tantalum for the fuel cladding interior TC; (b) molybdenum/rhenium alloy (50/50) for the fuel centerline TC; and (c) zirconium or Inconel for the shroud and steam probe TC.

Figure 73 shows the internal cladding TC of Rod 3A (which has experienced higher temperatures resulting in strong chemical interactions, see Figures 25 and 26). The sheath of this TC was a zirconium/ZrO_2 duplex tube. The internal ZrO_2 layer apparently reacted with the outer zirconium tube, forming an α-Zr(O) reaction layer. Also, some oxygen uptake occurred on the outside surface of the sheath. The structure of the remaining sheath appears to be two-phase and previously molten. The BeO insulation is gone, and an electrical short can be seen between the TC wires.

Figure 74 shows the chemical state of a fuel centerline TC. The TC sheath was apparently attacked by the BeO but not by the UO_2 fuel. The sheath/BeO interface is very irregular and looks as if the reaction products could have evaporated. The BeO is two-phase, perhaps a Be-BeO eutectic. (The melting point of BeO is $\simeq$2823 K). Figure 75 shows a similar ceramic phase which also contains many very small, metallic particles, indicating that molten and oxidation-resistant components of the TC material or spacer grids may have been part of the melt. The phase ratio of the ceramic material (formerly BeO) in Figure 74 is different than the phase ratio in Figure 75.

Fuel Structure Appearance

Most of the various fuel structure appearances have been described previously. In this section, only structures which reveal additional information will be considered.

Figure 76 shows a part of a UO_2 pellet cross section, the oxidized cladding, and between them the previously metallic (U,Zr,O) melt which also penetrated along cracks into the pellet. The fuel exhibits different structures; it is not clear if this is caused by a second phase or if it is just a surface effect (relief). A part of the UO_2 grains show strong pore formation of the grain boundaries.

Figure 77 shows a type of second phase within the UO_2 grains, similar to that of Figure 46c, evidently caused by fuel oxidation (U_4O_9 precipitates).

Figure 78 exhibits a rather loose fuel grain structure at the fuel/melt interface. A densified zone exists between the fuel and the solidified ceramic material which could be the previously metallic (U,Zr,O) melt that dissolved and disintegrated a part of the solid fuel before it was oxidized.

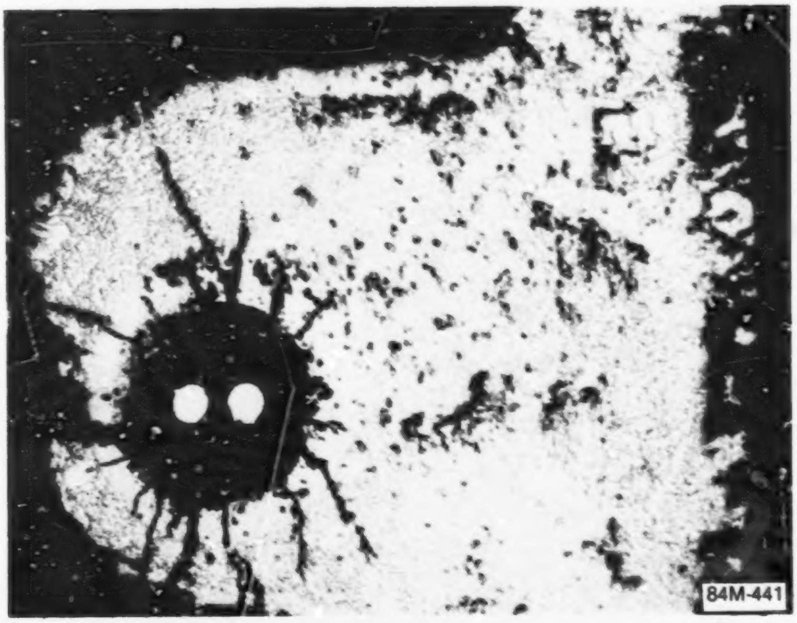
84M-441
As polished
200 μm

(a) Cladding internal thermocouple

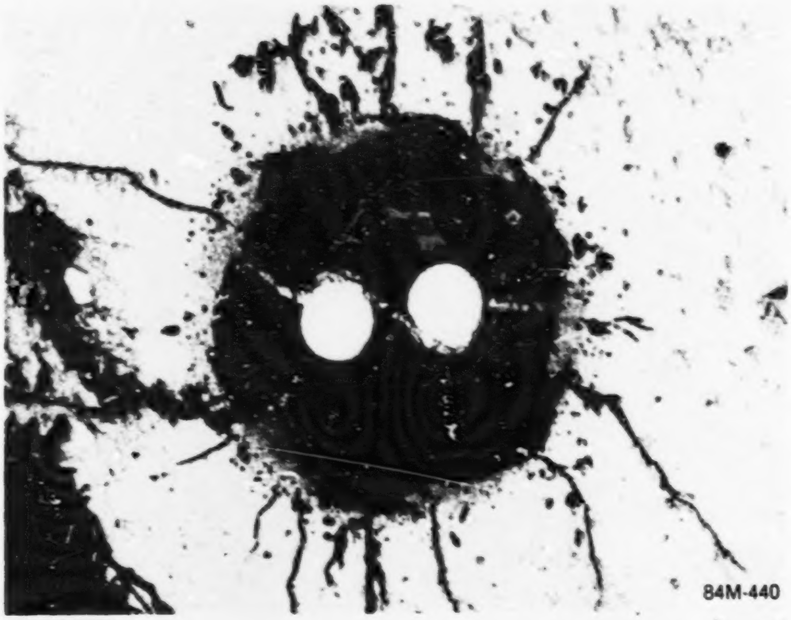
84M-440
As polished
100 μm
4 2081

(b) Detail of (a)

Figure 73. Cladding internal TC in Rod 3A, 315°, at the 0.17-m cross-section elevation (TC wires, W/Rh; insulation, BeO; sheath, Zr/ZrO_2 duplex tube).

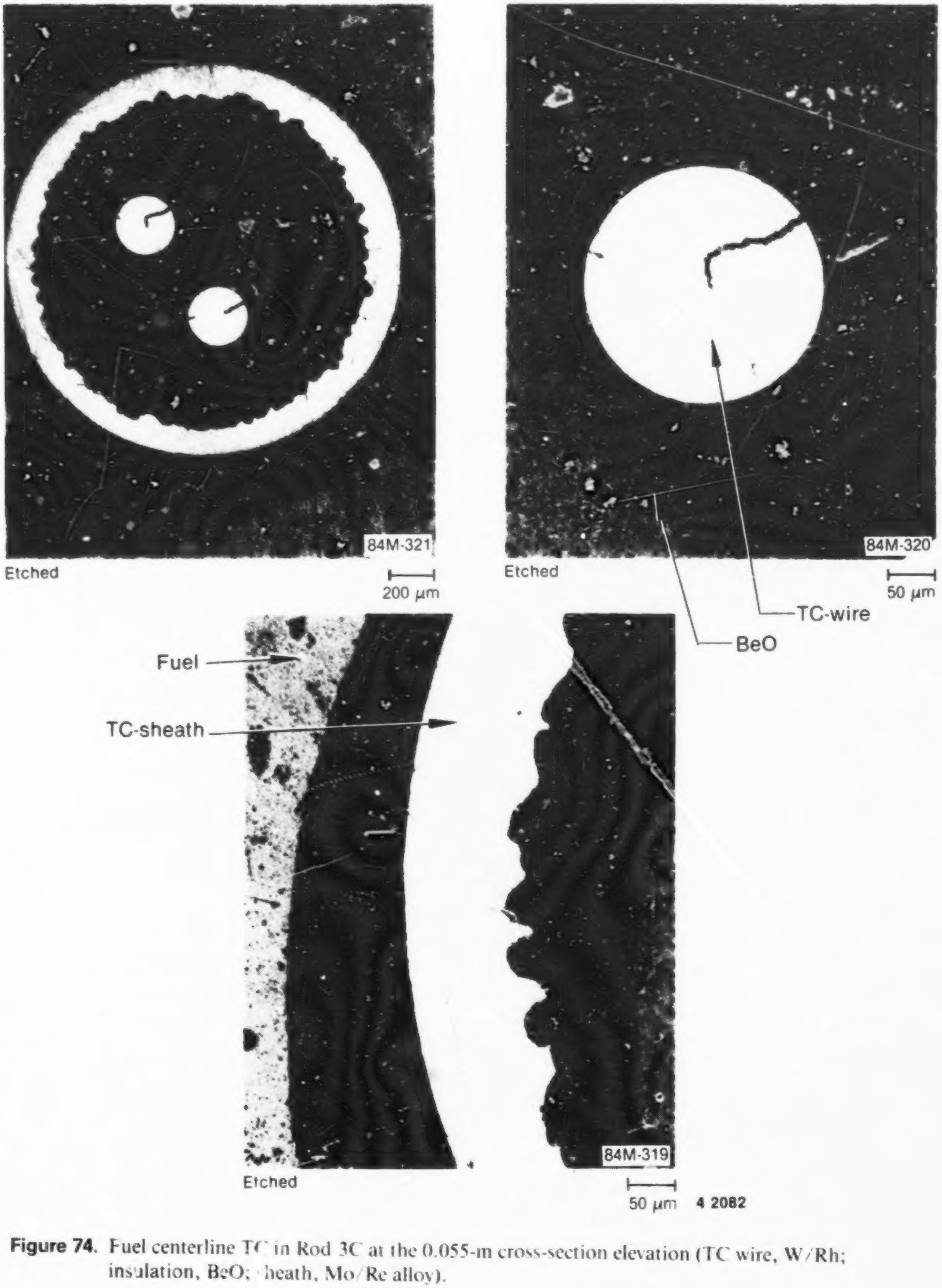
84M-321
Etched
200 μm
84M-320
Etched
50 μm
TC-wire
BeO
Fuel
TC-sheath
84M-319
Etched
50 μm
4 2082

Figure 74. Fuel centerline TC in Rod 3C at the 0.055-m cross-section elevation (TC wire, W/Rh; insulation, BeO; sheath, Mo/Re alloy).

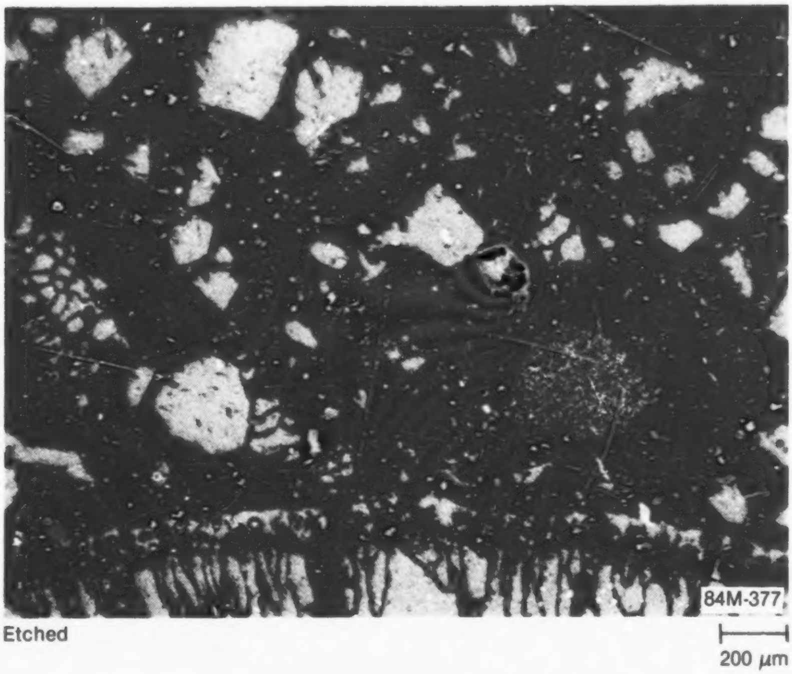
84M-377
200 μm

Etched

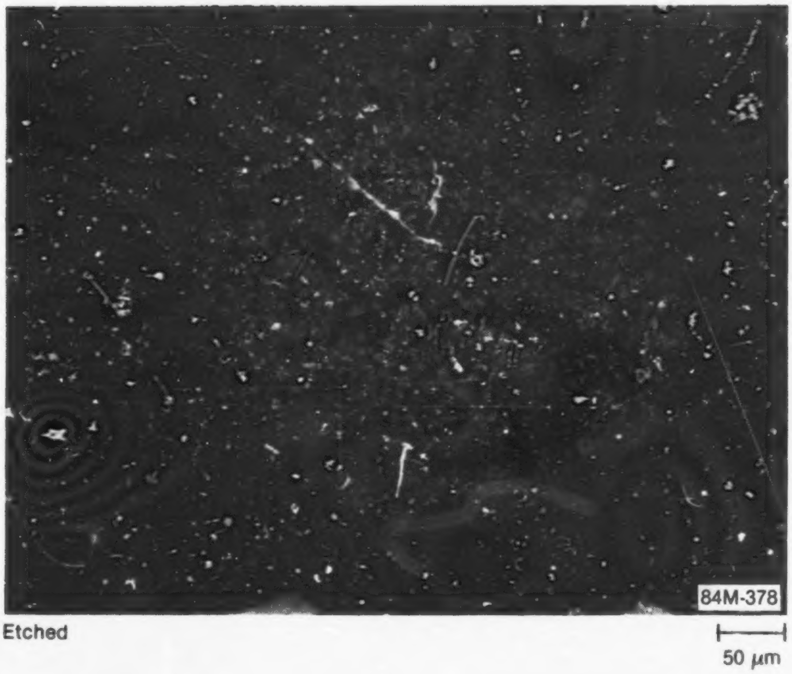
84M-378
50 μm

Etched

4 2083

Figure 75. Debris near cladding remnant on object number 11, 60°, at the 0.495-m cross-section elevation (may be Be/BeO eutectic).

BEST COPY AVAILABLE

BLANK PAGE

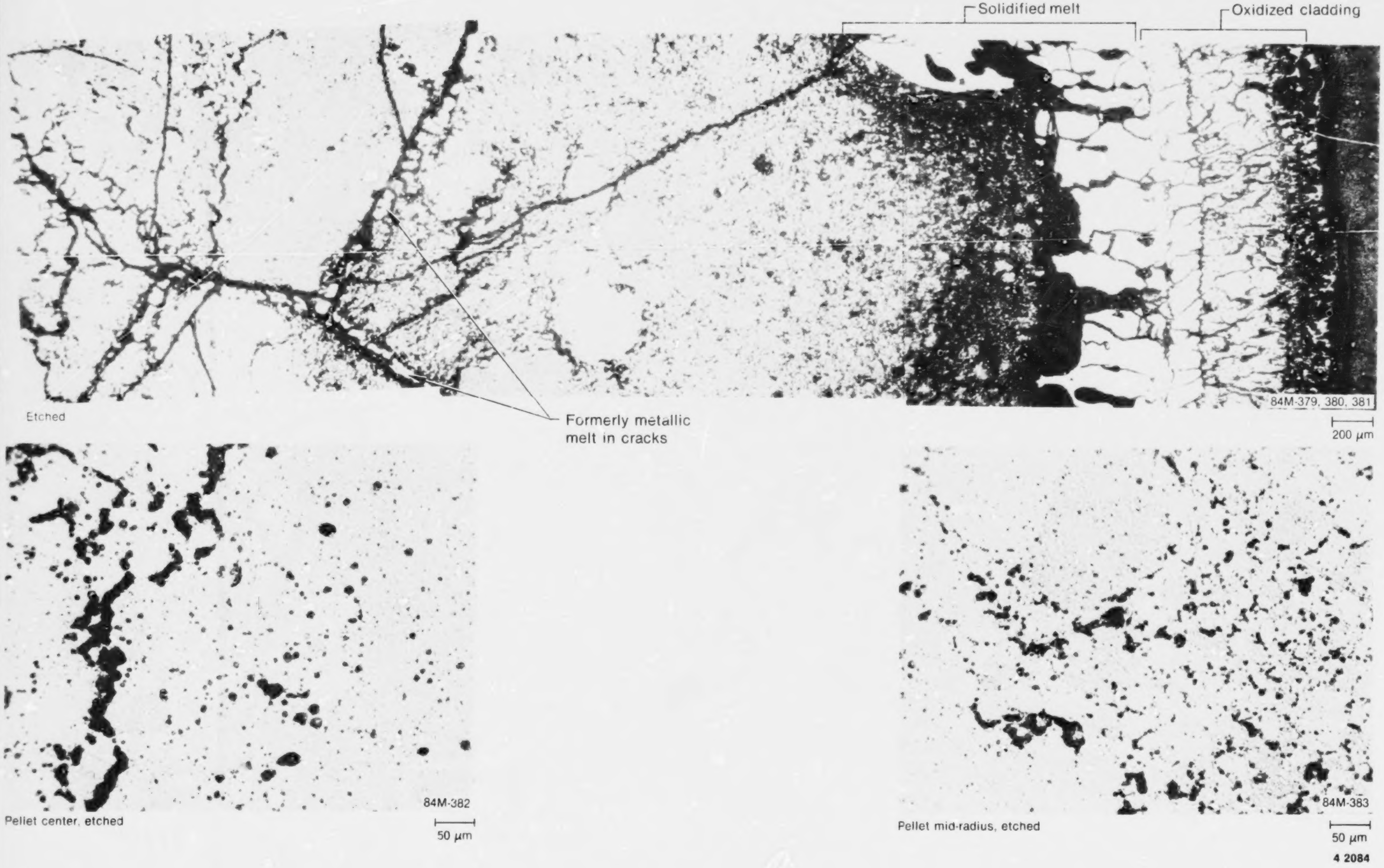
Solidified melt
Oxidized cladding
Etched
Formerly metallic melt in cracks
84M-379, 380, 381
200 μm
Pellet center, etched
84M-382
50 μm
Pellet mid-radius, etched
84M-383
50 μm
4 2084

Figure 76. Fuel across the pellet cross section shows different conditions (object number 2 at the 0.495-m cross-section elevation). Etching reveals a very fine structure within a few UO_2 regions and pore formation at the grain boundaries.

BEST COPY AVAILABLE

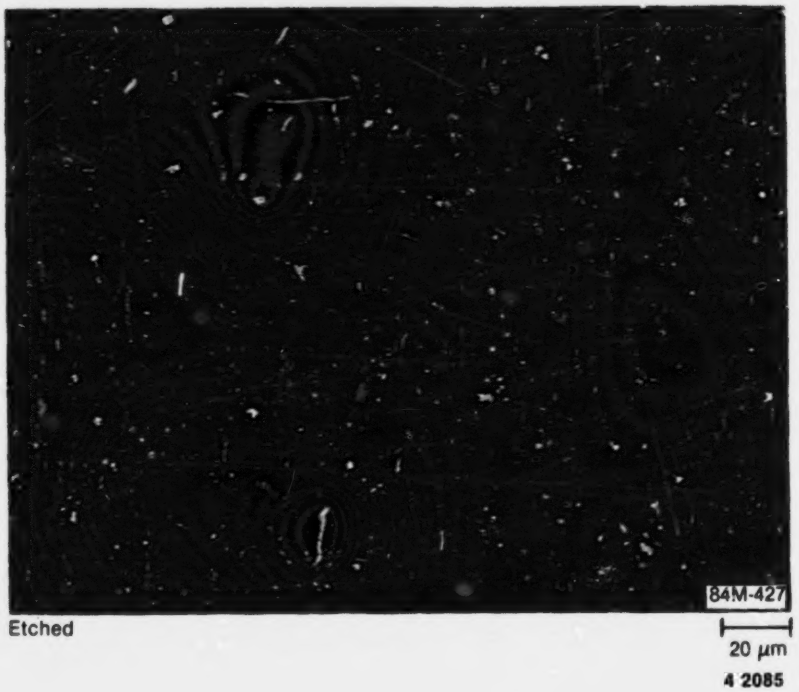
84M-427
Etched
20 μm
4 2085

Figure 77. Fuel structure at the pellet center of Rod 4D at the 0.27-m cross-section elevation.

BEST COPY AVAILABLE

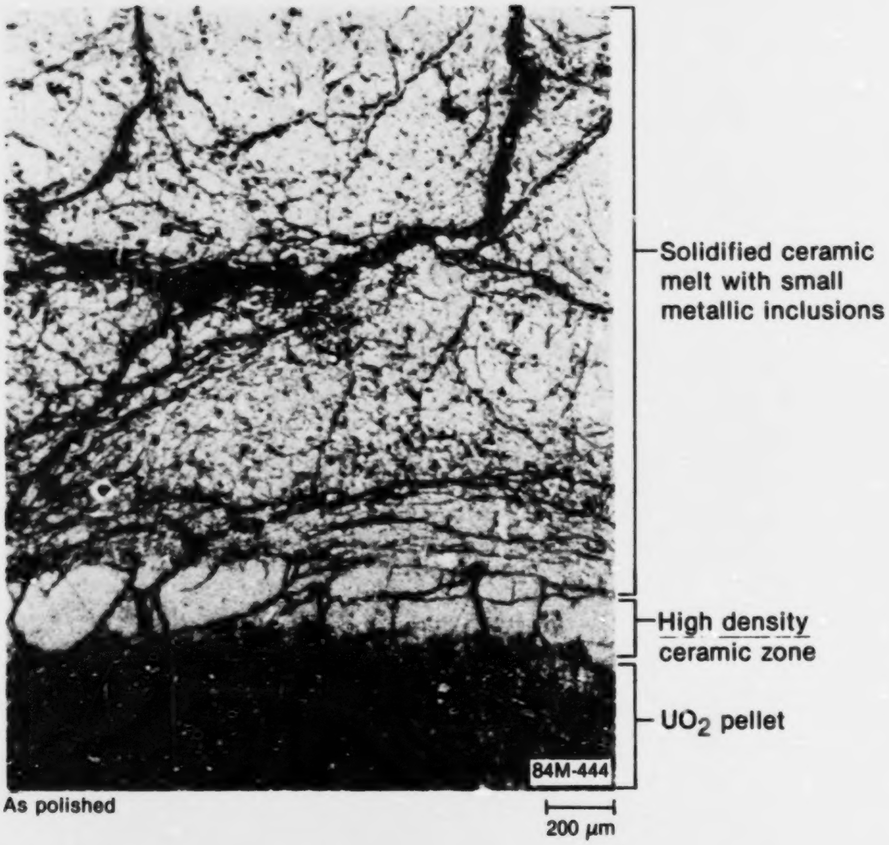
Solidified ceramic melt with small metallic inclusions
High density ceramic zone
UO_2 pellet
84M-444
As polished
200 μm

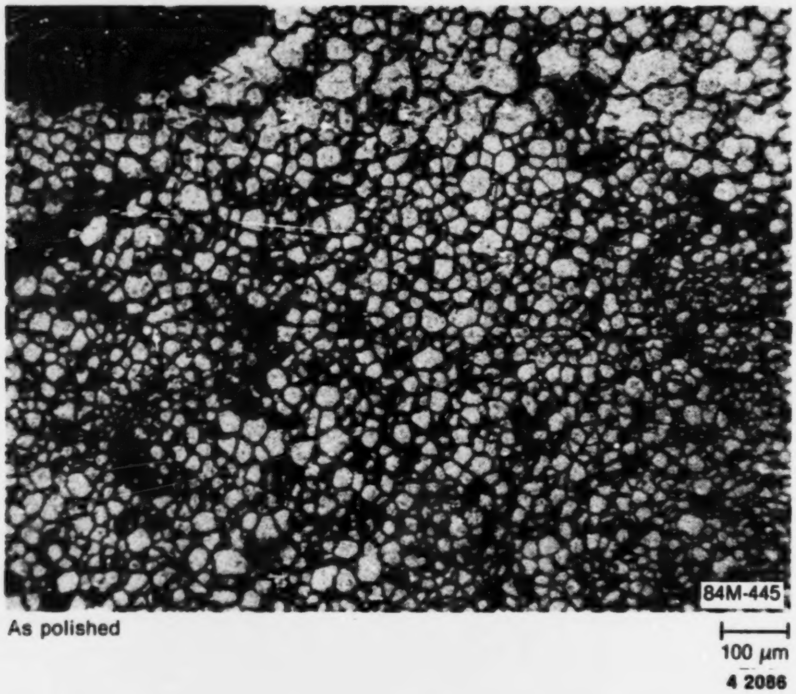
84M-445
As polished
100 μm
4 2086

Figure 78. Fuel structure at the pellet/melt interface of Rod 6E, 90°, at the 0.17-m cross-section elevation.

BEST COPY AVAILABLE

DISCUSSION

The metallographic examination of the SFD-ST fuel rod bundle cross sections has identified a great variety of metallic and ceramic material appearances. About 75% of the microstructures look similar to those of well defined, out-of-pile UO_2/zircaloy interaction experiments under inert gas and oxidizing conditions[1-9,11,12] and "core meltdown" experiments.[15] The remaining microstructures look different, and the mechanisms of their formation could only be postulated. Quantitative chemical analyses of the various reaction products are necessary to obtain more information and positive identification of the different phases. These results are discussed in Reference 16.

The main objectives of this segment of the post-irradiation examination of the fuel rod bundle are: (a) to describe the chemical interactions affecting the bundle components during the test; and (b) to estimate or define temperatures that were involved. In this respect, some of the microstructures can be related without doubt to well defined temperatures which must have been exceeded for some time to form the solid interaction products or metallic and ceramic melts. The highest local temperatures reached could be observed in the highest examined cross-section elevation (0.915 m, Figure 11) by the onset of fuel melting (Figures 54 and 55). There were a few pellets which were either completely or partially molten, and the UO_2 looked foam-like, i.e., very porous. To get this type of UO_2 structure, the temperatures of these UO_2 pellets must have been close to or at the melting point of UO_2, combined with a fast heatup. The melting point of UO_2 depends on the O/U ratio; at an O/U ratio of 2.00, the fuel melts congruently at about 3123 K. At the 0.915-m cross-section elevation, most of the cladding is still present but fully oxidized. Probably the temperature escalation due to exothermic cladding oxidation contributed to a large extent to the high temperatures reached. It is also interesting to note that only very small cladding and fuel relocations occurred at this elevation.

With respect to the formation of the various metallic and ceramic melts at the examined cross-section elevations, a final statement concerning the minimum temperatures reached can be made in a reliable way only after SEM examinations have been performed to determine actual chemical compositions. The chemical composition of the melts could then be used in combination with available phase diagrams to determine melting points or melting regions.

The estimate of temperatures in metallic melts is easier than for ceramic melts. As-received zircaloy cladding will melt at about 2033 K, and its melting point increases with increasing oxygen content up to about 2223 K, the melting point of oxygen-saturated α-Zr(O). UO_2 dissolution by molten zircaloy can already occur in the 2033 to 2223 K temperature range, about 1273 K below the melting point of UO_2 ($\cong$3123 K), forming a metallic (U,Zr,O) melt. But, the molten metallic cladding can also dissolve ZrO_2. Whether the (U,Zr,O) melt is homogeneous or heterogeneous (containing solid particles) depends on the oxygen content. The (U,Zr,O) melt decomposes during cooldown into α-Zr(O) and a (U,Zr) alloy; and at higher oxygen contents, $(U,Zr)O_2$ will also be present. [Typical solidified (U,Zr,O) melts are shown in Figures 33, 34, 35, 36, 41, 42, and 44.]

The important point here is that the solidification of metallic (U,Zr,O) melts occurs over a large temperature range. Upon cooldown of the melt, α-Zr(O) solidifies first at temperatures of about 2223 K, forming, in general, a dendritic (tree-like) structure. The (U,Zr) alloy solidifies as low as 1393 K, depending on the zirconium content of the metallic alloy (see Figure 51). As long as the (U,Zr) alloy is still liquid, the mixture of solid and liquid phases relocates very easily.

The melting points of ceramic melts are much higher. ZrO_2 melts at about 2973 K, and UO_2 melts at about 3123 K. ZrO_2 and UO_2 form a quasi-binary isomorphous system in which the liquidus and solidus do not descend continuously from the melting temperature of one compound to that of the other but, instead, pass through a minimum temperature which lies about 373 K below the melting point of ZrO_2. The indicated melting points of ZrO_2 and UO_2 depend, however, also on their composition (oxygen/metal ratio), as shown in the corresponding phase diagrams (Figures 14, 49). For this reason, additional influences on the melting points or ranges of (U,Zr,O) ceramic melts have to be expected.

Some of the cross sections show large blockages by ceramic material (Figures 4 through 7) in which the greatest part of the UO_2 pellets is still present, whereas the cladding has gone. This indicates that the temperature of the ceramic melts was at least

2873 K but still below the melting point of UO_2; otherwise, the fuel would have melted.

If one compares the minimum temperatures which have to be exceeded to get metallic and/or ceramic melts, a temperature difference of about 1073 K exists between the two melts. It is therefore very important to clarify whether or not some parts of the ceramic-looking melts were initially metallic and oxidized in either the liquid or solid state. A general characteristic of ceramic melt is the appearance of metal ingots of oxygen-resistant materials at room temperature. These are not apparent in metallic melts that oxidize after solidification. Many observations lead to the assumption that parts of the ceramic material were initially metallic; for example, all the cases where the melt penetrated along cracks into the UO_2 pellets before it was oxidized (Figures 44, 45, 46, 48, and 50). With this assumption, it must then be determined whether metallic melt was oxidized in the liquid or solid state. With respect to the microstructure appearance, there should be differences. A homogeneous, liquid (U,Zr,O) melt oxidized at temperature should result in a homogeneous, single-phase $(U,Zr)O_2$ solid solution, as in the case of the surface oxidation of metallic melt droplets (Figures 36, 44, 47, 48, 52, and 53). A solidified homogeneous (U,Zr,O) melt, which decomposes during cooldown into α-Zr(O) and a (U,Zr) alloy, should reveal two different oxidic phases: ZrO_2, with some uranium, and $(U,Zr)O_2$, with small amounts of zirconium (Figure 50). A general, though not necessary, characteristic of a ceramic melt is the appearance of oxygen-resistant materials at room temperature. These inclusions are not apparent in metallic melts that oxidize after solidification.

The general amount of ceramic material in the bundle should be rather high, due to the strong oxidation of the cladding and the zircaloy liner and, especially, due to the ZrO_2 insulator material which enters into the bundle after the inner liner has failed. For this reason, the UO_2 fuel dissolution could be smaller than one would expect in a PWR fuel rod bundle undergoing an SFD accident.

If the metallographically estimated temperatures are compared with the measured temperatures or those calculated from test parameters, the estimated temperatures are, depending on the cross-section elevation, between 973 K (0.915 m) and 1773 K (0.145 m) higher. This is true for local regions within the bundle cross section. The estimated or measured temperature differences become smaller if one considers average bundle cross-section temperatures, since very large temperature differences exist within the individual cross sections (for example, Figures 4 and 5). Also, the thermocouples were known to have failed during the transient and formed junctions at cooler locations; therefore, the measured temperatures only indicate a minimum reading. The reason for the large temperature differences within a certain cross section is not clear.

REFERENCES

1. P. Hofmann and D. K. Kerwin-Peck, "Chemical Interactions of Solid and Liquid Zircaloy with UO_2 Under Transient Nonoxidizing Conditions," *International Meeting on LWR Severe Accident Evaluation, Cambridge, MA, August 28-September 1, 1983.*

2. P. Hofmann and D. K. Kerwin-Peck, *UO_2/Zry-4 Chemical Interactions and Reaction Kinetics from 1000 to 1700°C Under Isothermal Conditions*, KfK Report 3552, 1983.

3. P. Hofmann and D. K. Kerwin-Peck, "UO_2/Zry-4 Chemical Interactions from 1000 to 1700°C Under Isothermal and Transient Temperature Conditions," *Journal of Nuclear Materials, 124,* 1984, pp. 80-105.

4. S. Hagen and S. O. Peck, "Temperature Escalation of Zry-Clad Fuel Rods and Bundles Under SFD Conditions," KfK Report 3656, *International Meeting on LWR Severe Accident Evaluation, Cambridge, MA, August 28-September 1, 1983.*

5. A. Fiege, "SFD Research in Germany; A Review of the KfK/PNS Program," KfK Report 3431 B, *Ibid.*

6. P. Hofmann and H. J. Neitzel, "External and Internal Reaction of Zry Tubing with Oxygen and UO_2 and Its Modeling," *5th International Meeting on Thermal Nuclear Reactor Safety, September 9-13, 1984, Karlsruhe, Germany.*

7. W. Dienst, P. Hofmann, D. K. Kerwin-Peck, "Chemical Interactions Between UO_2 and Zry-4 from 1000 to 2000°C," *Nuclear Technology, 65,* 1984, pp. 109-124.

8. P. Hofmann and C. Politis, "The Kinetics of the UO_2-Zry Reactions at High Temperatures," *Journal of Nuclear Materials, 87,* 1979, pp. 375-397.

9. P. Hofmann et al., "Liquid Zry/Liquid UO_2 Interaction Experiments," *The Annual Report of the Nuclear Safety Project (1983)*, KfK Report 3450, 1984, pp. 4200/126-4200/145.

10. P. Nikolopoulos, P. Hofmann, D. K. Kerwin-Peck, "Determination of the Interfacial Energy and Work of Adhesion in the UO_2/Zry-4 Diffusion Couple," *Journal of Nuclear Materials, 124,* 1984, pp. 106-113.

11. S. Hagen et al., "Phenomena and Material Behavior During Meltdown of PWR Fuel Rods," *OECD/NEA Specialists Meeting Behavior of LWR Fuel Elements Under Accident Conditions, Spatind, Norway, 1976.*

12. W. Dienst, P. Hofmann, and P. Kerwin-Peck, "Chemical Interactions Between UO_2 and Zircaloy-4 from 1000 to 2000°C," *Nuclear Technology, 65*, 1984, p. 109.

13. A. Skokan, "High Temperature Phase Relations in the U-Zr-O System," *5th International Meeting on Thermal Nuclear Reactor Safety, September 9-13, 1984, Karlsruhe, Germany.*

14. F. N. Rhines, *Phase Diagrams in Metallurgy*, McGraw-Hill Book Co. Inc., 1956.

15. P. Hofmann, *Reaction-and Melting Behavior of LWR-Core Components UO_2, Zr_2, and Steel During the Meltdown Period*, KfK Report 2220, 1976.

16. Alan D. Knipe, Scott A. Ploger, and Daniel J. Osetek, *PBF Severe Fuel Damage Scoping Test—Test Results Report*, NUREG/CR-4683, EGG-2413, August 1986.

NRC FORM 335
(2-84)
NRCM 1102,
3201, 3202

U.S. NUCLEAR REGULATORY COMMISSION

BIBLIOGRAPHIC DATA SHEET

SEE INSTRUCTIONS ON THE REVERSE

1 REPORT NUMBER (Assigned by TIDC, add Vol. No., if any)
NUREG/CR-5119
EGG-2537

2 TITLE AND SUBTITLE
Metallographic Examination of the Severe Fuel Damage Scoping Test (SFD-ST) Fuel Rod Bundle Cross Sections

3 LEAVE BLANK

4 DATE REPORT COMPLETED

MONTH	YEAR
June	1988

5 AUTHOR(S)
Peter Hofmann

6 DATE REPORT ISSUED

MONTH	YEAR
July	1988

7 PERFORMING ORGANIZATION NAME AND MAILING ADDRESS (Include Zip Code)
EG&G Idaho, Inc.
P.O. Box 1625
Idaho Falls, ID 83415

8 PROJECT/TASK/WORK UNIT NUMBER

9 FIN OR GRANT NUMBER
A6305

10 SPONSORING ORGANIZATION NAME AND MAILING ADDRESS (Include Zip Code)
Division of Reactor Accident Analysis
Office of Nuclear Regulatory Research
U.S. Nuclear Regulatory Commission
Washington, D.C. 20555

11a TYPE OF REPORT
Technical

b PERIOD COVERED (Inclusive dates)

12 SUPPLEMENTARY NOTES

13 ABSTRACT (200 words or less)

A series of severe fuel damage (SFD) tests was performed in the Power Burst Facility (PBF) at the Idaho National Engineering Laboratory (INEL) to obtain data necessary to understand: (a) fission product release, deposition, and transport; (b) hydrogen release; and (c) fuel behavior and coolability during severe fuel damage accidents. This report presents the results from the metallographic posttest examination of the fuel rod bundle cross sections of the first experiment in the SFD series, the Scoping Test (SFD-ST). The metallographic appearance of the zircaloy cladding, solidified melt, UO_2 fuel, Inconel spacer grids, and other instrumentation and structural components is discussed. The observed structures are compared to those documented in well defined, out-of-pile, separate-effects reference experiments. The chemical interactions that take place at high temperatures between the fuel bundle components are described; and estimates of peak test temperatures are made, based only on metallography since scanning electron microscopy results were not available.

14 DOCUMENT ANALYSIS – a KEYWORDS/DESCRIPTORS

severe fuel damage scoping test (SFD-ST)
fuel rod bundle
fuel behavior

b IDENTIFIERS/OPEN-ENDED TERMS

15 AVAILABILITY STATEMENT
Unlimited

16 SECURITY CLASSIFICATION
(This page)
Unclassified
(This report)
Unclassified

17 NUMBER OF PAGES

18 PRICE

*U.S. GOVERNMENT PRINTING OFFICE:1988-202-292:80140

97

UNITED STATES
NUCLEAR REGULATORY COMMISSION
WASHINGTON, D.C. 20555

OFFICIAL BUSINESS
PENALTY FOR PRIVATE USE, $300

SPECIAL FOURTH-CLASS RATE
POSTAGE & FEES PAID
USNRC

PERMIT No. G-67

98